

Structural prediction and materials design

from high throughput to global minima optimization methods



Dissertation

zur Erlangung des akademischen Grades
doctor rerum naturalium (Dr. rer. nat.)

vorgelegt dem Rat der Physikalisch-Astronomischen Fakultät
der Friedrich-Schiller-Universität Jena

von Tiago F.T. Cerqueira, M.Sc.
geboren am 28. Januar 1987 in Amarante

Gutachter:

1. Prof. Dr. Silvana Botti (Friedrich-Schiller Universität Jena)
2. Prof. Dr. Claudia Draxl (Humboldt-Universität zu Berlin)
3. Prof. Dr. Angel Rubio (Max-Planck-Institut für Struktur und Dynamik der Materie)

Tag der Disputation: 26.05.2016

Abstract

In this thesis we use high-throughput techniques and global structure prediction algorithms to predict the crystal structure of different materials under different conditions. We start by investigating the modifications on the structure of carbon nanotubes under hydrostatic pressure. Afterwards, we explore a subset of ternary silicon clathrates searching for new thermodynamically stable phases. Then, we screen the periodic table for new p -type transparent oxides of the form (Cu, Ag, Au, Ni)XO₂ and CuXOS. Finally, we present a new approach for materials design in a pure *ab initio* way.

First, we investigate the radial collapse of CNTs, bundled and individualized in a water environment, using the density functional tight-binding method. For CNTs bundles, we obtain collapse pressures considerably larger than previous estimates based on classical potentials. Furthermore, we show that the effect of chirality on the collapse pressure is small, and that previous reports of large chiral effects are probably due to the use of too small unit cells. For individualized tubes surrounded by water, we observe behaviours that strongly depend on the water filling ratio of the CNT. For empty CNTs, the collapse pressures are higher than for the equivalent calculations of bundles. For filled tubes, low filling ratios destabilize slightly the CNTs, leading to modifications on the CNT cross section at lower pressures than for empty tubes. For higher concentrations of water, we see a consistent increase in the collapse pressure with the increasing filling ratio. Finally, we observe that unusual states of water can be found in the collapsing / collapsed nanotubes. These can range from nanotube-like to 2D sheet-like planes of water, depending on the diameter of the CNT and on the pressure.

In a second step, using *ab initio* high-throughput computational techniques we investigate the stability of ternary clathrate phases based on a Si framework. Our results explain the vast majority of experimental results and predict the existence of a wealth of new thermodynamically stable clathrate phases. Based on this prediction, a new Be-doped clathrate, namely Ba₈Be_{3.7}Si_{42.3}, was successfully synthesized by our co-workers. We note that this clathrate phase would probably be missed experimentally since it can not be expected based on the simple Zintl-Klemm rule.

Using the minima hopping method combined with high-throughput calculations, we also explore the periodic table in search of novel oxide phases. In total, we study 304 different compositions of the form $(\text{Cu}, \text{Ag}, \text{Au}, \text{Ni})\text{XO}_2$ and CuXOS , where X is an element of the periodic table. The choice of this specific set is motivated by the fact that it includes Cu delafossite compounds, which are the best-known *p*-type transparent conductive oxides. Our calculations identify 93 stable compositions, out of which only 41 are already included in materials databases. We then prescreen these new phases for applications as *p*-type transparent conductors by calculating their electronic band gap and hole effective masses, finding a few potentially good candidates.

With the lessons learnt from the previous tasks, we propose a novel approach to design new materials with tailored properties using only the laws of quantum mechanics and the knowledge of the periodic table. This is done by combining state-of-the-art methods of global structure prediction with an evolutionary algorithm that optimizes the chemical composition for the desired property. As a first showcase demonstration of our method, we perform an unbiased search for superhard materials and for transparent conductors. The approach used is extremely successful, with several interesting, unknown materials stemming from the simulations.

Abstrakt

In dieser Arbeit setzen wir Hochdurchsatz-Techniken und globale Strukturvorhersage-Algorithmen ein, um die Kristallstruktur verschiedener Materialien unter verschiedenen Bedingungen vorherzusagen. Wir beginnen mit einer Untersuchung der Struktur-Modifikationen von Kohlenstoff-Nanoröhren (CNT) unter hydrostatischem Druck. Anschließend durchsuchen wir eine Untergruppe der ternären Silizium-Clathrate nach neuen thermodynamisch stabilen Phasen. Danach durchforsten wir das Periodensystem der Elemente nach neuen p -dotierten transparenten Oxiden von der Form $(\text{Cu}, \text{Ag}, \text{Au}, \text{Ni})\text{XO}_2$ und CuXOS . Schlussendlich präsentieren wir einen neuen Ansatz für ein reines *ab initio* Material-Design.

Zunächst untersuchen wir den radialen Kollaps von gebündelten CNT und von einzelnen CNT in einer Wasser-Umgebung mit der Dichte-Funktional-Tight-Binding-Methode. Für gebündelte CNT erhalten wir deutlich höhere Kollaps-Drücke, als frühere Abschätzungen mittels klassischer Potentiale ergeben hatten. Darüberhinaus zeigen wir, dass die Chiralität nur einen geringen Einfluss auf den Kollaps-Druck hat, und dass frühere Berichte über einen starken chiralen Einfluss vermutlich auf die Verwendung zu kleiner Einheitszellen zurückzuführen sind. Im Fall von einzelnen, von Wasser umgebenen Nanoröhren beobachten wir, dass ihr Verhalten stark vom Wasser-Füllungsgrad der CNT abhängt. Bei leeren Nanoröhren ist der Kollaps-Druck höher als in denäquivalenten Rechnungen für Bündel. In dem Fall, dass die Röhren teilweise mit Wasser gefüllt sind, führt ein geringer Füllgrad zu einer leichten Destabilisierung der CNT, was eine Modifikation des Röhren-Querschnitts bereits bei geringeren Drücken als bei leeren Röhren zur Folge hat. Bei höheren Wasserkonzentrationen sehen wir einen konsistenten Anstieg im Kollaps-Druck mit zunehmendem Füllgrad. Schließlich beobachten wir ungewöhnliche Konfigurationen für das Wasser in den kollabierten Röhren. Diese können, abhängig von Röhrendurchmesser und Druck, von nanoröhrenartig bis zu zweidimensionalen planaren Schichten variieren.

In einem zweiten Schritt untersuchen wir mittels Hochdurchsatz-*ab initio*-Rechnungen die Stabilität ternärer Clathrate auf Si-Basis. Unsere Ergebnisse erklären den Großteil der experimentellen Ergebnisse hierzu und sagen eine Fülle von neuen, thermodynamisch stabilen Clathrat-Phasen voraus. Aufgrund unserer Vorhersage wurde von unseren Kollegen mit $\text{Ba}_8\text{Be}_{3.7}\text{Si}_{42.3}$ ein neuer Be-dotierter Clathrat erfolgreich synthetisiert. Wir bemerken, dass

diese Clathrat-Phase experimentell vermutlich übersehen worden wäre, weil sie die einfache Zintl-Klemm-Regel nicht erfüllt und daher eine unerwartete Zusammensetzung darstellt.

Mittels einer Kombination der Minima-Hopping-Methode und Hochdurchsatz-Rechnungen durchkämmen wir außerdem das Periodensystem der Elemente auf der Suche nach neuen Oxid-Phasen. Insgesamt untersuchen wir 304 verschiedene Zusammensetzungen der Form $(\text{Cu}, \text{Ag}, \text{Au}, \text{Ni})\text{XO}_2$ und CuXOS , wobei X ein Element des Periodensystems ist. Die Motivation für die Wahl dieses spezifischen Systems liegt darin, dass es mit den Delafossiten die besten bekannten *p*-dotierten leitfähigen Oxide beinhaltet. Unsere Rechnungen identifizieren 93 stabile Zusammensetzungen, von denen erst 41 bereits in Material-Datenbanken aufgeführt sind. Diese neuen Phasen untersuchen wir im Hinblick auf eine Anwendung als *p*-dotierte transparente Leiter, indem wir ihre elektronischen Bandlücken und effektiven Massen berechnen, und finden einige potenziell gute Kandidaten.

Auf der Grundlage des bis hier Gelernten schlagen wir einen neuen Ansatz vor, um neue Materialien mit maßgeschneiderten Eigenschaften einzig aus den Gesetzen der Quantenmechanik und der Kenntnis des Periodensystems heraus zu entwickeln. Dies erfolgt durch eine Kombination von State-of-the-Art-Methoden der globalen Strukturvorhersage mit einem evolutionären Algorithmus, welcher die chemische Zusammensetzung für die gewünschte Eigenschaft optimiert. Als Vorzeiganwendung unserer Methode betreiben wir eine unvoreingenommene Suche nach superharten Materialien und transparenten Leitern. Der Ansatz ist äußerst erfolgreich, liefert er doch einige interessante, bisher unbekannt Materialien.

Contents

1	Introduction	1
2	Theoretical background	5
2.1	Density Functional Theory	5
2.2	Kohn-Sham Equations	8
2.3	Density Functional Tight-Binding Method	9
2.4	Structural Prediction Algorithms	12
2.4.1	Random Search	13
2.4.2	Simulated Annealing	14
2.4.3	Genetic Algorithms	14
2.4.4	Particle Swarm	14
2.4.5	Minima Hopping Method	15
2.5	Structural Stability	16
3	Radial collapse of Carbon Nanotubes	19
3.1	Carbon nanotubes bundles	21
3.2	Individualized Carbon nanotubes in water	28
3.3	Summary and Conclusions	36
4	Type-I Silicon Clathrates	39
4.1	Details of Calculations	40
4.2	Results and Analysis	45
4.3	Summary and Conclusions	51
5	New <i>p</i>-type transparent conducting oxides by global structure prediction	53
5.1	Details of Calculations	55
5.2	Results and Analysis	59
5.2.1	Delafossites	63
5.2.2	Group IA	66

5.2.3	Group IIA	68
5.2.4	Transition metals	69
5.2.5	Halogens	74
5.2.6	Others	76
5.3	Summary and Conclusions	78
6	Materials Design and Inverse Problem	81
6.1	Details of Calculations	82
6.1.1	Genetic algorithms	83
6.1.2	Ab initio calculations	83
6.1.3	Hardness evaluations	84
6.1.4	Calculation of the gaps and hole effective masses	84
6.2	Results and Analysis	85
6.3	Summary and Conclusions	91
7	Summary and Conclusions	95
	Bibliography	97
	Appendix A Bader charges, oxidation states, and coordination numbers (Chapter 5)	113

Chapter 1

Introduction

For centuries, materials' discovery was only possible by experimental synthesis. Most of this knowledge concerning the crystal structure of (inorganic) materials is nowadays gathered in generally available databases. The most used of these, the Inorganic Crystal Structure Database (ICSD) [1] contains around 170,000 entries. This number can be compared, e.g., to the number of chemical substances in the CAS registry (more than 103 million), to the number of macromolecules in the RCSB Protein Data Bank [2] (more than 100,000), or even the number of crystals (organic and inorganic) in the Crystallography Open Database [3] (around 300,000).

However, these 170,000 entries in the ICSD include duplicated structures, insufficiently characterized phases (e.g., missing the positions of H atoms), and several alloys. If we restrict ourselves to well-defined crystal structures we find around 50,000 entries. It is this amount of 50,000 entries that has been studied theoretically, in a systematic manner, over the last few years using high throughput techniques. The results of these large-scale studies can be found in excellent publicly available databases, such as the Materials Project [4], the Open Quantum Materials Database [5], or the Ab-initio Electronic Structure Library AFLOWLIB [6].

But let us go a step back and, and look at the 50,000 materials we know nowadays. The first question that comes to our mind is if this set is representative of the number of (thermodynamically stable) materials that we can create in a lab. The answer to this question is probably no. It is true that elementary substances and binary compounds are relatively well studied, but present knowledge of ternary and multinary materials is likely less complete. Of course, a systematic experimental endeavor of synthesis and characterization of all possible phases is extremely expensive and time-consuming. It is for this task that numerical simulations appear as the most cost-effective way to explore the gigantic search space of compositions at our disposal. One way to do this is by using these databases as the

starting point for sophisticated machine learning techniques that try to design new materials with tailored properties. These techniques have been touted as the most cost effective path to the discovery of new materials in a diverse range of applications, such as Li batteries [7, 8], thermoelectricity [9–11], or photovoltaics [12–15].

An alternative approach to computational materials discovery that does not rely on databases is crystal structural prediction (CSP). This is a relatively new field, that gained some momentum by the beginning of the 21th century. However, we still had to wait another 10 years before seeing any large scale application. There are several reasons why CSP remained, in practice, unaccessible for so long. First of all, CSP is one of the computationally more demanding problems in materials science. Secondly, universal access to high performance computing (HPC) infrastructures is also recent. To give an example, the first European HPC initiative (HPCEUR) only appeared in 2004. Third, accurate *ab initio* methods that allow for proper simulations of (sizeable) quantum systems were also under development. Finally, and perhaps due to the previous points, efficient algorithms for CSP were also only developed around this time. Nevertheless, most of these limitations are by now overcome, and a new era of computationally-guided materials discovery has already begun.

The main goal of this thesis is to extend the knowledge of new materials using state-of-the-art *ab initio* structural predictions methods. There is a huge demand for new, revolutionary materials. These are expected to leverage ground breaking developments in critical technological areas like thermoelectricity, high temperature superconductors, batteries, solar cells, transparent electronics, *etc.* In some of these fields the solutions that exist are simply not good enough for large scale applications, while in others, cheaper and more sustainable alternatives are desired. To this end, besides using already well established technics, we will also need develop novel approaches to tackle some limitations of the standard methods. Two key ingredients are needed: first, we need a crystal structure prediction algorithm, that allows us to explore efficiently the potential energy surface. To this end we chose the minima hopping method (MHM) [16, 17]. Second, we need a method able to calculate accurately energies, forces and stresses. Here, the obvious choice is density functional theory [18, 19]. This choice is well motivated by the fact that density functional theory is by now the only theory that is able to provide a convenient accuracy for a relatively moderate computational effort. This thesis is organized as follows:

Chapter 2 is an introduction to the theoretical framework. I will start by an brief introduction to Density Functional Theory (DFT), followed by an overview of the Density Functional Tight-Binding method (DFTB). Finally, we discuss structural prediction methods, including the important topic of structural stability.

Chapter 3 is about the radial collapse of carbon nanotubes (CNT). This work was done in collaboration with the experimental group of Prof. A. San-Miguel in Lyon. I will present results for quasi-static DFTB calculations of bundled, and individualized CNTs in water, using the DFTB method, as these systems are too large for systematic DFT calculations. In this case, we are not interested in finding the lowest energy structure, but rather we want to follow the evolution of the CNT structures with pressure.

In Chapter 4 I deal with the subject of type-I Silicon Clathrates. Si clathrates are widely studied compounds that gained a renewed attention in the recent years as they have been investigated for thermoelectric applications. Their band gap can be easily tuned by doping the framework structure and the center of the cages. At the same time, the unit cell complexity and the host-guest interaction lead to a very low lattice thermal conductivity. Due the large number of combinations of doping elements, a variety of different clathrate phases has been synthesized. However, we think that many more are still due to be discovered. Therefore, we used computational high-throughput techniques in order to search for potentially new thermodynamic stable clathrate phases. Here, we are only interested in compounds with the type-I clathrate structure (space group 223), hence no global structure prediction is needed.

In Chapter 5 we use *ab initio* global structural prediction combined with high-throughput calculations to explore the periodic table in search of novel oxide phases. The goal is to find unknown compounds within the stoichiometries $(\text{Cu,Ag,Au,Ni})\text{XO}_2$ and CuXOS where X is an element of the periodic table. The choice of this specific set is motivated by the fact that it includes Cu delafossite compounds, which are the best known *p*-type transparent conductive oxides, critical for potential applications in transparent electronics.

Chapter 6 present our work done on materials design, i.e., the so-called *inverse problem*: given a certain desired property (or properties), discover (design) the material that possesses this property under a given set of constrains. We propose a novel approach to design new materials with tailored properties using only the laws of quantum mechanics and the knowledge of periodic table. This is done by combining an evolutionary algorithm that optimizes the chemical composition for the desired property, and the minima hopping method that searches for the ground state structure of each chemical composition. On top of this, we developed software to automatize most of the workflow, which turns these complex calculations feasible.

Finally, in Chapter 7 we present a summary and relevant conclusions of this thesis.

With the exception of Chapter 4, most of the results presented in this thesis have been published in Refs [20–22]

Chapter 2

Theoretical background

Kohn-Sham Density Functional Theory (DFT) is by now the default choice for condensed matter *ab initio* simulations. Backed by the exponential growth of the computational power, we are no longer limited to simple systems like small molecules or periodic systems with a few atoms per unit-cell. In fact, calculations with several thousands of atoms have already been possible for some time, being the known record at the moment over 2 million atoms [23].

Long gone are the days where a computer simulation would serve merely as a complement for an experiment. We live in the era where *ab initio* calculations are accurate enough not only to reproduce experimental data, but also to estimate properties of materials inaccessible experimentally. More recently, even the prediction of new materials has become possible, allowing the exploration of a large variety of systems in a fast and relatively inexpensive way.

In this chapter, I introduce the framework used throughout this thesis. DFT is one of the key ingredients, therefore I start with a brief introduction to this theory. In the following, I give a description of the density functional tight-binding method, an approximation to DFT that allows the study of large systems, too large for systematic studies with *ab initio* methods. Then, a description of the several algorithms which make structural prediction possible. Finally, a discussion on structural stability.

2.1 Density Functional Theory

Let us consider a system of N non-relativistic electrons described by the time-independent Schrödinger equation, in the Born-Oppenheimer approximation [24], written as

$$\hat{H}\Psi(\mathbf{x}_1, \mathbf{x}_2, \dots, \mathbf{x}_N) = E\Psi(\mathbf{x}_1, \mathbf{x}_2, \dots, \mathbf{x}_N), \quad (2.1)$$

where \mathbf{x}_i comprehends the spatial and spin coordinates of electron i (\mathbf{r}_i, σ_i). The hamiltonian operator can be written as,

$$\hat{H} = \hat{T} + \hat{V}_{\text{ext}} + \hat{V}_{\text{ee}}, \quad (2.2)$$

where the kinetic energy, the external potential, and the electron-electron repulsion operators are respectively:

$$\hat{T} = -\sum_{i=1}^N \frac{1}{2} \nabla_i^2, \quad \hat{V}_{\text{ext}} = \sum_{i=1}^N v_{\text{ext}}(\mathbf{r}_i), \quad \text{and} \quad \hat{V}_{\text{ee}} = \sum_{i<j}^N \frac{1}{r_{ij}}, \quad (2.3)$$

with

$$v_{\text{ext}}(\mathbf{r}_i) = -\sum_I \frac{Z_I}{r_{iI}} \quad \text{and} \quad r_{ij} = |\mathbf{r}_i - \mathbf{r}_j|. \quad (2.4)$$

Here, capital indices stand for the nuclear coordinates and Z_I is the atomic number of the nuclei I . Hartree atomic units are used throughout. To obtain the total energy of the system we have also to add the nuclei-nuclei repulsive energy contribution,

$$V_{\text{nn}} = \sum_{I<J} \frac{Z_I Z_J}{r_{IJ}}. \quad (2.5)$$

In principle, by solving equation (2.1), we can calculate all the physical quantities we want. However, there are several reasons why this is simply not possible. In the first place, Ψ is a function of $3N$ variables. Just storing the wave-function in memory is an impossible task, even for small atomic systems. Secondly, due to the last term of (2.2), we can not solve the equation independently for each of the N particles.

In DFT we replace as the basic physical quantity the complicated multi-dimensional wave-function Ψ by a much simpler quantity - the electronic density of the system $n(\mathbf{r})$, which is a function of just 3 variables. The first step was done in 1927 by Llewellyn Thomas [25] and Enrico Fermi [26] which, independently, idealized a model where the full many-body Schrödinger equation was replaced by one equation depending only on the electronic density of the system. This approach was later developed by Hohenberg and Kohn in 1964 [27], who paved the mathematical ground for density function theory with two fundamental theorems. Considering a N -electron system with a non-degenerate ground-state ruled by the Hamiltonian (2.2), the first theorem states that the external potential $v_{\text{ext}}(\mathbf{r})$ is determined, within an additive constant, by the electronic ground state density $n_0(\mathbf{r})$ of the system. That is, there is a one-to-one correspondence between the electronic density of the system and the

external potential. Besides that, they proved that any observable of the system can be written as a unique functional of the density,

$$\langle \Psi | \hat{O} | \Psi \rangle = O[n]. \quad (2.6)$$

For instance, we can write the total energy of the system under an external potential v_{ext} as a functional of the density:

$$\begin{aligned} E_{v_{\text{ext}}}[n] &= \langle \Psi | \hat{T} + \hat{V}_{\text{ext}} + \hat{V}_{\text{ee}} | \Psi \rangle + E_{\text{nn}} \\ &= F_{\text{HK}}[n] + \int d\mathbf{r} n(\mathbf{r}) v_{\text{ext}}(\mathbf{r}) + E_{\text{nn}}, \end{aligned} \quad (2.7)$$

where

$$F_{\text{HK}}[n] = T[n] + V_{\text{ee}}[n] \quad (2.8)$$

is an universal functional, independent of the external potential, that is the same for any N -electron system. The second theorem states that, for a non-negative trial density, \tilde{n} , and $\int \tilde{n} d\mathbf{r} = N$:

$$E_0 \leq E_{v_{\text{ext}}}[\tilde{n}]. \quad (2.9)$$

The exact ground-state density is then the one that minimizes the energy functional (2.7)

$$E_0 = \min_{\{n\}} E_{v_{\text{ext}}}[n]. \quad (2.10)$$

which can also be written as

$$\frac{\delta}{\delta n(\mathbf{r})} \left[E_{v_{\text{ext}}}[n] - \mu \int n(\mathbf{r}) d\mathbf{r} \right] = \frac{\delta F_{\text{HK}}[n]}{\delta n(\mathbf{r})} + v_{\text{ext}}(\mathbf{r}) - \mu = 0, \quad (2.11)$$

where μ is a Lagrange multiplier that ensures the normalization of the density to the total number of electrons. So, solving Eq. (2.11) would give us the exact ground-state of any electronic system. However, the explicit form of F_{HK} is unknown.

2.2 Kohn-Sham Equations

Let us consider a non-interacting system of electrons ($\hat{V}_{ee} = 0$ in equation (2.2)). In this case, the many-body ground-state wave-function can be written as a Slater determinant of single particle wavefunctions ψ_i ,

$$\Psi_s(\mathbf{x}_1, \mathbf{x}_2, \dots, \mathbf{x}_N) = \frac{1}{\sqrt{N!}} \begin{vmatrix} \psi_1(\mathbf{r}_1) & \psi_2(\mathbf{r}_1) & \cdots & \psi_N(\mathbf{r}_1) \\ \psi_1(\mathbf{r}_2) & \psi_2(\mathbf{r}_2) & \cdots & \psi_N(\mathbf{r}_2) \\ \vdots & \vdots & \ddots & \vdots \\ \psi_1(\mathbf{r}_N) & \psi_2(\mathbf{r}_N) & \cdots & \psi_N(\mathbf{r}_N) \end{vmatrix}, \quad (2.12)$$

satisfying:

$$\left[-\frac{1}{2}\nabla^2 + v_s(\mathbf{r}) \right] \psi_i(\mathbf{r}) = \varepsilon_i \psi_i(\mathbf{r}). \quad (2.13)$$

Here, v_s is a fictitious external potential. The ground-state density is obtained from the N lowest occupied orbitals,

$$n(\mathbf{r}) = \sum_{i=1}^N |\psi_i(\mathbf{r})|^2. \quad (2.14)$$

The variational principle for this non-interacting system yields:

$$\frac{\delta}{\delta n(\mathbf{r})} \left[E_s[n] - \mu_s \int n(\mathbf{r}) d\mathbf{r} \right] = \frac{\delta T_s[n]}{\delta n(\mathbf{r})} + v_s(\mathbf{r}) - \mu_s = 0. \quad (2.15)$$

This is formally equivalent to equation (2.13). Now, let us consider again the interacting system. We can rewrite the functional (2.8) as

$$F_{\text{HK}}[n] = T_s[n] + E_{\text{H}}[n] + E_{\text{xc}}[n], \quad (2.16)$$

where $E_{\text{H}}[n]$ is the classic Coulomb energy, also known as the Hartree energy

$$E_{\text{H}}[n] = \frac{1}{2} \int d\mathbf{r} \int d\mathbf{r}' \frac{n(\mathbf{r})n(\mathbf{r}')}{|\mathbf{r} - \mathbf{r}'|}, \quad (2.17)$$

and the non-classical part, the exchange and correlation energy

$$E_{\text{xc}}[n] = T[n] + V_{ee}[n] - T_s[n] - E_{\text{H}}[n]. \quad (2.18)$$

With these modifications the Euler equation (2.11) reads:

$$\frac{\delta T_s[n]}{\delta n(\mathbf{r})} + v_{\text{ext}}(\mathbf{r}) + \frac{1}{2} \int d\mathbf{r}' \frac{n(\mathbf{r}')}{|\mathbf{r} - \mathbf{r}'|} + \frac{\delta E_{\text{xc}}[n]}{\delta n(\mathbf{r})} - \mu = 0. \quad (2.19)$$

Finally, we can rewrite this Euler equation as:

$$\frac{\delta T_s[n]}{\delta n(\mathbf{r})} + v_{\text{KS}}[n](\mathbf{r}) - \mu = 0, \quad (2.20)$$

where

$$v_{\text{KS}}[n](\mathbf{r}) = v_{\text{ext}}(\mathbf{r}) + v_{\text{H}}[n](\mathbf{r}) + v_{\text{xc}}[n](\mathbf{r}), \quad (2.21)$$

with

$$v_{\text{H}}[n](\mathbf{r}) = \frac{1}{2} \int d\mathbf{r}' \frac{n(\mathbf{r}')}{|\mathbf{r} - \mathbf{r}'|} \quad \text{and} \quad v_{\text{xc}}[n](\mathbf{r}) = \frac{\delta E_{\text{xc}}[n]}{\delta n(\mathbf{r})}. \quad (2.22)$$

If we now compare equation (2.20) with (2.15), we see that the two are identical and therefore, solving (2.20) has to be the same as solving the single-particle Schrödinger equation:

$$\left[-\frac{1}{2} \nabla^2 + v_{\text{KS}}[n](\mathbf{r}) \right] \psi_i(\mathbf{r}) = \epsilon_i \psi_i(\mathbf{r}), \quad (2.23)$$

where the ground-state density is given by:

$$n(\mathbf{r}) = \sum_{i=1}^N |\psi_i(\mathbf{r})|^2. \quad (2.24)$$

Equations (2.20) and (2.23) are known as the Kohn-Sham equations [28]. They allow us to treat a system of interacting electrons using a non-interacting one, that yields the same ground-state density. This would be *exact* if we knew the exact form of E_{xc} , but we do not. Nevertheless, the major part of the electron-electron interaction (the Hartree energy) is treated exactly and so does the non-interacting kinetic energy. The remaining exchange and correlation energy is by far the one that has the smallest contribution to the total energy. It is however, the main responsible for the binding energy of matter, being a good approximation to this term the key to obtain accurate results.

2.3 Density Functional Tight-Binding Method

DFT is certainly the best compromise between accuracy and speed for most of the systems studied in the field of condensed matter. However, when systems at study are too large for

extensive *ab initio* calculations other approaches are required. Force field methods allow for simulations with millions of atoms with limited computer resources. These methods are usually parametric models fitted to experimental data: for a given system and a given model, some parameters are fitted to reproduce experimental data (geometries, energies, *etc*). These can be very precise for systems close to the ones they were fitted to, but they are not always *transferable* to other problems. For instance, a model parameterized to graphite will in principle work well for other systems with sp^2 hybridized carbon, but it will fail for diamond-like systems where carbon adopts a sp^3 hybridization. Somehow in between force fields and *ab initio* we have *semi-empirical* methods. These are derived from *ab initio*, where the traditionally heavy computational terms are simplified and approximated. To compensate for the lost physics, parameters are then fitted to experimental data. Therefore, although they are not as accurate as *ab initio*, they are a few orders of magnitude faster, while transferable to a larger range of systems than force field methods.

Density functional tight binding [29, 30], unlike other *semi-empirical* methods, is fitted to DFT calculations. The energy functional is derived directly from the expectation value of the Kohn-Sham hamiltonian (Eq. (2.23)):

$$E = \sum_i^N \langle \psi_i | -\frac{\nabla^2}{2} + v_{\text{ext}}(\mathbf{r}) + v_{\text{H}}[n](\mathbf{r}) + v_{\text{xc}}[n](\mathbf{r}) | \psi_i \rangle + V_{\text{nn}}, \quad (2.25)$$

where V_{nn} is the energy due to the ions. The first step is to approximate the charge density $n(\mathbf{r})$ as a sum of a reference charge $n_0(\mathbf{r})$ plus a small charge fluctuation $\delta n(\mathbf{r})$. With this substitution, and expanding E around n_0 to second order fluctuation δn (with $n(\mathbf{r}) \rightarrow n$ and $\int d\mathbf{r} \rightarrow \int$):

$$\begin{aligned} E = & \sum_i^N \langle \psi_i | -\frac{\nabla^2}{2} + v_{\text{ext}}(\mathbf{r}) + \frac{1}{2} \int' \frac{n'_0}{|\mathbf{r}-\mathbf{r}'|} + v_{\text{xc}}[n_0] | \psi_i \rangle \\ & - \frac{1}{2} \int \int' \frac{n'_0 n_0}{|\mathbf{r}-\mathbf{r}'|} + E_{\text{xc}}[n_0] - \int v_{\text{xc}}[n_0] n_0 + V_{\text{nn}} \\ & + \frac{1}{2} \int \int' \left(\frac{1}{|\mathbf{r}-\mathbf{r}'|} + \left. \frac{\delta^2 E_{\text{xc}}}{\delta n \delta n'} \right|_{n_0} \right) \delta n \delta n' . \end{aligned} \quad (2.26)$$

The first line of Eq. (2.26) is known as the band-structure energy, E_{BS} . It is usually written in a compact form as

$$E_{\text{BS}} = \sum_i^N \langle \psi_i | \hat{H}_0 | \psi_i \rangle . \quad (2.27)$$

The second line is called the repulsive term, E_{rep} , mainly due to V_{nn} , even if it also contains exchange and correlation contributions. In fact, this term works like the E_{xc} (Eq. (2.18)) in plain DFT – all the complicated physics are put here and approximated. In DFTB this term is written as a sum over atom pairs, IJ , where each one is a simple repulsive function depending only on the atomic species and interatomic distance,

$$E_{\text{rep}} = \sum_{I < J} V_{\text{rep}}^{IJ}(\mathbf{R}_{IJ}) . \quad (2.28)$$

These repulsive functions have to be fitted to reference DFT calculations and constitute the major difficulty for good DFTB parameterizations.

Finally, the last term in Eq. (2.26) contains Coulomb and exchange-correlation interactions due to charge fluctuations. It is commonly referenced as E_{coul} . When performing non self consistent-charge calculations (nonSCC) [31], charge fluctuations are ignored and E_{coul} is simply disregarded. However, for most hetero-nuclear systems this term has to be included. In order to include this effects without a significant computational burden, charge fluctuations δn are decomposed in a sum over normalized atomic contributions δn_I [32]:

$$\delta n = \sum_I \Delta q_I \delta n_I , \quad (2.29)$$

with

$$\Delta q_I \approx \int_{V_I} \delta n . \quad (2.30)$$

The charge fluctuation term is then simply written as:

$$E_{\text{coul}} = \frac{1}{2} \sum_{IJ} \gamma_{IJ}(R_{IJ}) \Delta q_I \Delta q_J , \quad (2.31)$$

where γ_{IJ} is a term that depends only on the distance R_{IJ} and on the Hubbard parameters U_I and U_J , in a way that reproduces the original behavior of the Coulomb and exchange-correlation interactions when $I = J$ and $I \neq J$.

Now, following the traditional tight-binding approach, the single-particle wave-functions ψ_i , are expanded using a minimal local basis (one radial function for each angular momentum state):

$$\psi_i(\mathbf{r}) = \sum_{\mu} c_{\mu}^i \phi_{\mu}(\mathbf{r}) . \quad (2.32)$$

Applying Eq. (2.32) to Eq. (2.26) and applying all the previous approximations, we end up with the final DFTB energy expression:

$$E = \sum_i \sum_{\mu\nu} c_\mu^{i*} c_\nu^i H_{\mu\nu}^0 + \frac{1}{2} \sum_{IJ} \gamma_{IJ}(R_{IJ}) \Delta q_I \Delta q_J + \sum_{I < J} V_{\text{rep}}^{IJ}(\mathbf{R}_{IJ}). \quad (2.33)$$

Using now the variational principle, we obtain the general eigenvalue problem:

$$\sum_{\mu}^M c_{\mu}^i (H_{\mu\nu} - \varepsilon^i S_{\mu\nu}) = 0, \quad \forall \nu, i \quad (2.34)$$

with

$$\begin{aligned} H_{\mu\nu} &= H_{\mu\nu}^0 + \frac{1}{2} S_{\mu\nu} \sum_K (\gamma_{K\mu} + \gamma_{K\nu}) \Delta q_K, \\ &= H_{\mu\nu}^0 + H_{\mu\nu}^1, \quad S_{\mu\nu} = \langle \phi_{\mu} | \phi_{\nu} \rangle, \quad \forall \mu \in I, \nu \in J. \end{aligned} \quad (2.35)$$

Matrix elements of $H_{\mu\nu}^0$ and $S_{\mu\nu}$ are not calculated at runtime. Rather, they are previously calculated and tabulated for efficiency. Localized atomic orbitals ϕ_i are obtained from DFT calculations of free atoms. In order to simulate confined orbitals as one has on multi-atomic systems, an extra confinement term is added to the traditional Kohn-Sham potential. Having ϕ_i , the matrix elements $H_{\mu\nu}^0$ and $S_{\mu\nu}$ are calculated and stored, for fixed values of \mathbf{R}_{IJ} and for each pair of orbitals. These matrix elements, the Hubbard parameters and $V_{\text{rep}}^{IJ}(\mathbf{R}_{IJ})$ are the parameters actually used in a DFTB calculation.

In a non-SCC calculation, the solution of Eq. (2.34) is obtained immediately. On the other hand, in SCC calculations Eq. (2.34) has to be solved self-consistently, akin to the Kohn-Sham equations. For a starting guess set of Δq_i , we calculate $H_{\mu\nu}^1$ and solve Eq. (2.34) to obtain the expansion coefficients c_{ν}^i . With these coefficients, updated Δq_i are obtained and used again to calculate $H_{\mu\nu}^1$. This process is repeated until the new and previous Δq_i are the same within some tolerance value.

2.4 Structural Prediction Algorithms

Crystal structure prediction is one of the hardest problems in materials science. This is in part due to the fact that the number of local minima of the potential energy surface (PES) increases exponential with the number of atoms in the system. Another problem is that there is no quantity that can unequivocally tell if one has arrived to the global minimum. Local optimizers are only capable of optimizing a structure to the closest local minimum. Therefore, either one knows approximately the ground state structure of a compound, and in

this case a local optimizer will do the job, or one needs an algorithm that allows to search the whole PES. The first case suggests a strategy used in materials science as a valuable method for materials discovery. Following the principle that Nature often chooses similar answers to similar problems, if one knows the crystal structure characteristic of a family of compounds (delafossites, perovskites, clathrates, Heuslers, *etc*), one can find a different compound by replacing one atom with a different one. In this case, a local optimization is enough to relax the new structure that hopefully, will also be the ground state structure for the new compound. Higher success rates can be achieved by using sophisticated machine learning algorithms, which can help to choose the most likely substitutions. This approach is currently widely used with very good results, and applications to several areas have already been published [7, 33–35]. However, as it relies heavily on experimental data, it will fail to find compounds that are very different from what is already known.

Structural prediction algorithms are then designed to explore large regions of the PES, aiming to find its global minimum. Several methods to tackle this problem were proposed with demonstrated success [36–38]. Incidentally, these methods also allow the discovery of low energy metastable structures, not always accessible experimentally in normal conditions, at no extra cost. In the next paragraphs an overview of the most used methods is given, with special a emphasis on our method of choice: the minima hopping method (MHM). All these methods are fairly general and can be used with several *ab initio* / semi-empirical codes, as long as they can provide energies, forces and stresses. In our case, all the MHM runs in this thesis used energies and forces calculated using DFT as implemented in the code VASP [39, 40].

2.4.1 Random Search

Random search is perhaps the simplest of all the methods for structure prediction. It tries to find the global minimum by spawning several random structures across the PES (solid circles in Fig. 2.1a), which are then (locally) optimised (empty circles). By repeating this several times one expects to eventually find the global minimum - each colored circle represents a different candidate structure. Several constrains (space group, cell volume, distance between different atoms, etc) are applied to limit the otherwise too large search space and speed up the process. Available experimental data can also help biasing the initial structures for the problem at hand.

2.4.2 Simulated Annealing

Simulated annealing [41] can be seen as the computer realization of metallurgy. Here, metals are melt at high temperatures and subsequently cooled in a controlled way. In simulated annealing, the energy of a candidate structure is evaluated at a certain (high) temperature. Afterwards, atomic positions and cell vectors are perturbed using molecular dynamics or Monte-Carlo and the energy of this new structure is calculated. This new structure is then accepted or rejected based on the Metropolis criterion. This process is repeated while the simulation temperature is gradually decreased. Initial structures have a higher probability of being accepted since the temperature is high, which leads to disordered (amorphous) structures. As the temperature decreases, lower energy structures will have higher accepting rates. When the temperature reaches 0 K, only lower energy structures are accepted.

2.4.3 Genetic Algorithms

Genetic algorithms [42] inherited their name from genetics, due to their principle of “*survival of the fittest*”, which makes them similar to the Darwinian evolution.

For a given stoichiometry, several different candidates are created (population) – filled green and red circles in Fig. 2.1b. These initial structures can either be random structures or educated guesses for this particular problem. After a local optimization (empty circles), the target property (or properties) is calculated – the thermodynamic stability in most cases. The best candidates are chosen, and a new set of structures (generation) is created containing part of these candidates, and new structures obtained from crossover operations between the best candidates (blue circle). There are also other possible operations like mutations, where an atom is replaced by another one, or permutations, where two atoms of the crystal are permuted. These operations are also applied to the cell vectors to create new cell parameters that are not copies of the ones of the parents, but instead a mixture of both. Genetic algorithms are perhaps, the most widely used algorithms nowadays for crystal structure prediction.

2.4.4 Particle Swarm

Particle swarm optimization [43] is inspired by the swarm behavior found in Nature (insects and birds for instance). The main idea is to have several walkers exploring different points of the PES at the same time, as one has in a parallel random search algorithm. In this case, however, each walker shares its position in the PES with the others and they move across the PES as a group. At each instant, the position of each walker, $x_i(t')$, depends on its previous position, $x_i(t)$, and its velocity, $v_i(t')$, as $x_i(t') = x_i(t) + v_i(t')$. Its velocity depends not only

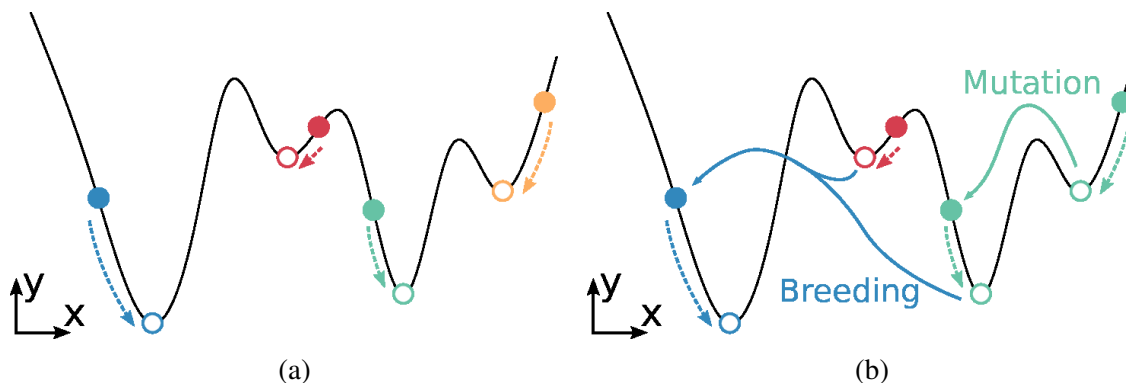


Figure 2.1 Hypothetical PES and schematic algorithm for (a) random search and (b) genetic algorithm. The x axis represents some internal degree of freedom, while y is the energy for a given configuration.

on its previous velocity, $v_i(t)$, but also on the history of all the walkers, namely the position of the best known minimum, $g_{best}(t)$, and its optimized position, $p_{best}(t)$, as

$$v_i(t') = \omega v_i(t) + c_{i_1} r_{i_1} (p_{best}(t) - x_i(t)) + c_{i_2} r_{i_2} (g_{best}(t) - x_i(t)). \quad (2.36)$$

Here, ω is an inertia weight, r_{i_1}, r_{i_2} are random numbers and c_{i_1}, c_{i_2} control how much each walker trusts its position compared to the best known minimum. An hypothetical path for a single walker can be seen in Fig. 2.2a (green circles).

2.4.5 Minima Hopping Method

The Minima Hopping Method, developed by S. Gödecke and M. Amsler [16, 17], is a structural prediction algorithm that tries to find the global minimum of a PES by jumping between local minima using short molecular dynamics (MD) runs (solid arrows in Fig. 2.2b), followed by local geometry optimizations at each minima (dashed arrows). An energy based acceptance criteria assures that each new minimum has a 50% chance of being accepted (δE in the figure). This means that every time a new minimum is found, the acceptance criterion is adjusted to guarantee that, on average, only half of the local minima are accepted. In order to avoid revisiting already explored minima, the temperature of the MD runs is adjusted dynamically during the search. This is done to allow escaping local minima surrounded by high energy barriers. A *softening* process is used to accelerate the minimization problem as it is expected that (on average) crossing low energy barriers will lead to lower energy minima [44]. Hence, the MD velocities should be aligned along directions of low curvatures

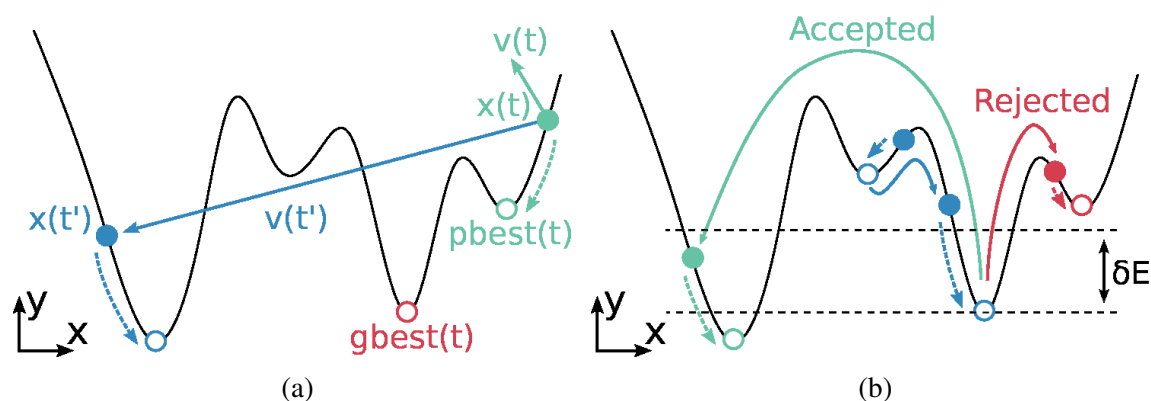


Figure 2.2 Hypothetical PES and schematic algorithm for (a) particle swarm optimization and (b) minima hopping. The x axis represents some internal degree of freedom, while y is the energy for a given configuration.

– soft modes. In practice, as a perfect alignment would eliminate the random character of the escape step, these directions are chosen only to avoid hard mode directions.

This method is able to optimize both cell vectors and atomic positions, being the only constraints the stoichiometry and the number of unit cells. In our runs, we start always from a random structure, assuring only that the minimum distance between atoms is at least equal to the sum of their covalent radii.

The minima hopping method has been used for structural prediction in a wide range of materials [45–48], including the dependence on pressure [49] and the exploration of binary phase diagram [50–52] with remarkable results.

2.5 Structural Stability

Now that we have described how to get an optimised (new) structure of a given composition, we ask ourselves how we know if this is the ground-state structure, and more importantly, how we know if this structure is accessible experimentally. Even for small systems there are a lot of possible combinations of arrangements of atoms / crystal structures, most of them not favorable thermodynamically. Also, independently of the algorithm used, there is no guarantee that the lowest energy found is the ground-state. In fact, it can happen that the true ground state is not accessible (too large unit cells, temperature, pressure, *etc*). The question is then how to estimate the thermodynamic stability of a compound.

Let us consider a system at zero pressure and zero temperature. The relevant thermodynamic quantity in this case is simply the total energy E . The simplest way one can think of to estimate the stability is to compare the energy of the compound with the energy of its individ-

ual constituents. For instance, we consider a binary compound A_nB_m with energy E . A_nB_m is thermodynamically stable if $E - (nE_A + mE_B) < 0$. This quantity is known as the formation energy. However, this only tells us that A_nB_m is stabler than the sum of its constituents. We are not considering the case were another compound, for example A_nB_n , could be even more stable. Therefore, when calculating the thermodynamic stability of a structure we should compare its energy with all the possible decomposition channels. This leads to the concept of convex hull of stability. We define the convex hull of thermodynamic stability as the hypersurface in composition space that passes by all materials that are thermodynamically stable. Unstable materials will be above the hull, and the distance will be a measure of the energy released by decomposing into the stable phases. In this context, a compound is thermodynamically stable if its distance to the convex hull is zero. Therefore, one needs to search for the experimentally and theoretical known decomposition channels, calculate them using e.g. DFT, and compare them with our new candidate structure. Fortunately, nowadays there are several public available databases of DFT calculations where one can extract easily this information [4–6], provided they were obtained in the same simulation conditions (same code, pseudo-potentials, number of k-points, cut off energy, etc).

Another important aspect to take in account is the dynamic stability. Local optimizations result in stationary points on the PES – i.e. the first derivatives of the energy are close to zero. However, this does not assure that we are in a minimum. For that, we need to calculate second derivatives of the energy, which are related to phonon frequencies. Imaginary phonon frequencies are then signs of dynamic instability. That said, a thermodynamically stable structure ($E_{hull} = 0$) can still be dynamically unstable, meaning that we did not find its ground state.

Chapter 3

Radial collapse of Carbon Nanotubes

Since the outstanding paper by Iijima in 1991 [53] carbon nanotubes remain an intense field of research. Their unique electronic and mechanical properties make them ideal candidates for novel electronics and new superhard materials. Despite their very high resilience and Young modules, it was observed that nanotubes can undergo ovalization and collapse, sometimes even at atmospheric pressure [54, 55]. The impact of these geometrical changes on the electronic properties is still subject to debate [56–58]. Moreover, the collapse process itself is still not completely understood, as only indirect observation is reported. It is expected that the radial collapse pressure of a carbon nanotube is mainly determined by its diameter [59–64], but other factors, like the nanotube chirality, the presence of defects, the choice of the pressure transmitting medium [65] (PTM), and the nanotube filling (e.g. argon [65], water [66], fullerenes [67, 68] or other nanotubes [68, 69]) are also known to be relevant [70, 71].

Experimentally, Raman spectroscopy is the main technique used to study the collapse of nanotubes. However there is not yet a clear consensus on the best spectroscopic signature of the collapse. Several footprints have been proposed: (i) the disappearance of the radial breathing mode signal, which has been used in literature either to identify the polygonization [72] or the ovalization [73] of the cross-section, or directly the tube collapse [74] ; (ii) the change of slope [73, 75, 76], the presence of a plateau [74], or even the change of sign [67] of the curve representing the dependence of the G-band frequency with respect to pressure. However, the use of the progressive attenuation of the Raman modes intensity was questioned, due to the resonant character of the Raman signal [77], and the modifications of the resonance conditions induced by pressure [78, 79]. Many factors, in fact, contribute to make experimental results difficult to interpret: the inhomogeneity of the geometrical characteristics of the tubes in the samples, impurities and defects resulting from the growth processes, or the use of different pressure transmitting media [65, 80–82], which could

eventually become solid before the observation of the collapse or even penetrate the tubes if these are open [65]. In fact, for tubes of similar diameters, the experimental values of the collapse pressure of single-wall bundles can differ of more than one order of magnitude. These values have been shown to be extremely sensitive to the nature of the pressure transmitting media [67]. Other experimental methods have been used to observe the pressure induced modification of the cross-section, such as neutron diffraction [83] (indicating a progressive polygonization), X-ray diffraction [84] (with no indication of collapse transitions up to 10 GPa in arc-discharge carbon nanotubes) or optical spectroscopy [85].

There are many theoretical papers dealing with the collapse of carbon nanotubes [59, 63, 64, 70, 71, 86–95]. Unfortunately, theoretical works using different methods and setups are known to give dissimilar and sometimes even contradictory results. In particular, calculations performed with classical potentials usually yield collapse pressures around 50% smaller than the ones obtained with *ab initio* methods [63]. However, even when calculations are performed with comparable approaches, the output values of the collapse pressure are very scattered and difficult to reconcile. The reasons are easy to understand if we consider that calculations are usually performed using either classical potentials or density-functional theory. While the latter is certainly the most precise method, density-functional simulations are numerically very heavy for these systems, and therefore calculations are usually performed for very small unit cells containing only one (zigzag or armchair) nanotube. Classical potentials are certainly numerically much more efficient, and allow for simulations of unit-cells containing several nanotubes of diverse diameters and chiralities. However, they suffer from an intrinsic problem of precision: while designing classical potentials for either sp^2 or sp^3 carbon is relatively easy, nanotubes contain a combination of both bonds, a situation much more complicated to describe classically.

Here we aim at clarifying the existing controversies by performing accurate simulations of a large number of single-wall nanotubes with a variety of diameters and chiralities, in several setups. In view of the problem of precision of classical potentials in this context, we chose to stick to a quantum-mechanical description. As the use of density-functional theory would limit considerably the size of the systems that we could study, we chose therefore a more efficient alternative, namely the density-functional based tight-binding method (DFTB) [29, 30] explained in Chapter 2. This method is particularly good for carbon compounds as demonstrated in previous works [29, 96–98].

In the rest of this Chapter, we will first study the collapse of CNTs in a bundled configuration, using the bundle matrix as the pressure transmitting medium. Afterwards, in order to examine the effect of the PTM and the filling on the collapse, we will turn our attention to isolated, empty and water filled, carbon nanotubes in a water environment.

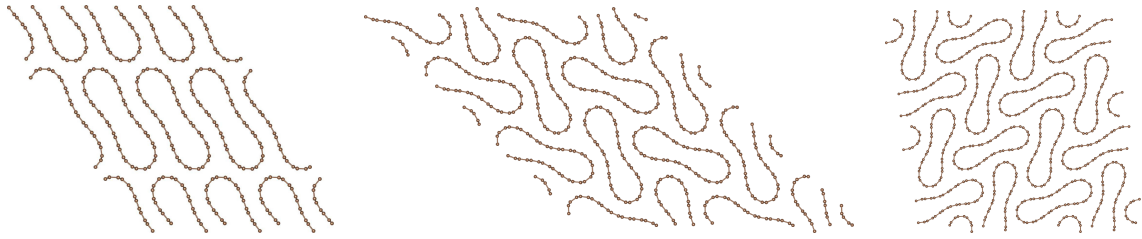


Figure 3.1 Collapsed bundle of (10,10) nanotubes in the case of 1 tube per cell (left), 2 tubes per cell (center) and 4 tubes per cell (right).

3.1 Carbon nanotubes bundles

We started performing quasi-static DFTB calculations on 69 single-wall carbon nanotubes bundles using the DFTB+ software package [99] (with the matsci-0-3 parameters set [100]). Since carbon nanotubes are relatively inert structures where no significant charge transfer is expected [96], we decided to adopt the non-self-consistent charge scheme of DFTB. It is true that there is a small charge transfer *after* the collapse as a result of the modified curvature [101], but this is not expected to affect the pressure at which the collapse takes place. Even if this form of tight-binding has already been extensively tested, we performed a simple validation test of our setup, by comparing the lattice constant of the (10,10) nanotube at ambient pressure (1.69 nm) with the experimental [102] 1.70 nm and DFT values [89] (1.65 – 1.69 nm, depending on the exchange and correlation functional and pseudo-potential used). The DFTB value is in very good agreement with both.

The set of systems under study includes basically all nanotubes with less than 300 atoms in the unit cell and with diameters up to 1.9 nm. Our simulations were performed using hexagonal unit cells containing 1, 2 and 4 nanotubes with periodic boundary conditions in the three directions. (For unit cells containing 4 tubes we included only nanotubes with less than 150 atoms due to the increased computation requirements.) A minimum tube length of 1.98 nm was assured in all cases, which corresponds to four primitive unit cells for the armchair nanotubes. The initial distance between the nanotubes in the bundle was set to 0.335 nm.

For each value of pressure, a random displacement of 0.002 nm was applied on each atom. After that, geometry and cell vectors were optimized until all the forces became smaller than 10^{-4} Ha/Bohr. The applied pressure was increased in steps of 0.2 GPa up to 30 GPa or until collapse. The collapse of the tubes is abrupt in the large majority of the cases and it was identified by a discontinuity in the Gibbs energy, that corresponds to the transformation to a peanut-like geometry. In some rare cases this discontinuity was not found and the collapse

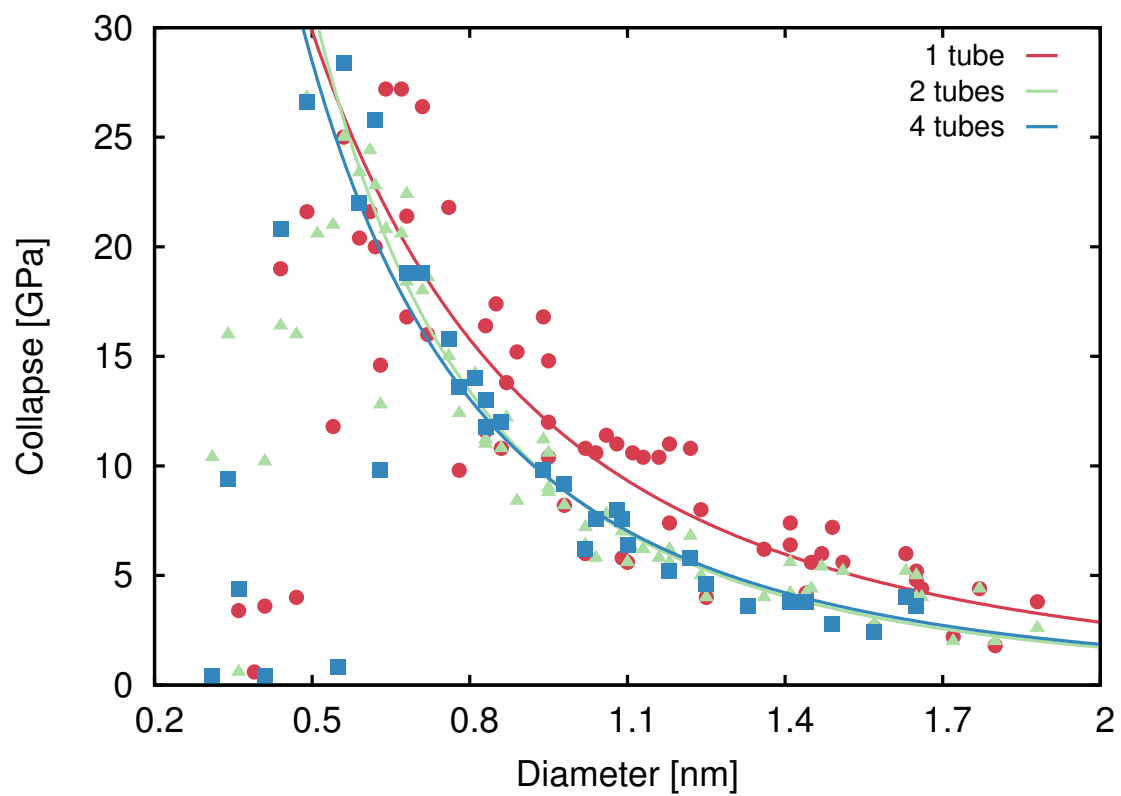


Figure 3.2 Collapse pressure as a function of the nanotube diameter for 1 (circles), 2 (triangles) and 4 (squares) nanotubes in the unit cell. The lines are fits obtained using Eq. (3.1).

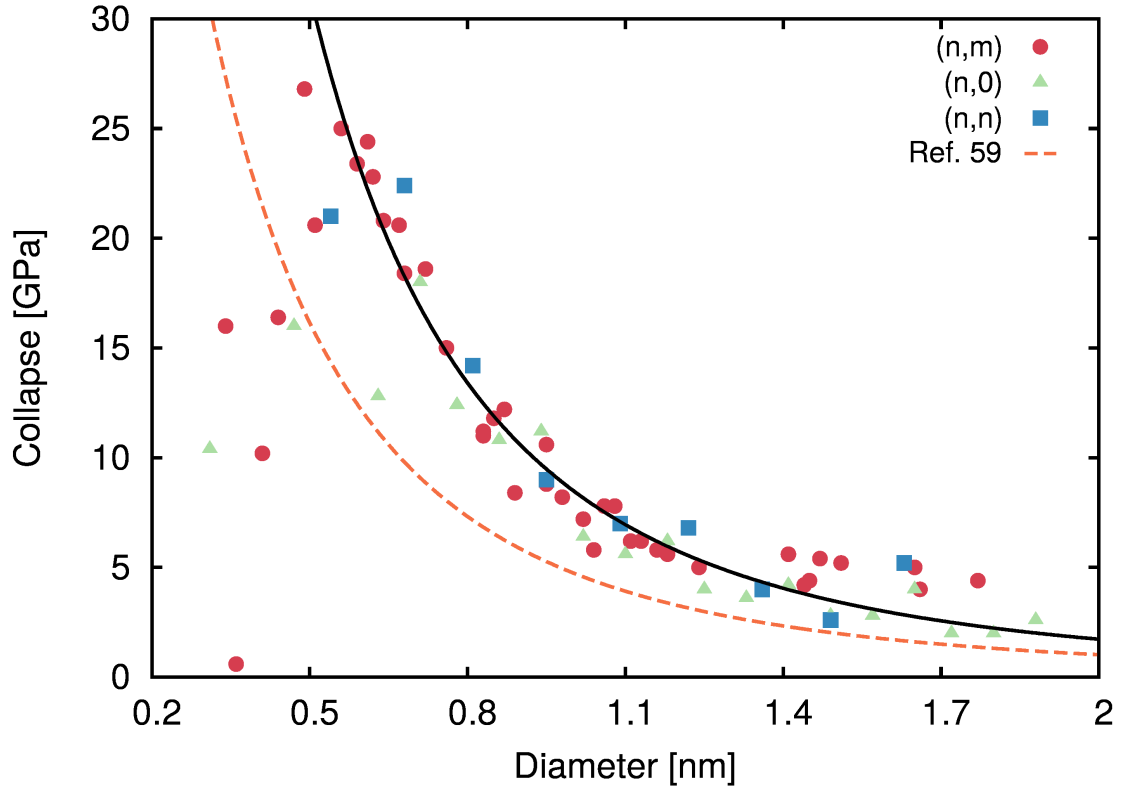


Figure 3.3 Collapse pressure as a function of the nanotube diameter for zig-zag, armchair and chiral nanotubes, using 2 CNTs per unit cell. The black line is the fit obtained using Eq. (3.1).

pressure was determined by inspection, *i.e.*, we assigned the collapse to the first peanut-like geometry found.

We start by analyzing how the number of tubes in the unit cell influences the collapse pressures. It is evident that having only one tube per unit cell is a large constraint, allowing only symmetric collapses, while having more tubes opens up other possible collapse channels (see Fig 3.1). To estimate how this influences the collapse pressure, we performed simulations using 1, 2, and 4 nanotubes per unit cell and maintaining equal all other parameters of the simulation. These results are summarized in Fig. 3.2. The two lines represent fits of the data for tubes larger than 0.6 nm diameter with the function

$$P_{\text{collapse}} = \alpha / (\beta + D)^3, \quad (3.1)$$

where D is the diameter. Fig. 3.2 shows that using 2 or 4 tubes per cell yields similar results, but having only one tube per cell leads to a much larger dispersion of the collapse pressures. This clearly proves that one tube per cell is not enough to describe correctly the bundle

interactions. A recent theoretical work [71] concluded that, for a comparable diameter of about 1.35 nm, the collapse pressure of an armchair single-wall carbon nanotube is several (13.75) times higher than the one of a zigzag nanotube. Our accurate calculations suggest that that result is likely to be an artifact of using only one tube in the unit cell. In particular, for (10,10) and (17,0) CNTs, our simulations yield collapse pressures of 3.4 and 3.6 GPa, to compare with the values reported in Ref. [71] of ~ 5.5 and ~ 0.4 GPa, respectively. The choice of using one tube per unit cell might be one of the reasons for the observed discrepancies in the results published in the literature.

As we proved that the differences between having 2 and 4 tubes are not significant, we will focus the rest of the discussion on the case of 2 tubes per unit cell for which we have results for more chiralities (see Fig. 3.3). The solid black line in Fig. 3.3 is again a fit using Eq. (3.1) (yielding $\alpha = 24.6$ GPa nm³ and $\beta = 0.4$ nm, while the dashed line reproduces the results of Ref. [59]). If we consider tubes with diameters above 0.6 nm, we find an overall good agreement with the well known D^{-3} behavior. However, below this value, the collapse pressures start to decrease with decreasing diameter. This may be related to the increased curvature of the graphene sheet that causes higher load on the C–C bonds. For small tubes, we even see for some chiralities the formation of interlinked sp³ structures connecting adjacent nanotubes after collapse. For really small nanotubes, such as the (5,0) and (7,0), these interlinked structures are already present at ambient pressure. The existence of these structures has been reported experimentally [103] and theoretically [89, 104, 105].

Quantitatively, we obtained collapse pressures that are roughly the double of the majority of other theoretical works based on classical potentials [59] (see Fig. 3.3). For nanotube diameters in the range of 1.2 to 1.5 nm, which typically correspond to arc-discharge carbon nanotube bundles, our calculated collapse pressures range from 3 to 7 GPa. As already explained, the experimental values for the collapse pressure are highly spread. We consider the case of arc-discharge bundles and only studies using either 4:1 methanol:ethanol or argon as pressure transmitting medium, which exhibit good hydrostatic conditions up to 10 GPa. Phase transformations towards collapsed forms were reported at 10 GPa using Raman spectroscopy [65, 75] or X-ray diffraction [84]. Other works [103] reported the collapse of arc-discharge bundles at pressures of 5 GPa. Our calculated values in the 3–7 GPa interval compare very well with the experimental values ranging from 5 to 10 GPa for arc-discharge carbon nanotube bundles.

In order to study the effects of chirality on the collapse, we plotted the collapsed pressure as a function of the chiral angle in Fig. 3.4 in the case of two tubes per unit cell. The diameter is represented by the color scale on the right. For the smallest nanotubes, chirality has a large influence in the collapse pressure, which can be understood as a consequence of the

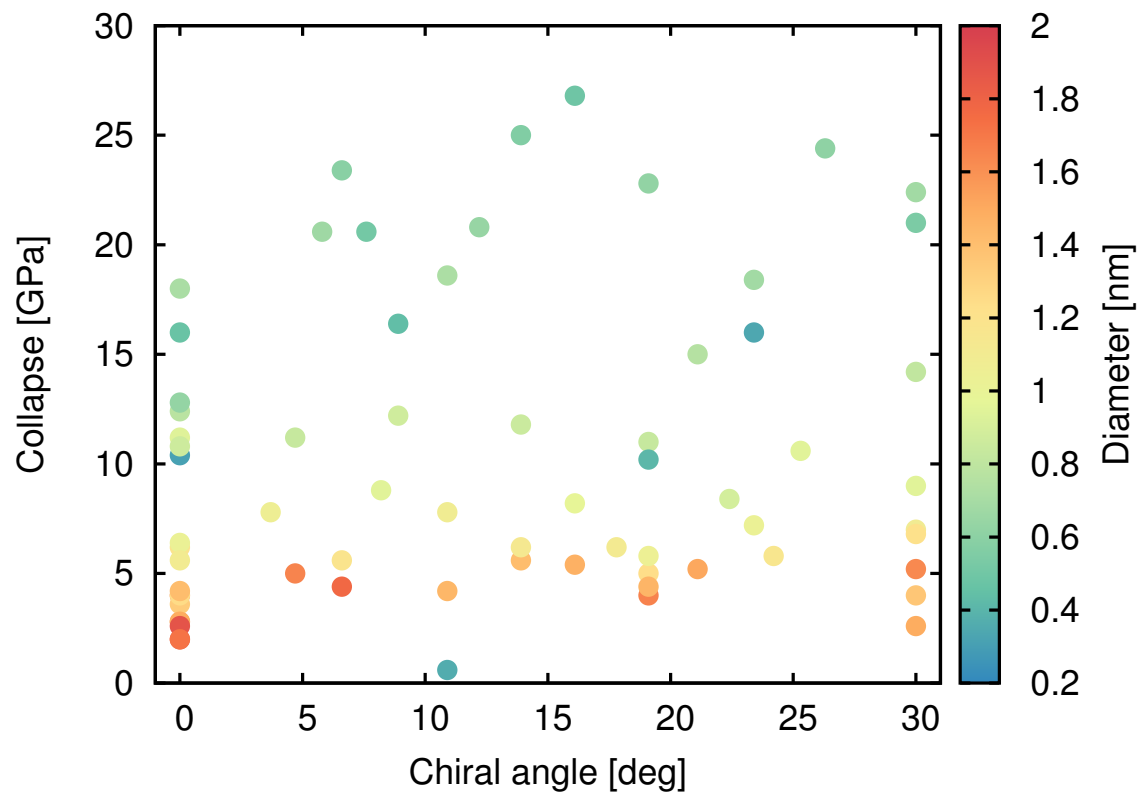


Figure 3.4 Collapse pressure as a function of the chiral angle calculated with two tubes per unit cell. The nanotube diameter is indicated by the color scale.

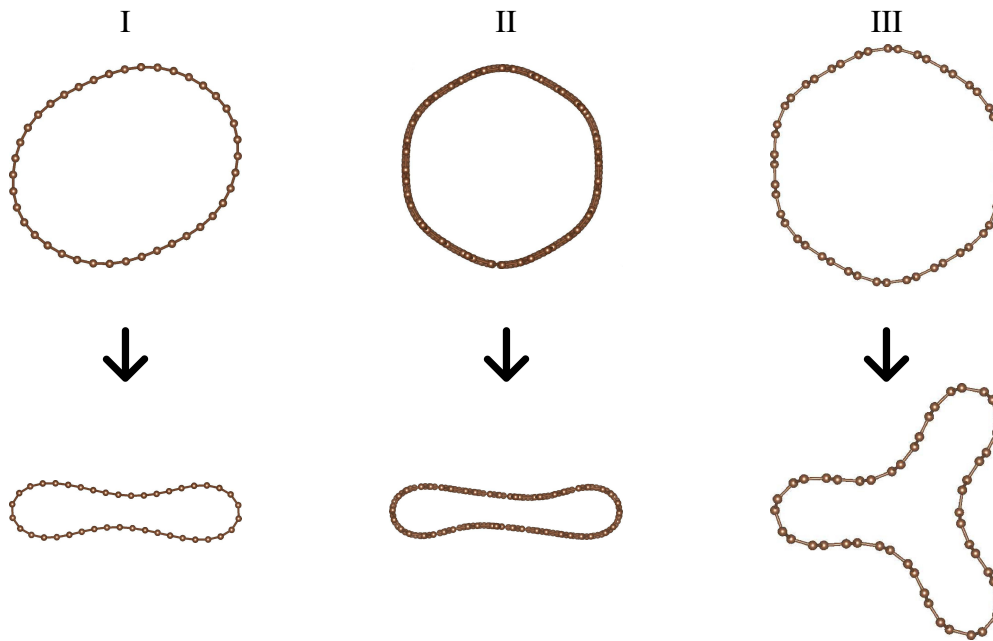


Figure 3.5 Collapse modes observed. From the top: Mode I, from ovalized to peanut geometry; Mode II, from polygonised to peanut; Mode III, from polygonised to star.

lower number of carbon atoms forming the nanotube wall, resulting in less cylindrical (more polygonised) nanotubes. For larger nanotubes no correlation between the chirality and the collapse pressure is noticeable.

Finally, we inspected the different possible collapse channels. We found three possibilities, as it is shown in Fig. 3.5. Mode I represents the transformation from ovalized to peanut, mode II the transformation from hexagonal to peanut and mode III from hexagonal to a star-like geometry. Figure 3.6 displays the collapse mode as function of the chiral angle and the nanotube diameter for unit cells containing 1, 2 and 4 tubes. The collapse mode depends slightly on the number of tubes in the unit cell used, and it depends strongly on the diameter and the chirality. As it was already noted by other authors [89], armchair nanotubes with chiral vectors $(3n+3, 3n+3)$ adopt a polygonised structure before collapse, whereas the remaining nanotubes collapse going through an ovalized structure. Interestingly, zigzag nanotubes with chiral vectors $(3n+3, 0)$ seem to collapse also going through a polygonal geometry. For other nanotubes, the collapse mode seems to be controlled by the diameter: small nanotubes ovalize and large ones polygonise. Evidences of polygonalised CNTs were also reported experimentally [106] for nanotubes with diameters around 1.7 nm.

With only one nanotube per unit cell, we observed in some cases the collapse to an unusual star-like structure. This structure was predicted to be a possible collapse mode [107],

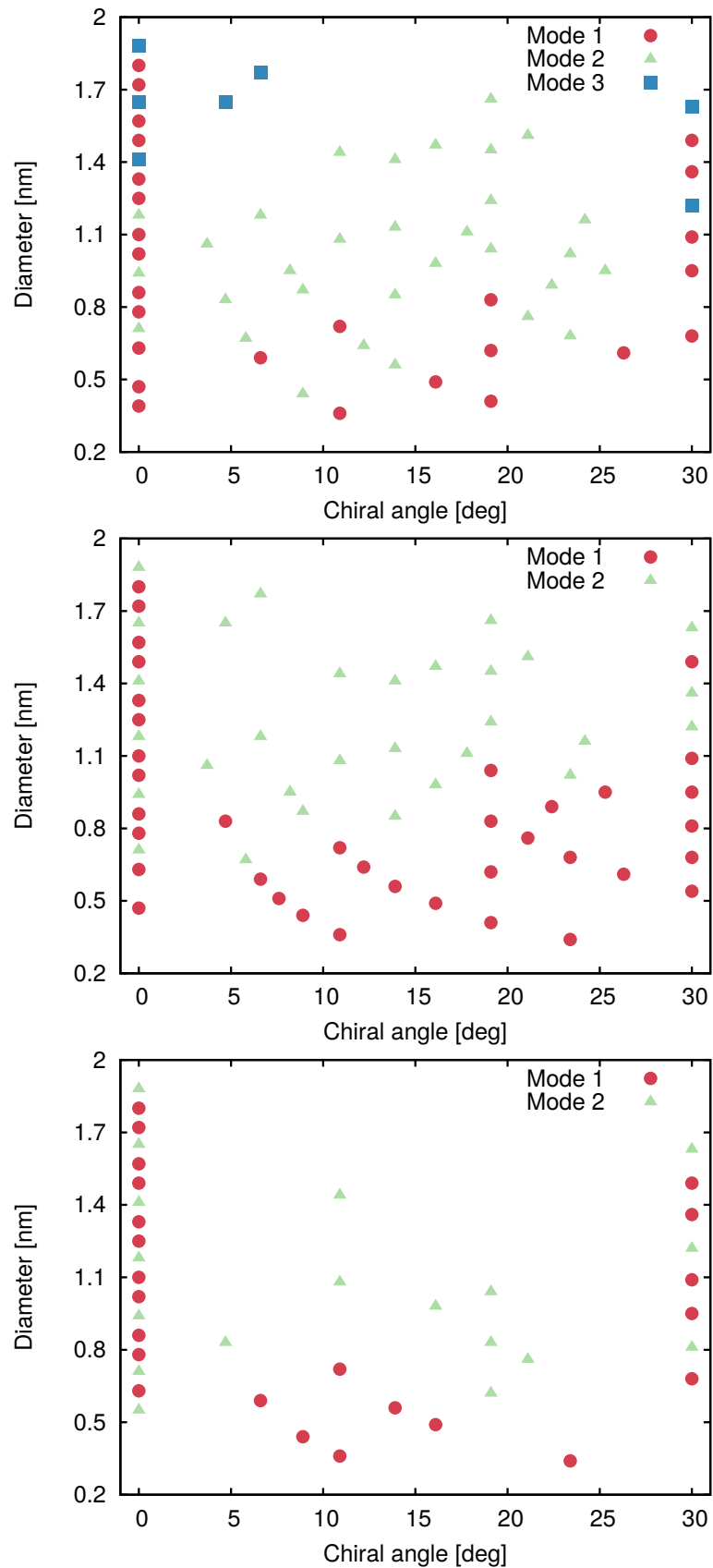


Figure 3.6 Collapse mode as a function of the diameter and the chiral angle of the nanotube. Top panel is for 1 tube per unit cell, the center for 2 tubes per cell, and the bottom panel for 4 tubes per cell.

although with a higher binding energy than the peanut geometry. We also noticed that the pressure range of polygonization is smaller than the one of ovalization.

It was shown in classical simulations [70, 86, 87] that the energetically most favorable arrangement of collapsed nanotubes is the one with parallel nanotubes. This was also seen in high-resolution transmission electron microscopy (HRTEM) experiments on collapsed double-wall bundles with large diameters [108]. Indeed, it is plausible that for very large diameters the most stable collapsed structure consists in parallel nanotubes, as this geometry maximizes the van der Waals interaction between the walls. However, for smaller tubes, it is also clear [70, 88] that other factors, such as the number of tubes in the simulation cell, the filling factor of the collapsed tubes, the environment, etc., may have a big influence on the collapsed geometry. In our simulations, the parallel geometry appeared for several bundles, while there were other cases where the herringbone geometry was found instead. We note, however, that the DFTB method does not describe accurately van der Waals interactions. Even if this contribution is small, it is of the order of the energy difference between the herringbone and the parallel arrangements (≈ 10 meV per atom), and it can therefore change the energetic ordering of the structures.

3.2 Individualized Carbon nanotubes in water

In this section, we investigate using the DFTB method, the effect of water on the pressure stability of empty and water-filled individualized SWCNT. In order to account for possible charge transfer processes we used the self-consistent charge density functional tight-binding scheme (SCC-DFTB) [31]. For the C–C interaction, we used the same parameters as for the CNT bundles. For the H–O–C, we chose to use parameters fitted to organic systems [31]. Our simulations were performed using hexagonal unit cells containing a four-unit-cell-long nanotube with periodic boundary conditions in the three directions. All the nanotubes were surrounded by water molecules, in enough number to assure that the distance between the nanotube and its periodic neighbor was larger than 10 \AA to avoid interactions between the tubes. Water molecules were put randomly around / inside the tube and a molecular dynamic thermalization was done at 370K followed by a rapid cooling to 10K. After that, geometry and cell vectors were optimized until all the forces became smaller than 10^{-4} Ha/Bohr. The applied pressure was increased in steps of 0.2 GPa up to 30 GPa or until noticeable collapse. With this setup it was not possible to simulate all the tubes we used for the bundles. For the empty CNTs in water, we used only armchair and zigzag nanotubes with diameters in the range 0.7 – 1.4 nm. For the filled case, we chose only the (8,8) and (10,10) nanotubes and

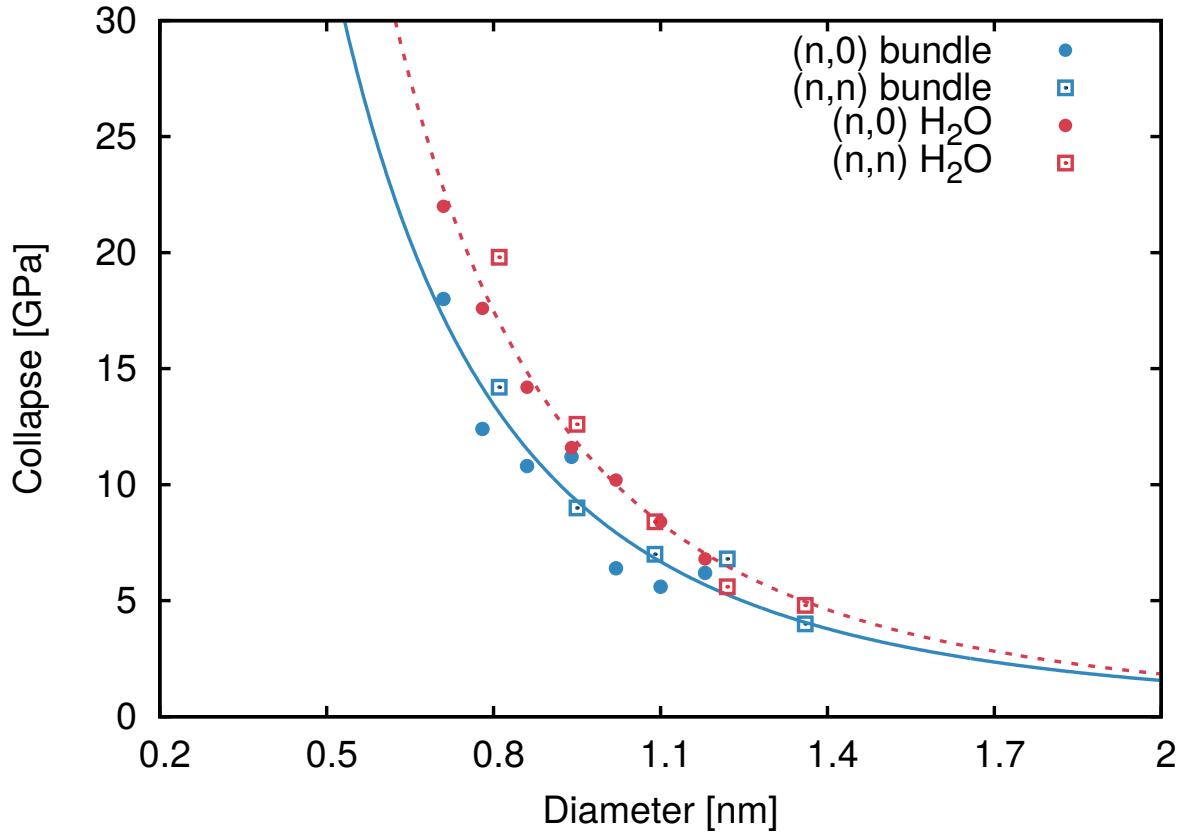


Figure 3.7 Comparison of the collapse pressure as a function of the diameter of bundles (blue) and individualized CNT in water (red). Squares are armchair and circles are zigzag nanotubes. The lines are fits obtained using Eq. (3.1).

pressures up to 15 GPa. We chose these nanotubes because their diameters are representative of the samples used in experiments.

Using the setup described above, we simulated the evolution with pressure of 12 empty CNTs in water. The results can be seen in Fig. 3.7. We fitted the values using the same Eq. (3.1) that we used for bundles. Here the parameters obtained are $\alpha = 21.7 \text{ GPa nm}^3$ and $\beta = 0.3 \text{ nm}$. For comparison, we also include the values and fit for the same tubes in the bundle configuration. We see that the overall behavior is the same as for the bundles, confirming again that the collapse pressure of single wall CNTs is determined mainly by its diameter. The collapse pressures are however slightly higher. For the largest diameters we have differences of around 5% whereas for the smaller we have around 15%. In the latter case, differences between bundles and individualized tubes are of the order of our pressure step. A snapshot of the initial structure at 0 GPa and the final geometry at 5.5 GPa for the (10,10) nanotube can be seen in Fig 3.8.

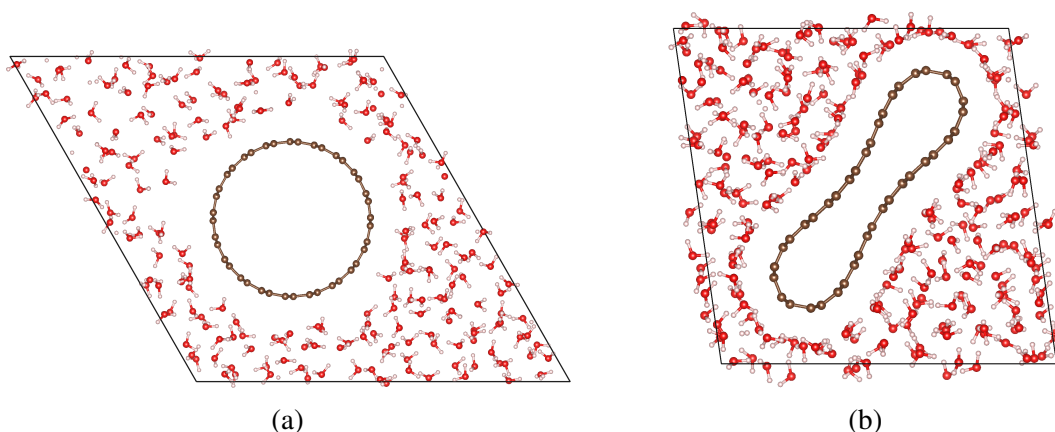
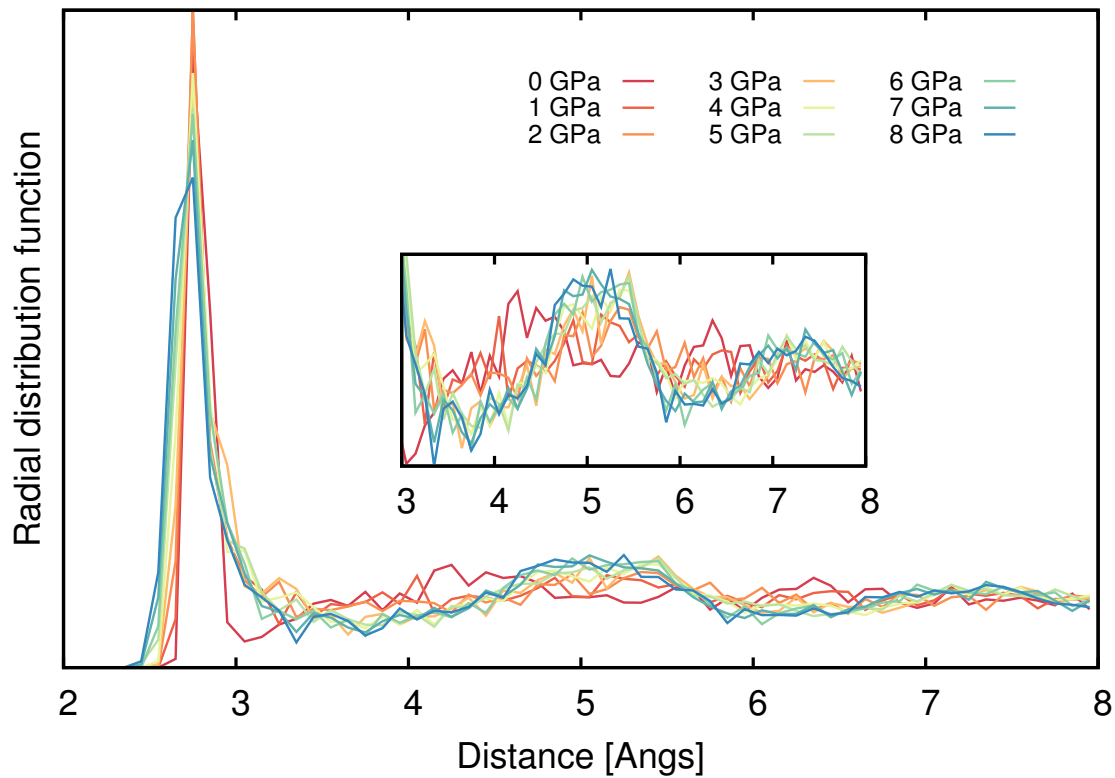


Figure 3.8 Snapshots for the (a) initial and (b) collapsed structures of empty CNTs.

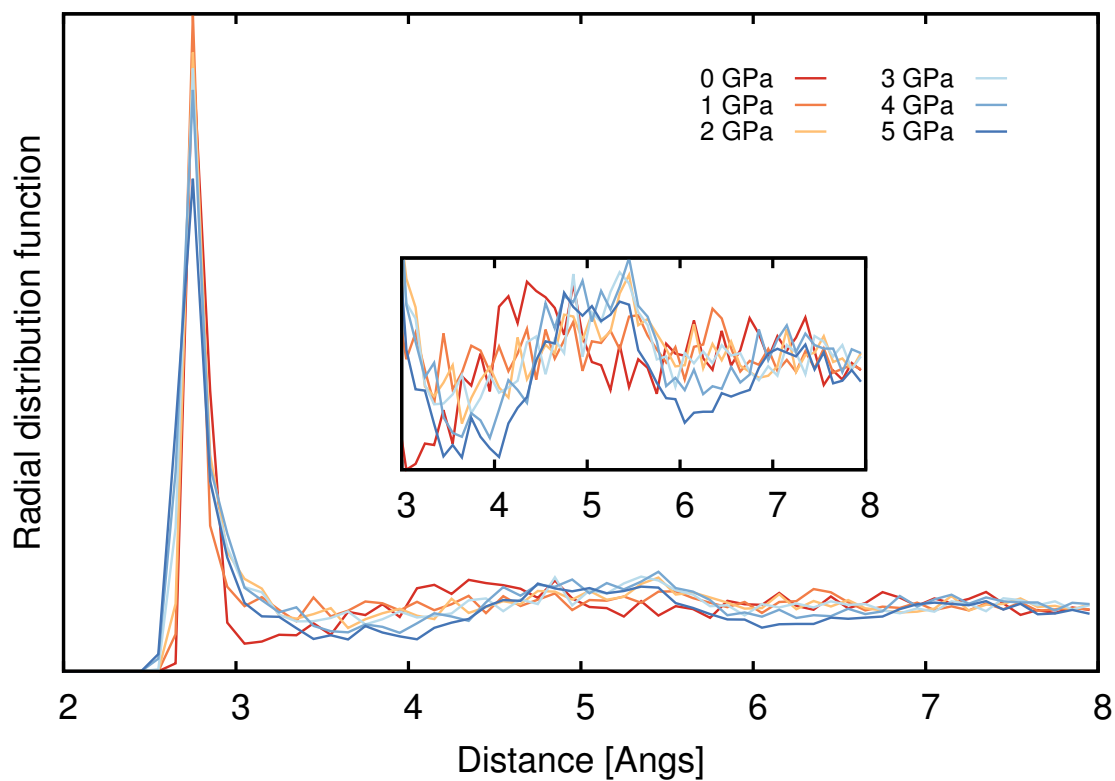
From Fig 3.7 we can also see that effects due to nanotube chirality are not present. This is consistent with the previous observations for bundles. In fact, the values obtained in this case seem to fit even better the expected d^{-3} behavior. This is not surprising since now we have a much more uniform PTM than with bundles, where geometric constraints were present. Also, we can now see that all the tubes ovalize, regardless of the chirality.

It is experimentally known that water loses hydrostatic conditions (crystallizes) at around 2 GPa. In order to check if our modeled water molecules are mimicking this effect, we plotted the O-O radial distribution function (RDF) as a function of pressure for the (8,8) and (10,10) tubes, as shown in Fig. 3.9. We can distinguish 2 groups in the RDF: one for the 0 – 2 GPa range, and another for the 3+ GPa pressure range. This suggests a transition between 2 – 3 GPa, in agreement with the observed crystallization of water at 2 GPa. Of course, we are not reproducing exactly the experimental conditions, but this gives us confidence to compare directly our simulations with experimental data. Experimental works estimated the collapse pressure of individualized CNTs with diameters in the range 0.8 – 0.9 nm, 1.2 – 1.3 nm and 1.24 – 1.4 nm to be of 10 GPa [109], 4 GPa [109] and 3.85 GPa [66], respectively. Taking these average diameters and using our fit, we obtain collapse pressures of 16.3 – 12.6 GPa, 6.4 – 5.3 GPa and 5.9 – 4.4 GPa. Differences can arise either from differences of the nanotube environment in experiments (surfactants and impurities) and calculations, from approximations needed in the calculations or from differences in the criteria of determination of full collapse in experiments and calculations.

We turn now our attention to the effect of water-filling on the pressure stability of individualized (8,8) and (10,10) SWCNT. The filling of arc-type SWCNT (comparable to the (10,10)) was experimentally estimated to be between 11% to 29% of total weight fraction of fully filled nanotubes (Ref. 110 and references therein). We studied the evolution with



(a)



(b)

Figure 3.9 O-O radial distribution function for the (8,8) (upper panel) and (10,10) (lower panel) empty CNTs in water as a function of pressure, with a zoom in the region 3–8 Å.

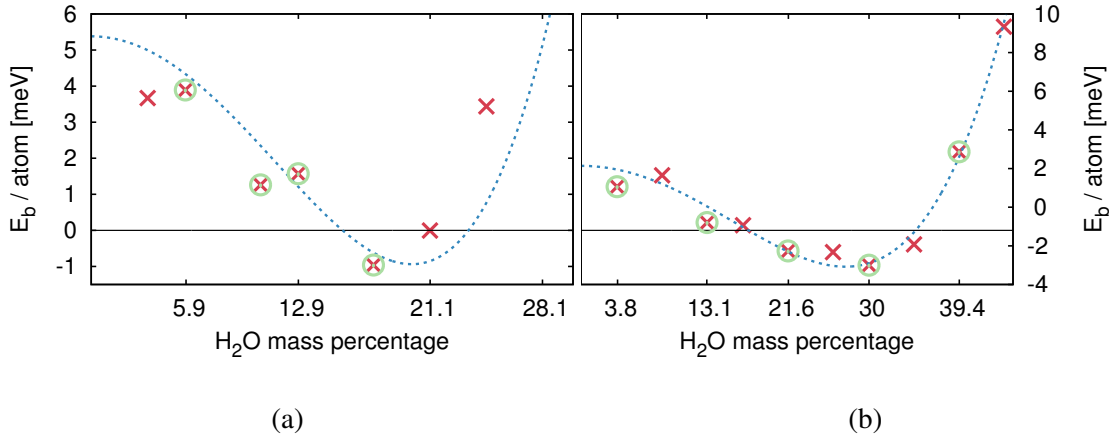


Figure 3.10 Binding energy per atom for the (8,8) (a) and (10,10) (b) nanotubes as a function of the water concentration. Red crosses are filled tubes in vacuum, green circles mark the cases where we also calculated the tube in water.

pressure for filling concentrations of water of 6.2%, 11.3%, 16.3% and 20.0% for the (8,8) CNTs and 3.8%, 13.1%, 21.6%, 30% and 39.4% for the (10,10) CNT. The optimum filling ratio for the (8,8) and (10,10) with our model was estimated to be between 15% to 23% and 17% to 35%, respectively. These values were estimated looking at the binding energy (E_b) per atom of the system composed by the nanotube plus water molecules (see Fig 3.10), calculated as:

$$E_b = E_{filled} - (E_{empty} + E_{H_2O} \times N_{H_2O}) \quad (3.2)$$

where E_{filled} is the energy of the tube filled with N_{H_2O} water molecules, E_{empty} is the energy of the empty, isolated tube and E_{H_2O} is the energy of one water molecule. It is noticeable from Fig. 3.10, specially for the (8,8) CNT, the presence of effects due to the finite length of the nanotube. Therefore, for a more precise estimation of the optima filling ratios, calculations using longer nanotubes are need.

In Figs. 3.11 and 3.12 we show the pressure dependence of the nanotube volume as a function of different water-filling ratios. The collapse of the tubes is abrupt in the case of empty tubes and in that case, the collapse pressure was identified by a discontinuity in the Gibbs energy, that corresponds to the transformation to a peanut like shape. In the case of filled tube where we have a smooth collapse process, the collapse pressure was determined by inspection, i.e., we assigned the collapse to the first peanut-like shape found. As these are continuous processes it is hard to identify precisely the collapse point. Rather, the values suggested should be regarded as the starting of the collapse process, where the tube is not anymore ovalized. Another important note is that we observe several kinds of collapses. In

Table 3.1 Number of water molecules (N_{H_2O}), water-to-carbon mass percentage (w/w) and collapse pressure (P_c) of the water filled: (left) (8,8) with $d = 1.09$ and (right) (10,10) with $d = 1.36$ CNTs.

N_{H_2O}	w/w [%]	P_c [GPa]	N_{H_2O}	w/w [%]	P_c [GPa]
0	0.0	8.4	0	0.0	4.8
5	5.9	7.4	4	3.7	4.8
9	10.5	8.6	14	13.1	5.8
12	14.1	10.2	23	21.6	5.8
15	17.6	12.6	32	30.0	6.2
			42	39.4	—

most of the cases, we see a first transition marked by a large drop in volume followed by second at higher pressures. The first is mainly related to the transformation of the nanotube shape, whereas the second is related to a reorganization of the water molecules inside the nanotube. Depending on the percentage of water filling and on the nanotube diameter, this can lead to 2D water structures like water sheets (Figs. 3.11d, 3.11f, 3.11h and 3.12d) or 3D structures like water-nanotubes (Fig. 3.12h). A plethora of different confined water structures has already been reported either experimentally or by the means of molecular dynamic simulations [111–119]. The structures we obtained are not fundamentally different to the ones already reported. Nevertheless, our results prove that CNTs can be used as *nano-anvils*, in order to obtain in a controlled way confined structures with varying dimensionality just by changing the pressure applied into the system, and by varying the diameter of the nanotube.

Let us now turn to the water-filling effect on collapse. Table 3.1 lists the obtained collapse pressures for several filling ratios, including also the value for the correspondent empty tube for comparison. For the lowest calculated water filling ratios, we observe a slight reduction of the collapse pressure which is followed by a steady increase of its value with increasing water content. This lower collapse pressure is not surprising if we consider that our calculation show a tendency of water molecules to cluster, which would then lead to a meniscus surface tension effect and act equivalently to an additional pressure. In fact, if we look at Figs. 3.11 and 3.12 we see that at low filling, the first volume modifications appear at pressures close to the collapse pressure of the empty tube, for both tubes. This is in agreement with observations on both RBM and G-band of filled CNTs [66]. At higher water content, the collapse pressure increases with respect to the empty tube case. In the case of a (10,10) tube, the collapse pressure of the filled tubes lies between 5.8 and 6.2 GPa. This pressure domain does not agree well with experimental observations in Ref. 66, where collapse pressures of 14 – 17 GPa were measured. However, in experiments it is not possible to prevent water

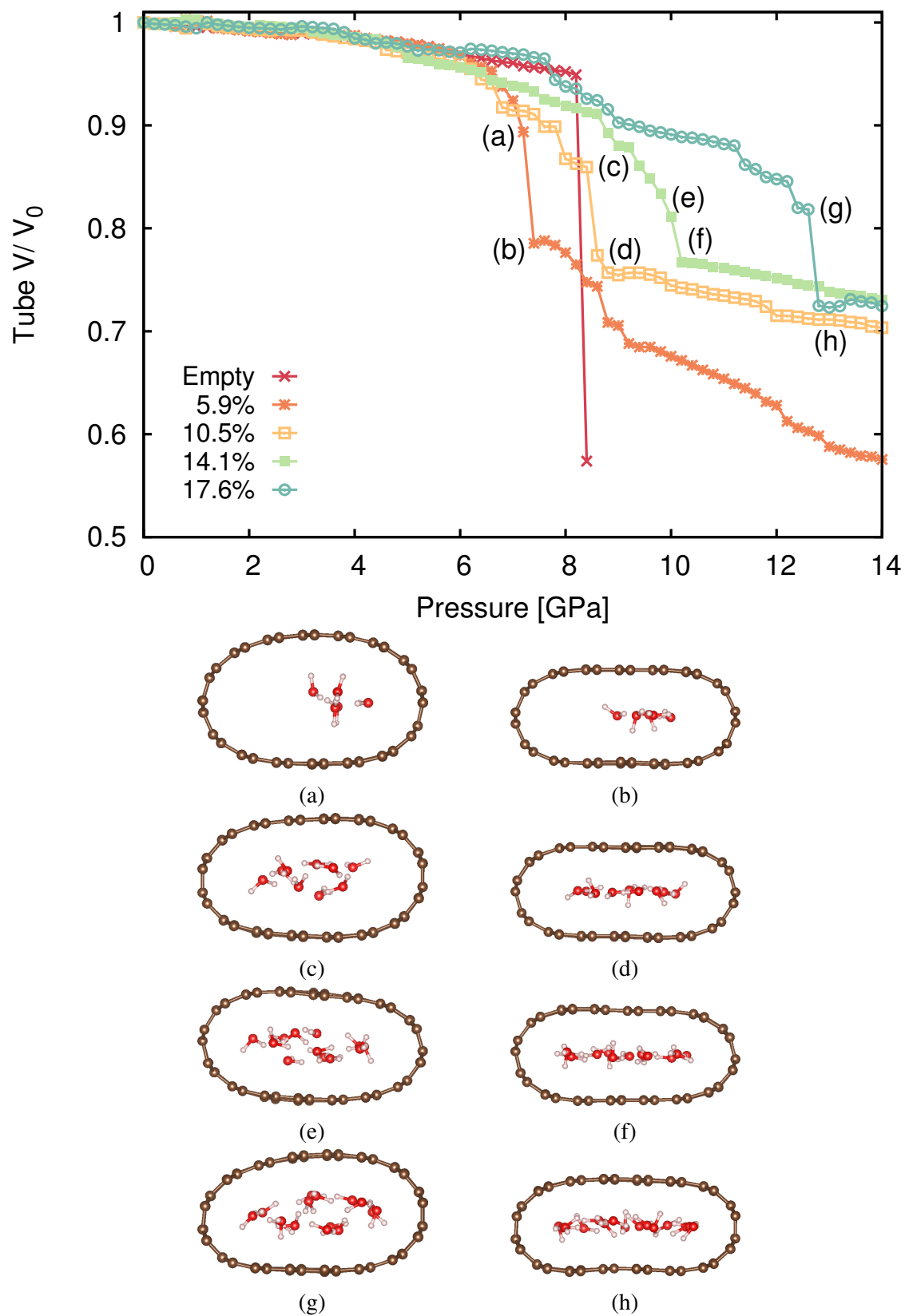


Figure 3.11 Upper panel: variation of volume for the (8,8) nanotube as a function of pressure. Lower panel: some snapshots.

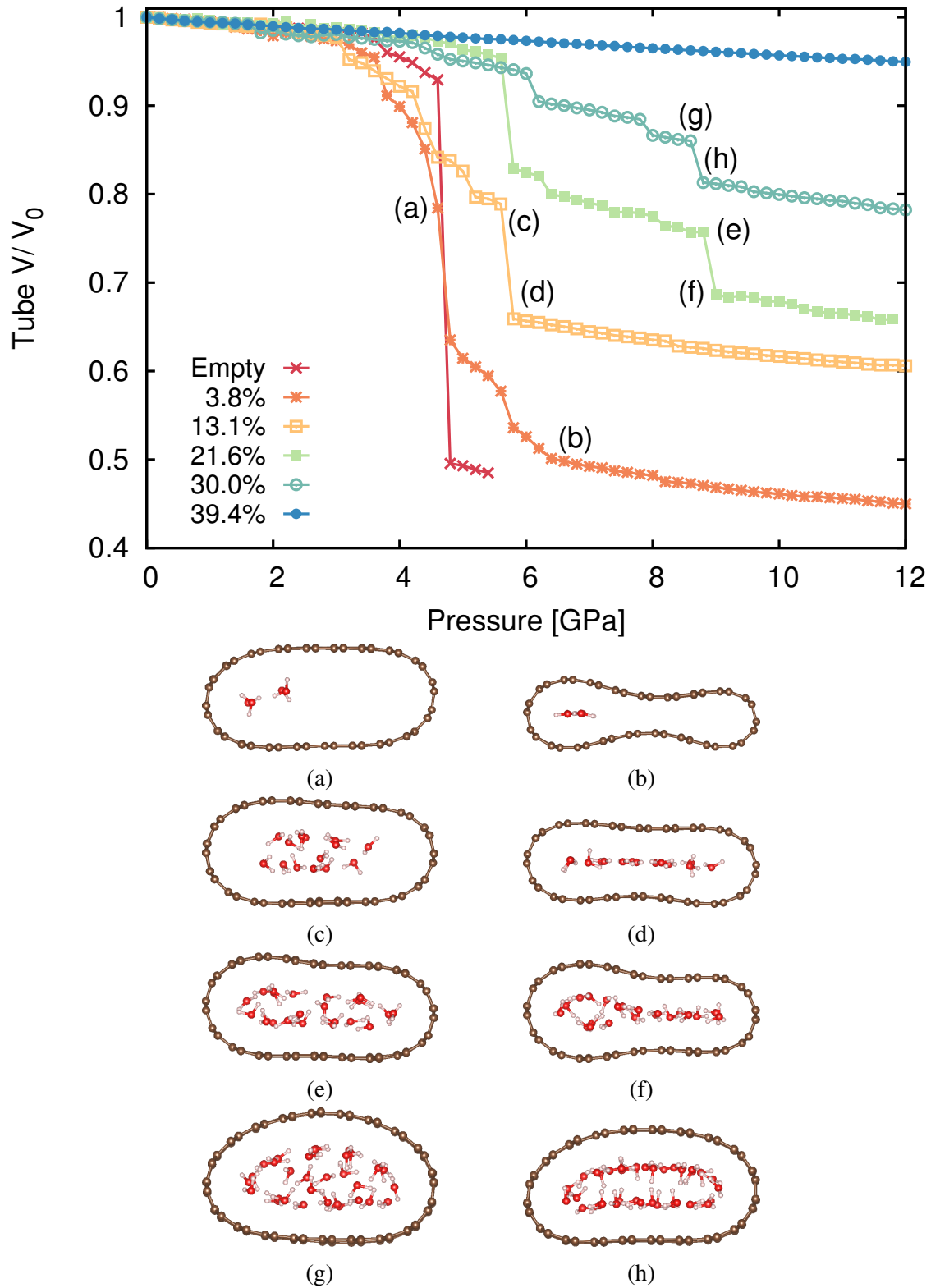


Figure 3.12 Upper panel: variation of volume for the (10,10) nanotube as a function of pressure. Lower panel: some snapshots.

filling to increase under the effect of increased pressure, up to the PTM solidification which, for water, takes place at ≈ 2 GPa. At 2 GPa, liquid water increases its density by 33% and if we consider that this is fully translated in an increase of the water-filling ratio, we would reach a filling value above 42%. In our simulations, for a similar water-filling ratio, we could not see any collapse up to 15 GP.

3.3 Summary and Conclusions

The collapse of carbon nanotubes has been subject to several theoretical and experimental studies over the years. However, contradictory results can be found in the literature between theory and experiments. Even considering only theoretical studies, divergent results can be found. By using a large set of nanotubes of different diameters and different chiralities in combination with a higher level of theory than what is commonly applied, we found several key factors that can justify these apparent contradictions.

For CNTs bundles, concerning the calculated collapse pressures, we showed that the discrepancies found in the literature can be explained by the different number of carbon nanotubes in the unit cell and by the theoretical framework employed. Furthermore, using a quantum-mechanical approach, we obtained collapse pressures that are about twice as large as the ones obtained with classical potentials. The chirality of the nanotube does not show a strong influence on the collapse pressure for nanotubes bundles with diameters above 1 nm but it can be significant for smaller diameters. From our results, we estimate that carbon nanotubes bundles with diameters of around 0.6 nm are the ones with the highest collapse pressures. Regarding the collapse modes, armchair and zigzag nanotubes polygonise before collapsing to a peanut geometry if their chirality equals $(3n + 3, 3n + 3)$ or $(3n + 3, 0)$, whereas in the other cases the nanotubes adopt oval cross sections before collapsing. For chiral nanotubes, the collapse mode seems to be independent of the chiral angle, being the diameter the underlying factor. From these results, we can conclude that there are two key ingredients that are mandatory to perform quantitative simulations of the collapse process of carbon nanotubes under pressure: (i) a quantum mechanical description and (ii) large unit cells containing several tubes. In our opinion all previous literature on the subject should be critically reviewed based on this consideration.

For individualized CNTs in water, we see an increase of the collapse pressures compared to the case of bundled CNTs, even for empty nanotubes. On the other hand, and similarly to the case of bundles, we do not notice any systematic chirality influence on the collapse pressure. Furthermore, we see that all tubes ovalize, regardless of the chirality. For water filled CNTs we see different behaviors, depending on the filling ratio. We estimated optimum filling

ratios for (8,8) and (10,10) CNTs to be around 15% – 23% and 17% – 35%, respectively, which compares well with available experimental data. We observe that low filling ratios tend to destabilize slightly the CNTs, leading to modifications on the CNT cross section at lower pressures than for empty tubes. For (10,10) tubes, this effect precipitates the collapse at lower pressures, but it does not seem to affect the collapse pressure of the (8,8) tube. However, as there is an underlying error in the calculations (and a pressure step of 0.2 GPa), we can not rule out that a reduction can also happen in this case. In fact, all evidences seem to indicate a little or to no dependence at all on the chirality, at least in a predictable and systematic way. For higher concentrations of water, we see a consistent increase in the collapse pressure with the increased filling ratio, in accordance with experimental data, even if the calculated collapse pressures do not match perfectly experimental data. However, we think this can be justified by the increase of the water filling (the tube ends are open) during the pressure cycle. Regardless of the filling ratio, we notice a dramatic change in the collapse process of filled CNTs. While we had abrupt transformations of the nanotube cross section for empty tubes (and also for the majority of the bundles), we see a continuous collapse process for filled CNTs. We can identify two different steps - the first, related to the regular transformation of the CNT shape, followed by a reorganization of the CNT filling molecules that allows for a further modification of the CNT shape at higher pressures. Finally, we observe that unusual states of water can be found in the collapsing / collapsed nanotubes. These can range from nanotube-like to 2D sheet-like planes of water, depending on the diameter of the CNT and on the pressure. We can also speculate that, likewise, other pressure transmitting mediums may adopt exotic arrangements when confined, and that CNTs under pressure may be used to study novel molecular structures.

Chapter 4

Type-I Silicon Clathrates

Clathrates form a class of fairly special materials based on a host-guest structure which consists in a regular lattice of cages in which guest atoms or molecules are encapsulated. Strictly speaking, clathrates are the duals of the intermetallic phases known as Frank-Kasper structures which contain only tetrahedral interstices, and that are closely related to a family of quasicrystals [120, 121].

Since the seminal work of Cros *et al.* [122, 123], who synthesized the first Si clathrates in 1965, many inorganic, group-IV, clathrate phases are by now known [124]. These are commonly described in a first approach as cubic solids with a unit cell composed of large cages of silicon, germanium, or tin. Their stability and their electrical properties (metal or semiconductor character) are, in a first approximation, fully understood in terms of the so-called Zintl-Klemm (ZK) rule (or charge balance rule) [125–129]: assuming that every guest atom in the cages completely donates its electrons, the structure maximizes its stability when each framework atom realizes an electron-octet. This can be achieved by doping the framework with acceptor/donor atoms. Typical examples of Zintl phases are compounds of the form $A_aX_x = (A^{n+})_a(X^{an/x-1})_x$, where A is an active metal, X a noble (electronegative) metal or semimetal, and n is the number of electrons transferred from the active metal to the acceptor atoms.

The superconductivity found in silicon clathrates is based on a strong covalent sp^3 network and has attracted much attention for the past decades [130]. More recently, inorganic clathrates have been widely investigated in the field of thermoelectricity: the electronic conduction is insured by the cage-framework and the band gap can be easily tuned thanks to the many possible substitutions of framework elements, giving raise to metallic or semiconducting behavior [131]; On the other hand, the unit cell complexity and the host-guest interaction are responsible for the depression of the heat carrying acoustic phonons resulting in a very low lattice thermal conductivity [132–134], without affecting the electronic conductivity.

Thus, although they are crystals, clathrates are very poor heat conductors, while offering a wide range of electronic properties. They are therefore a perfect example of Slack's concept of a phonon-glass and electron-crystal [135–137].

It is not surprising that an important experimental and theoretical research effort has been devoted to find and optimize the functional properties of clathrates. In this quest, the ZK-rule serves as an important guide to select among all the possible combinations of substitutions in the different crystallographic sites of guest and host atoms. However, although most clathrates are Zintl-phases from the point of view of their formal electronic structures, some of their properties cannot be explained in terms of the Zintl concept and violations of this rule were observed, notably in clathrates containing transition metal elements [136, 138].

Here, we go beyond the ZK-rule, and use density-functional theory to screen the stability of a very large number of silicon clathrate phases. Our methodology is based on high-throughput calculations [34] and involves trying out all possible combinations of guest and framework atoms. We consider the case of the very popular and heavily documented ternary type-I Si clathrates [124], whose general chemical formula is $A_8X_xSi_{46-x}$. To study this ternary composition, we do not make any *a priori* assumption on which dopants could lead to stable clathrate phases. Instead we use all elements of the periodic table up to Bi, with the exception of the rare-gases, the lanthanides, and the actinides. It is worth noting that a few silicon clathrate systems containing lanthanides exist, namely $Ba_7LaAu_6Si_{40}$ and $Ba_7CeAu_6Si_{40}$ (see Refs. 139, 140). However, all the known phases have more complex doping ratios than the ones studied here. This can be something worth studying in future works.

4.1 Details of Calculations

To estimate the stability of a given composition we use as criterion the distance to the convex hull of thermodynamic stability (for a description, see Section 2.5). It is worth underlying here that for ternary and multinary systems this criterion is much more relevant than the commonly used formation energies, which only measure the decomposition in elementary phases. Indeed, we found several cases where, despite the low formation energy, the distance to the convex hull was large due to the possible decomposition into other binary or ternary phases, thus destabilizing the structure.

For each system we perform a full geometry optimization, including both the ion positions and the lattice, with the code VASP [39, 40]. The pseudopotentials are taken from version 5.2 of VASP to guarantee compatibility with the Materials Project database [4], and we use the Perdew-Burke-Ernzerhof approximation [141] to the exchange-correlation potential. For

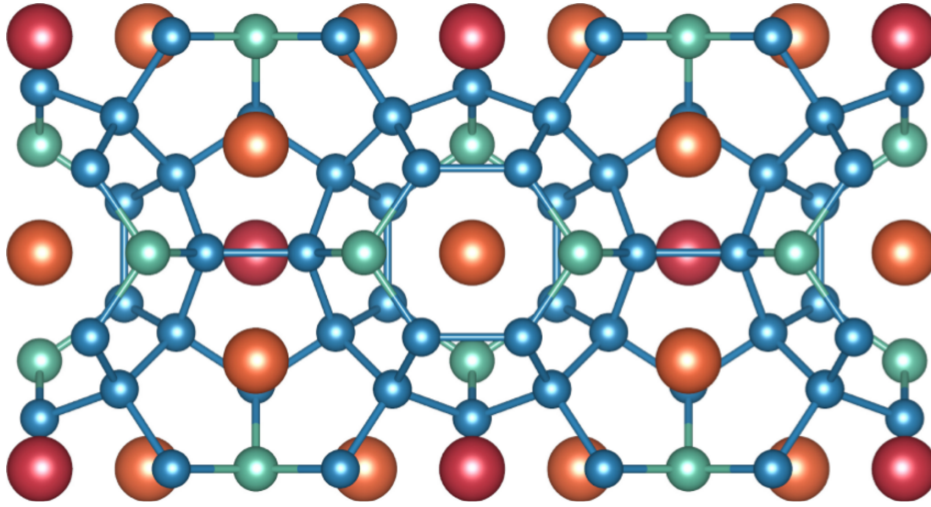


Figure 4.1 The type-I clathrate structure with different atoms indicating the relevant Wyckoff positions of the cubic space group #223: $16i$ and $24k$ (blue), $6c$ (green), $2a$ (red), and $6d$ (orange).

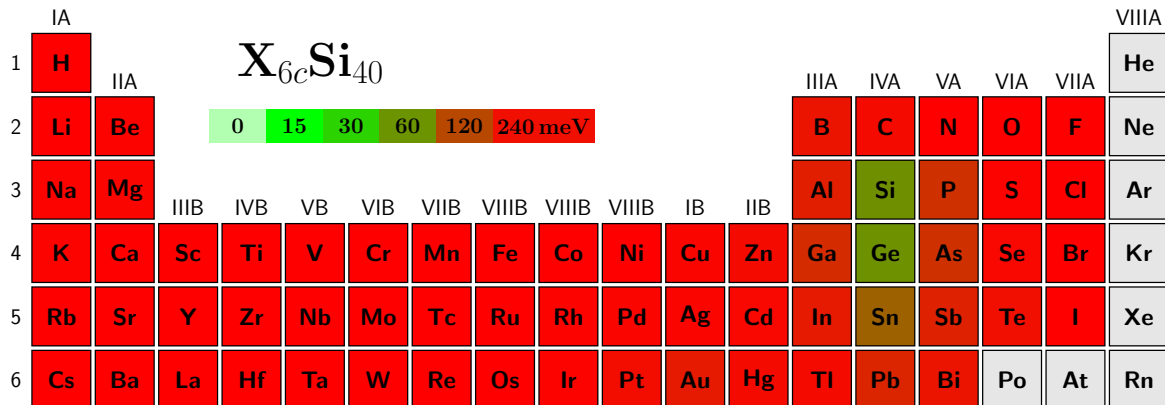


Figure 4.2 Distance to the convex hull (in meV per atom) for the clathrate $X_{6c}Si_{40}$.

the final calculation of the energy we use a cutoff of 520 eV and a $5 \times 5 \times 5$ k-point grid. This ensures convergence of the total energy to better than 2 meV/atom. The distance to the convex hull is calculated by comparing the energy of the system under investigation to all possible decomposition channels to materials present in the Materials Project database [4].

The type-I clathrate structure is depicted in Fig. 4.1. In the pure Si_{46} clathrate all the Wyckoff positions $16i$, $24k$, and $6c$ are occupied by Si atoms, and the $2a$ (center of small cages) and $6d$ positions (center of large cages) are empty. This is our reference structure that turns out to be 63 meV/atom above the convex hull, on which lies the standard diamond structure of Si. Endohedral doping can be achieved by filling either the $2a$ positions, the $6d$ positions, or both. Further (co-)doping can be achieved by substitution of the $16i$, $24k$, and $6c$



Figure 4.3 Distance to the convex hull (in meV per atom) for the clathrate $X_{2a}Si_{46}$ (a), $X_{6d}Si_{46}$ (b), and $X_{(2a+6d)}Si_{46}$ (c). The circles denote phases with similar stoichiometries that were synthesized experimentally: X_8Si_{46} ($X=Na, K, Rb, Cs, I$) [142–145]

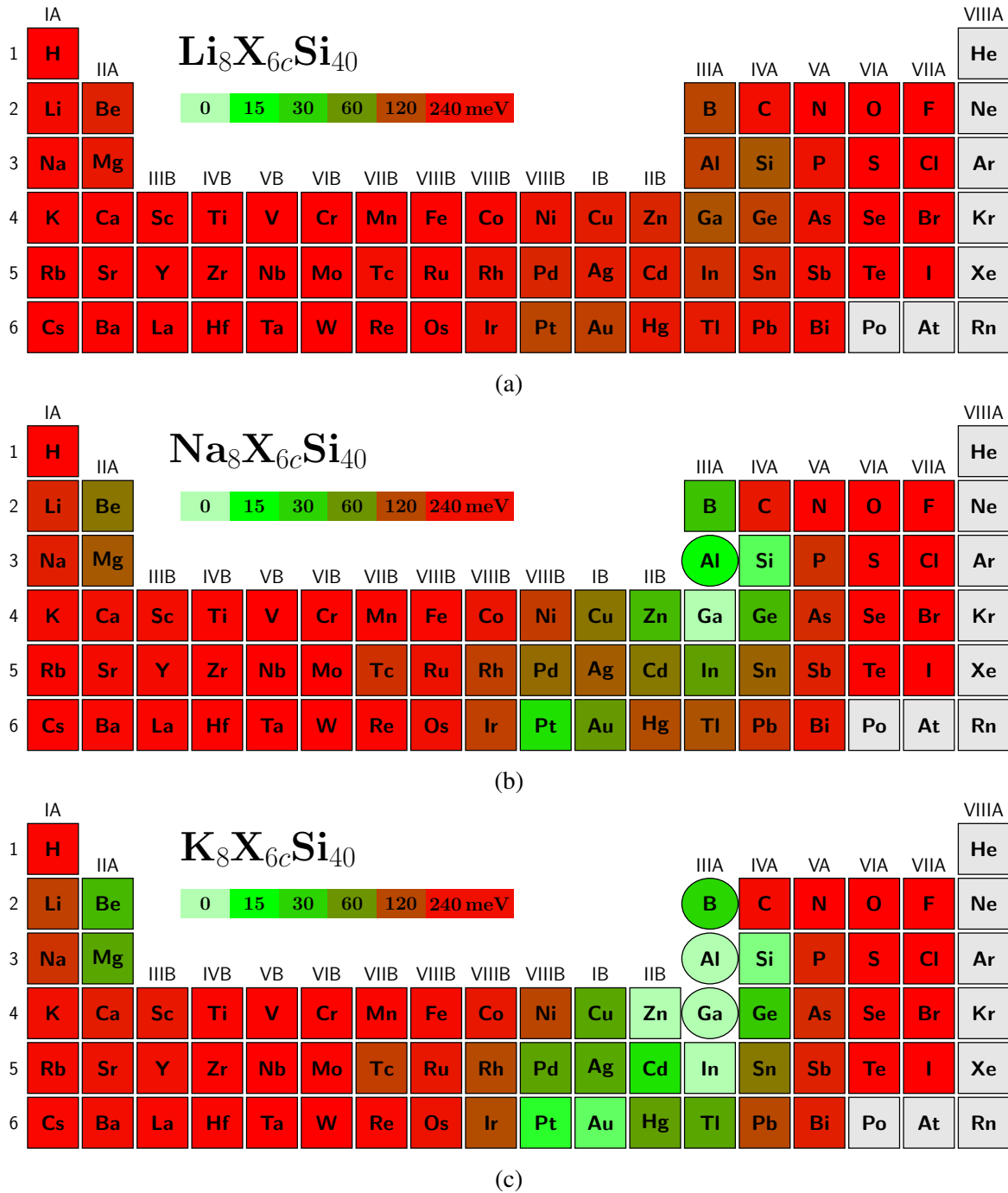
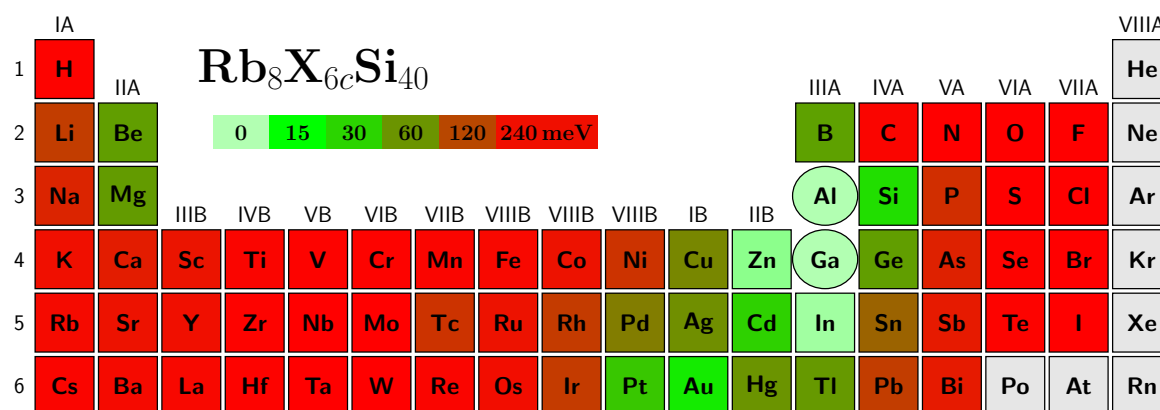
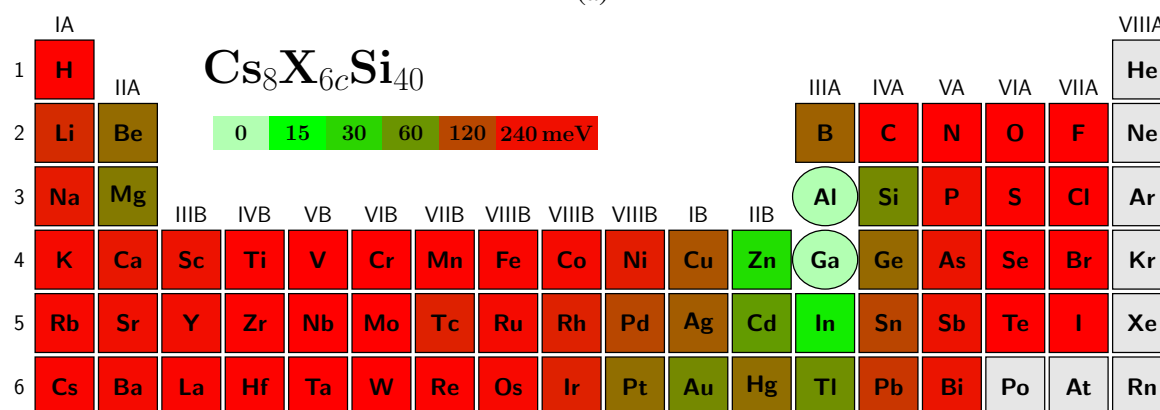


Figure 4.4 Distance to the convex hull (in meV per atom) for the clathrate $Z_{6d+2a}X_{6c}Si_{40}$ where Z is (a) Li, (b) Na, (c) K. The circles denote phases with similar stoichiometries that were synthesized experimentally [146]: $Na_8X_{6c}Si_{40}$ (X=Al) [147], $K_8X_{6c}Si_{40}$ (X=B, Al, Ga) [148–150]



(a)



(b)

Figure 4.5 Distance to the convex hull (in meV per atom) for the clathrate $\text{Z}_{6d+2a}\text{X}_{6c}\text{Si}_{40}$ where Z is (a) Rb and (b) Cs. The circles denote phases with similar stoichiometries that were synthesized experimentally [146]: $\text{Rb}_8\text{X}_{6c}\text{Si}_{40}$ (X=Al, Ga) [150, 151], $\text{Cs}_8\text{X}_{6c}\text{Si}_{40}$ (X=Al, Ga) [150, 152].

positions. This latter is experimentally known to be the most favorable, and our calculations corroborate this fact. In the following we will therefore focus on the substitution of $6c$ Si atoms.

4.2 Results and Analysis

We started studying the stability of the empty cages by replacing the $6c$ Si atoms, as shown in Fig. 4.2. The color scale denotes the distance to the convex hull, where green means less than around 50 meV/atom from the hull. Furthermore, circles mean that a similar stoichiometry was synthesized experimentally. All elements (with the unsurprising exception of Ge) occupying the $6c$ position destabilize considerably the Si clathrate framework. Then, we filled the $2a$, $6d$, and the $6d + 2a$ positions individually, while preserving the Si cage (Fig 4.3). As can be seen, several guest elements in the $2a$ position lead to a slight stabilization, but the largest effect was obtained occupying the $6d$ or the $6d + 2a$ positions. Results are in good agreement with published experiments, as the elements Na (7 meV/atom above the convex hull if all cages ($2a+6d$) are filled, 20 meV above the convex hull if $6d$ sites only are filled), K (4 meV/atom in $2a+6d$ and 3 meV in $6d$), Rb (26 meV/atom in $2a+6d$ and 11 meV in $6d$), Cs (65 meV/atom in $2a+6d$ and 31 meV in $6d$) yield already nearly thermodynamically stable phases. Indeed, these clathrates were already reported experimentally [142–144]. The only exception is the iodine compound that has been reported experimentally [145], but that in our calculations is more than 130 meV above the hull. We note, however, that this iodine structure was synthesized at high pressures and high temperatures, and that the experimental stoichiometry $\text{Si}_{44.5}\text{I}_{9.5}$ suggests that this cationic clathrate is likely to have a more complicated structure than the one investigated here.

From our results, we then selected the guest elements that were within 110 meV/atom from the convex hull for further studies. This included Li, Na, K, Rb, Cs, Ca, Sr, Ba, Hg, In, Tl, He, and Ne. For all these systems we performed calculations of simultaneous co-doping of the $6c$ and the $6d + 2a$ Wyckoff positions. In total, more than 1300 different compositions were investigated.

In Figs. 4.4, 4.5 and 4.6 we present a summary of our results, including all relevant phases that are close to stability. Our results are in excellent agreement with experiments, as all experimentally realized phases are green-colored in the figures. We can see that, to some extent, the simple ZK-rule emerges from the figure: when an alkali is at the center of the cages, we find the maximum of stability for co-doping with elements close to the IIIA group of the periodic table, while for Sr and Ba, the maximum stability is around the IIB group. What the ZK-rule can not explain, however, is the large number of stable

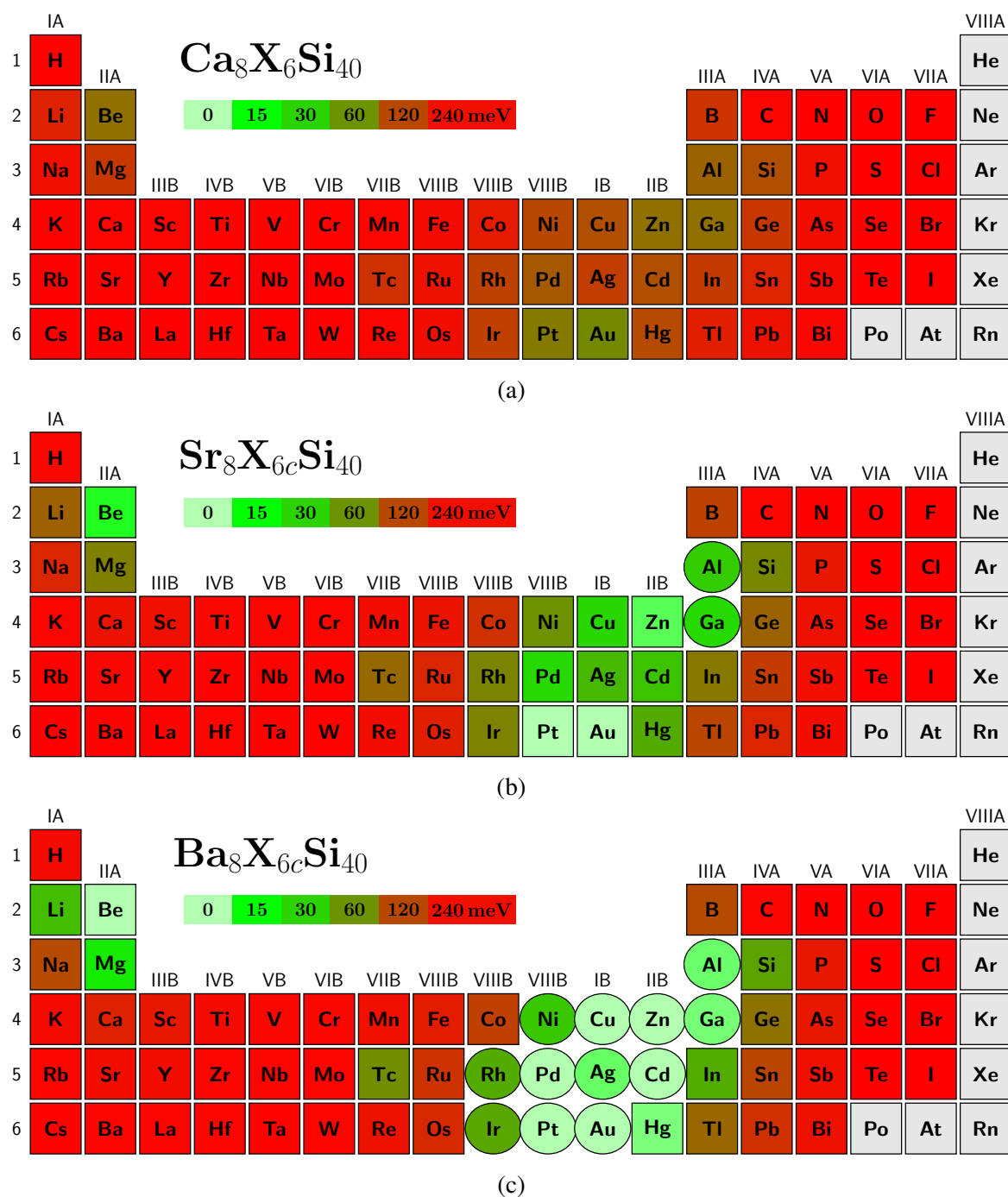
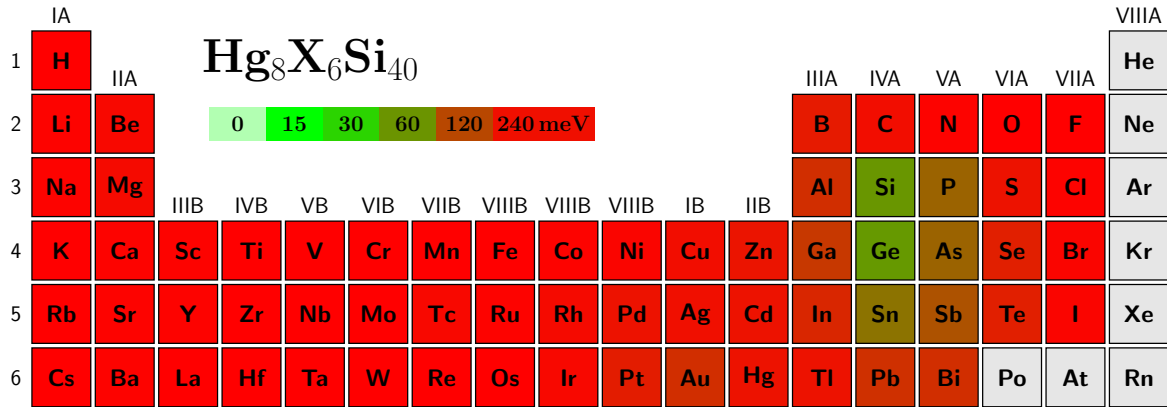
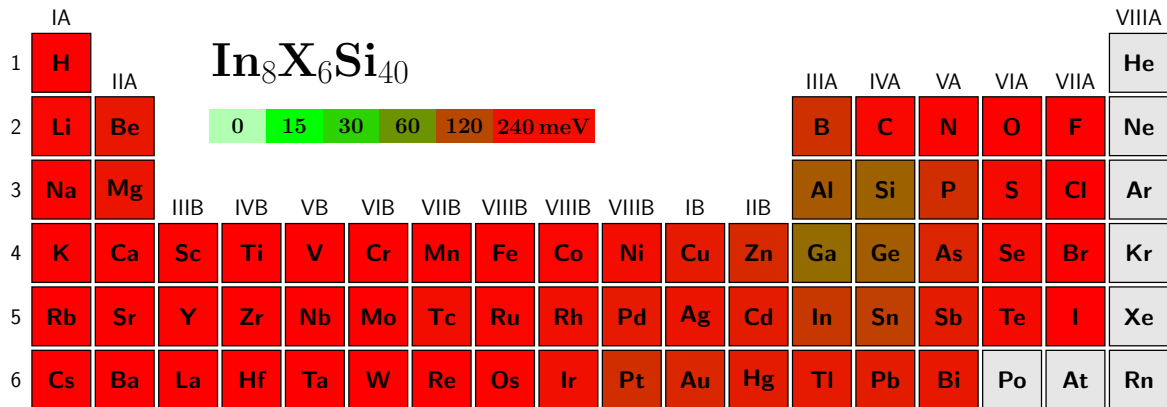


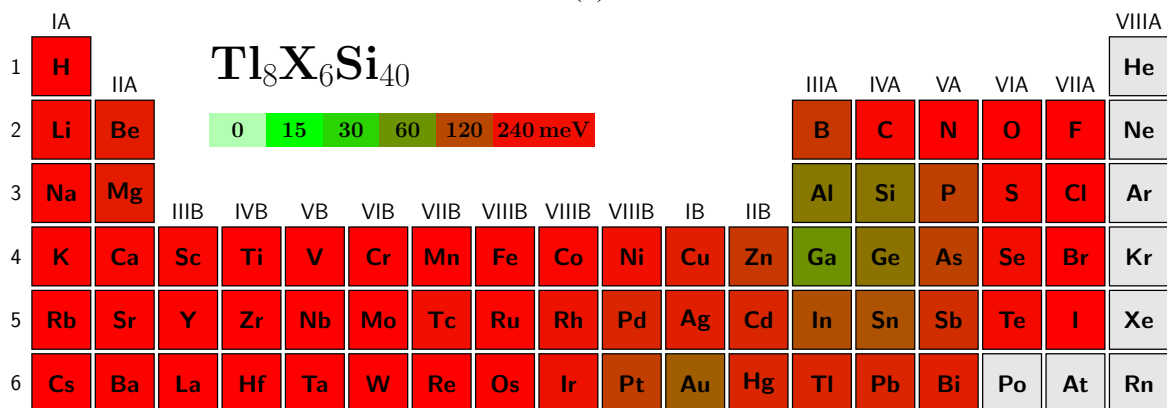
Figure 4.6 Distance to the convex hull (in meV per atom) for the clathrate $Z_{6d+2a}X_{6c}\text{Si}_{40}$ where Z is (a) Ca, (b) Sr, and (c) Ba. The circles denote phases with similar stoichiometries that were synthesized experimentally: $\text{Sr}_8\text{X}_{6c}\text{Si}_{40}$ (X=Al, Ga) [153, 154] and $\text{Ba}_8\text{X}_{6c}\text{Si}_{40}$ (X=Al, Ga, Ni, Cu, Zn, Rh, Pd, Ag, Cd, Ir, Pt, Au) [155–165]



(a)

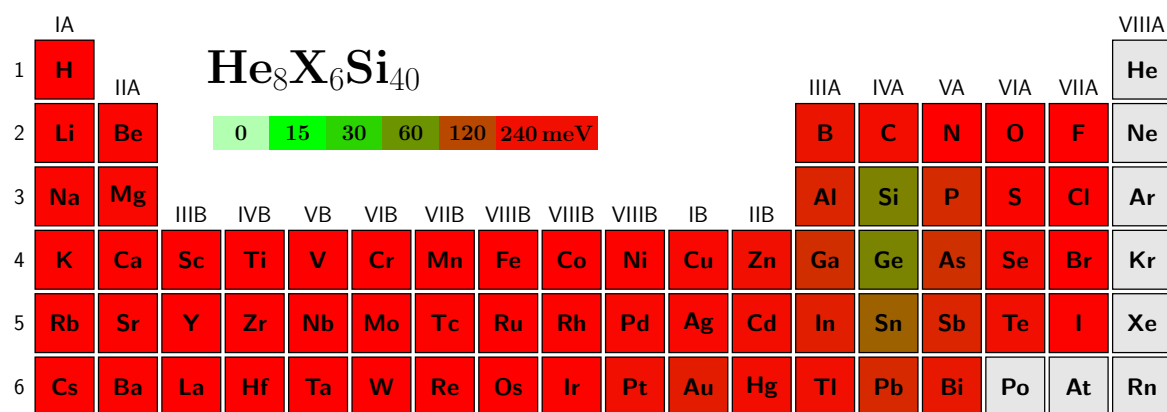


(b)

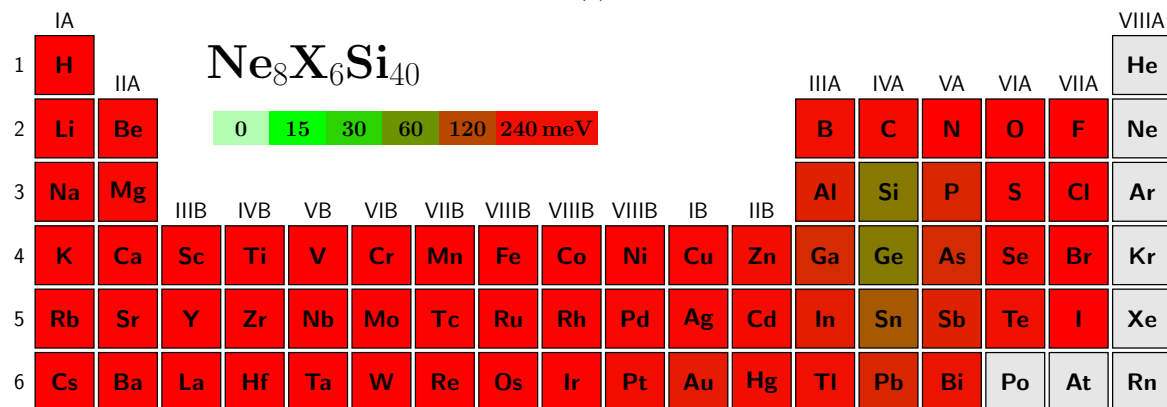


(c)

Figure 4.7 Distance to the convex hull (in meV per atom) for the clathrate $\text{Z}_{6d+2a}\text{X}_6\text{cSi}_{40}$ where Z is (a) Hg, (b) In and (c) Tl.



(a)



(b)

Figure 4.8 Distance to the convex hull (in meV per atom) for the clathrate $Z_{6d+2a}X_{6c}Si_{40}$ where Z is (a) He, and (b) Ne.

Table 4.1 Bader charges in units of $|e|$ for $\text{Ba}_8\text{Al}_6\text{Si}_{40}$, $\text{Ba}_8\text{Zn}_6\text{Si}_{40}$, and $\text{Ba}_8\text{Be}_6\text{Si}_{40}$

Wyckoff	$\text{Ba}_8\text{Al}_6\text{Si}_{40}$	$\text{Ba}_8\text{Zn}_6\text{Si}_{40}$	$\text{Ba}_8\text{Be}_6\text{Si}_{40}$
Ba (2a)	1.216	1.190	1.199
Ba (6d)	1.263	1.326	1.304
X (6c)	1.545	0.019	1.256
Si (16i)	-0.167	-0.171	-0.134
Si (16i)	-0.229	-0.227	-0.193
Si (24k)	-0.610	-0.240	-0.689
Si (24k)	-0.733	-0.365	-0.573

compounds with co-dopants from groups IB and VIII B. Moreover, compounds with Be (such as $\text{Sr}_8\text{Be}_6\text{Si}_{40}$ and $\text{Ba}_8\text{Be}_6\text{Si}_{40}$) are completely unexpected, as Be could give further electrons to the clathrate framework.

To assess the quality of our predictions, our experimental co-workers at the University of Lyon tried and successfully synthesized a new clathrate in the Ba–Be–Si ternary system, the most surprising stable composition stemming from our search. The new compound, $\text{Ba}_8\text{Be}_{3.7}\text{Si}_{42.3}$, has a unit cell parameter of 10.216 Å, which is considerably lower than the value for the parent material, recently measured in a single crystal of $\text{Ba}_8\text{Si}_{46}$ and found to be $a = 10.328$ Å [132]. The reduced cell parameter is perfectly in agreement with our simulation which predicts a value of $a = 10.297$ Å for the high-symmetry configuration $\text{Ba}_8\text{Be}_6\text{Si}_{40}$ instead of 10.392 Å for $\text{Ba}_8\text{Si}_{46}$. This new clathrate phase turns out to be a superconductor with a critical temperature of 4 K, a value lower than in the undoped material ($T_c \sim 8$ K for $\text{Ba}_8\text{Si}_{46}$).

In Fig. 4.9, we plot the density of states of $\text{Ba}_8\text{Al}_6\text{Si}_{40}$ compared to $\text{Ba}_8\text{Zn}_6\text{Si}_{40}$ and $\text{Ba}_8\text{Be}_6\text{Si}_{40}$. All three materials turn out to be remarkably similar, which is compatible to the interpretation that Be, Al, and Zn main role is to compensate the charge of the endohedral atom. The Fermi energy of the Be and Zn compounds are in a similar position, while for Al it is further displaced into the valence band due to the extra electron of Al with respect to Be and Zn. Bader charges are shown in Table 4.1. Again, the situation for the three dopants, Al, Zn, and Be is very similar, which shows that Be just assumes the role that the noble metal or semimetal would have according to the usual Zintl-Klemm rule.

Even if these results are consistent, it is important to underly that our theoretical predictions involve several approximations: (i) First there is the Perdew-Burke-Ernzerhof approximation to the exchange-correlation potential, which can give errors for formation energies as large as 0.1–0.2 eV/atom. We believe that our error is considerably smaller than this range, as our ternary clathrates usually decompose to binary silicides that have

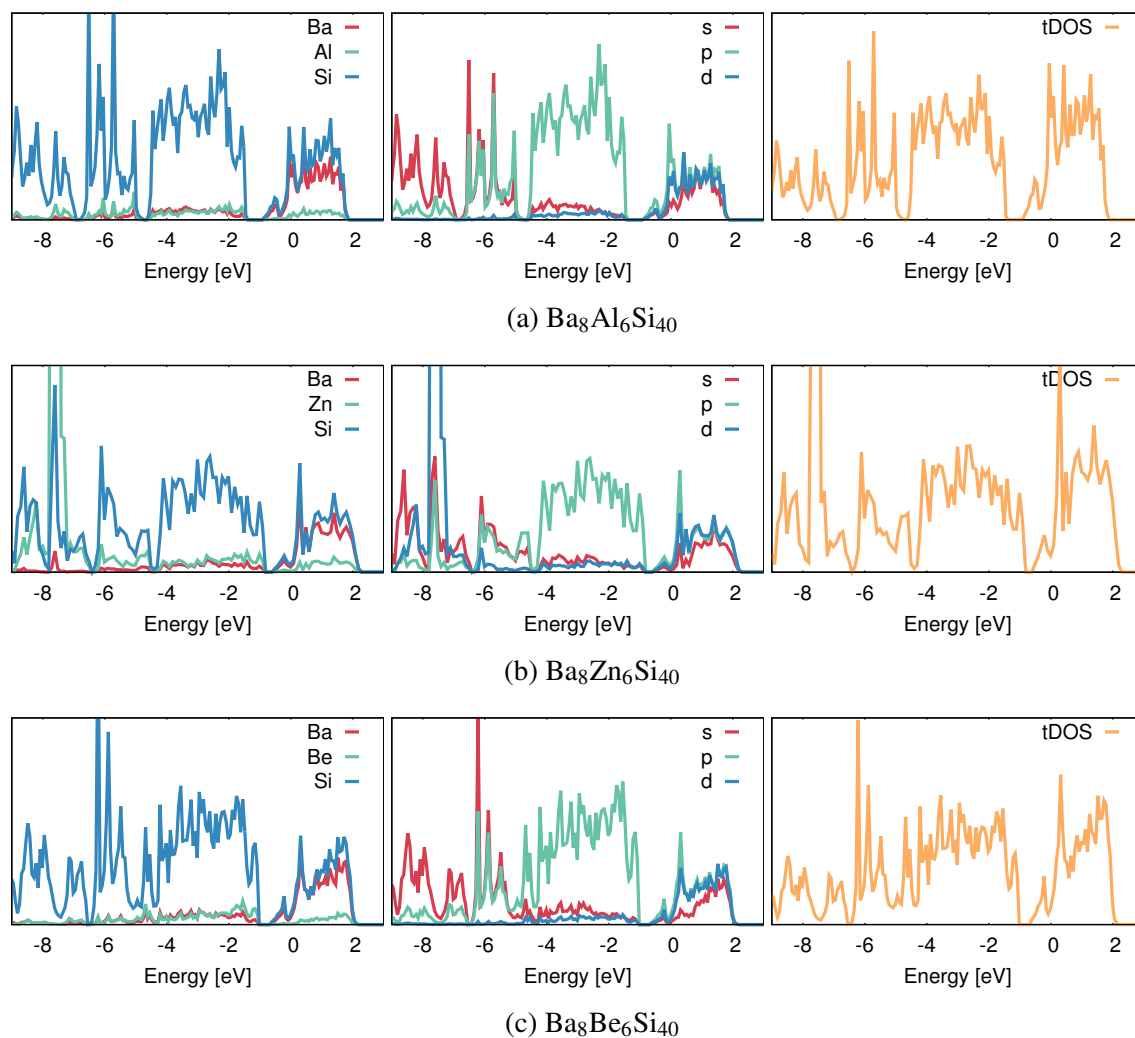


Figure 4.9 Density of states in states/eV of $\text{Ba}_8\text{Al}_6\text{Si}_{40}$, $\text{Ba}_8\text{Zn}_6\text{Si}_{40}$, and $\text{Ba}_8\text{Be}_6\text{Si}_{40}$ separated by atomic species (left), by angular momentum channel (center), and total (right). The Fermi energy is at zero.

a chemical arrangement similar to the clathrates. This should lead to systematic errors in the calculation of total energies, that mostly cancel when evaluating the distance to the convex hull. (ii) Pseudopotentials are another source of unavoidable systematic errors in our methodology, but again most of this error should cancel when calculating energy differences. (iii) All calculations were performed at zero temperature, and they did not include the correction coming from the zero-point energy. This is however expected to lead to only small corrections for the systems studied here. (iv) More importantly, we did not take into account disorder, and we always substituted all equivalent atoms of the original clathrate structure (i.e., for example we substituted all 6c atoms of Si by another element, and we did not try all other possibilities with 1, 2, 3, 4, 5, etc. dopant atoms). Of course, this reduces dramatically the number of possible systems to study, at the price of getting only an *upper bound* for the distance to the convex hull.

With all this in mind, we believe that all systems that are within ≈ 50 meV from the convex hull (the green cases in our periodic tables) have a high probability of existing. In fact, several of these green cases have already been reported experimentally. However, there are many more that have not been produced experimentally yet. Our results therefore indicate that there is a large number of Si-clathrate phases still to be synthesized. If one limits the distance to the convex hull to be lower than 30 meV per atom, 20 new phases in the clathrate of type I could likely be produced experimentally : $\text{Na}_8\text{X}_{6c}\text{Si}_{40}$ (X=Ga, Pt), $\text{K}_8\text{X}_{6c}\text{Si}_{40}$ (X=Al, Zn, In, Pt, Au), $\text{Rb}_8\text{X}_{6c}\text{Si}_{40}$ (X=Zn, In, Au), $\text{Cs}_8\text{X}_{6c}\text{Si}_{40}$ (X=Al, Ga, In, Zn), $\text{Sr}_8\text{X}_{6c}\text{Si}_{40}$ (X=Pt, Au, Zn, Cu, Pd). Moreover, all the phases with a distance to the convex hull ranging from 30 meV to 60 meV might be synthesized by means of non-equilibrium synthesis process (high pressure, thin films). Our theoretical results therefore provide a starting point for further experimental studies, establishing a novel methodology of a theoretically assisted, accelerated materials discovery, as proved here in the case of the Ba–Be–Si clathrate.

4.3 Summary and Conclusions

Using high-throughput computational techniques we investigated the stability of ternary clathrate phases based on a Si framework. We started by doping the cages of the pure-silicon clathrate, from where we selected the most promising cases (within 110 meV/atom from the convex hull): Li, Na, K, Rb, Cs, Ca, Sr, Ba, Hg, In, Tl, He, and Ne. We then tried to further stabilize these clathrates by replacing the atoms at the 6c position on the silicon framework by other elements. With the exception of He and Ne, that seem to be only providing mechanical stability to the undoped clathrates, we were able to further stabilize a variety of clathrate phases. Our results explain the vast majority of experimental results

and predict the existence of a wealth of new thermodynamically stable clathrate phases. Based on this prediction, a new Be-doped clathrate, namely $\text{Ba}_8\text{Be}_{3.7}\text{Si}_{42.3}$, was successfully synthesized. We note that this clathrate phase would probably be missed experimentally since it can not be expected based on the simple Zintl-Klemm-rule. Likewise, as we are not bounded by the price, availability, toxicity, *etc*, of the elements, we were able to predict unusual doping combinations that are traditionally not viable in the laboratory. This shows the efficiency of our approach, and indicates that experiment coupled to high-throughput computational approaches is the most cost-effective approach at our disposal for accelerated material discovery.

Chapter 5

New *p*-type transparent conducting oxides by global structure prediction

Transparent conductive oxides possess the uncommon property of being at the same time transparent to the visible spectrum and good electric conductors. The design of better-performing hole-doped transparent conductive oxides is of essential importance for technological advances in many domains, ranging from transparent electronics to thin-film solar cells. In this context, theoretical materials design based on density functional theory can play a key role by allowing us to explore in an efficient and reliable way the periodic table to test the potential of still unknown materials. Most theoretical studies follow a very simple recipe, namely the prototype search discussed in Section 2.4. A recent example of this approach is the work of Carrete and coworkers [11], who computed all possible compositions of half-Heusler compounds in the cubic structure (around 80,000 possibilities) and the work by Hautier and coworkers [166] who investigated Nature's missing oxides, i.e., which oxides were thermodynamically stable, but still unknown to mankind. It is evident that the major drawback of this approach is the impossibility to discover any material with different crystal structure than those of the compounds already contained in available databases.

Here, we address this problem and go a step further, by discussing an example of combination of global crystal structure prediction, that is usually applied in literature to study one or few related chemical compositions, with high-throughput methods to explore the periodic table of chemical elements. Our aim is to identify the lowest-energy crystal structures of materials with unreported chemical compositions, and verify if these lowest-energy structures are thermodynamically stable. In possession of these structures, we can then evaluate a number of spectroscopic properties using standard methods based on density functional theory and beyond.

In this case, we are interested in a subset of oxides, namely those having a composition of the type $(\text{Cu,Ag,Au,Ni})\text{XO}_2$, which includes the “famous” delafossites $\text{Cu}(\text{Al,In,Ga})\text{O}_2$ [167–170]. The compounds of this family are still the most promising *p*-type transparent conducting oxides (TCO) known to mankind. Additionally, promising *p*-type character was also identified in oxysulfides and oxyselenides [171–174]. Therefore, we will also study one of these systems, namely the CuXOS family. TCOs are indispensable for many high-technology devices which require transparent contacts, such as flat panel displays, touch screens, thin-film and stacked solar cells, functional windows, etc. Good electron (*n*-)doped TCOs, namely those based on SnO_2 , In_2O_3 , and ZnO , are already widely used in commercial applications. However, potential *p*-type TCOs identified up to date have conductivities at least one or two orders of magnitude lower than their *n*-type counterparts and carrier mobilities too small for large-scale exploitation. The best *p*-type TCO until now is $\text{CuCr}_{(1-x)}\text{Mg}_x\text{O}_2$ [175], which displays a conductivity of $220 \text{ } \Omega^{-1}\text{cm}^{-1}$ and a hole mobility of about $1 \text{ cm}^2/\text{Vs}$, while also suffering from poor transparency, with transmission in the visible smaller than 30%.

The origin of the relatively higher hole mobility of Cu delafossites relies on the fact that the highest valence bands are obtained through the strong hybridization of almost-degenerate oxygen *2p* and copper *3d* states. This hybridization reduces the localization of the top valence states on oxygen atoms, leading to more dispersive *p-d* anti-bonding bands with smaller hole effective masses [176]. A tetrahedral coordination of oxide ions (as in delafossite crystals) is particularly advantageous as it allows strong hybridization. Cu^{1+} (or equivalently Ag^{1+} and Au^{1+}) appear ideal elements for creating a *p-d* dispersive top valence while preserving transparency, as their closed *d* shell will prevent from absorbing light in the visible. Even if it is believed that a Cu^{+1} configuration is the best to obtain TCOs, we decided nevertheless to explore blindly also compositions that favor Cu^{2+} or even Cu^{3+} , as we do not want to preclude the possible formation of crystalline structures different from delafossite that would let emerge interesting electronic properties in different environments.

We can extract from the analysis above some expected good rules for the design of improved *p*-type TCOs: (i) cations should have *d* shells proximate in energy to oxygen *2p* states; (ii) cation *d* shells should be closed to avoid optical absorption in the visible range; (iii) strong hybridization of oxygen *p* and cation *d* states is required to increase the band dispersion [176]. Following these simple ideas, few other Cu oxides were already successfully tested in experiments after $\text{Cu}(\text{Al,In,Ga})\text{O}_2$ [167–170], such as CuCrMgO_2 [177], SrCu_2O_2 [178] or LaCuOS [171] and $(\text{Cu,Ag})\text{ScO}_2$ [175]. Our aim is now to extend and make more systematic this investigation by pre-screening *in silico* possible Cu, Ag, Au and Ni based ternary oxides, in order to offer to experimentalists a reliable guide on the stability and electronic properties of the still unknown compositions. Note that the set under consideration

here is also a subset of the systems studied using high-throughput and data-mining techniques in the above-mentioned work of Hautier and coworkers [166]. As a consequence, we will be able to provide a direct comparison of the success rate of our mixed approach, that combines high-throughput with structural prediction, in comparison with a high-throughput study based on prototype crystal structures. For reference, we should keep in mind that four materials of the type $(\text{Cu,Ag,Au,Ni})\text{XO}_2$ unreported in experimental databases were obtained in Ref. 166, namely (i) a trigonal phase of AgCoO_2 (50 meV above the convex hull of thermodynamic stability) based on the prototype experimental structure of AgInO_2 , (ii) a tetragonal phase of AgCsO_2 based on the prototype CuCsO_2 , (iii) an hexagonal phase of AgLaO_2 based on the prototype AgAlO_2 (4 meV above the hull), and (iv) an hexagonal phase of NiPtO_2 based on the prototype AgNiO_2 (1 meV above the hull).

5.1 Details of Calculations

We performed minima hopping simulations for all stoichiometries of the type $(\text{Cu, Ag, Au, Ni})\text{XO}_2$ and CuXOS , where X is any element of the periodic table up to Bi with the exclusion of the rare gases and the lanthanides. Forces and energies were calculated at zero temperature within density functional theory [27, 28] in the projector augmented wave (PAW) formalism [179] as implemented in VASP [39, 40]. For a given stoichiometry, the initial geometries were obtained randomly, ensuring only that the minimal distance between the atoms was at least equal to the sum of the covalent radii. The MHM searches were performed using the Perdew-Burke-Erzerhof (PBE) [141] approximation to the exchange-correlation functional. We used default “high” accuracy energy cutoffs. Each minima hopping run was repeated at least twice, using both one and two formula units (4 or 8 atoms). This may seem a relatively small number of atoms in the unit cell, but if we look at the experimentally known structures of the this family, we realize that almost all of them have a ground-state with less than 8 atoms (exceptions are some metastable phases of AgCO_2 with 16 atoms per unit cell and a stable phase of AgBO_2 with 128 atoms per unit cell). Therefore, we assume that this is not a major limitation. The CPU time required to perform structural prediction is about 3500 hours per composition.

We then compared the structures obtained in our runs with the ones present in available experimental and theoretical databases [4, 5]. Almost all experimental structures appeared at the early stages of our minima hopping runs, which certainly proves the efficiency of the method for this kind of task. Finally, we took the experimental structures and other relevant theoretical phases that we discovered during our minima hopping runs, and used them as prototypes for modified stoichiometries. We believe that this procedure, which effectively

mixes high-throughput techniques with structural prediction is essential in such large scale applications as each method can be used to provide a check on the other.

In total we investigated 304 stoichiometries, and we obtained $\sim 30,000$ minima, of which $\sim 10,000$ were further analyzed. In this last step we followed the same protocol as in the Materials Project database: spin-polarized calculation using the PBE [141] exchange-correlation functional, with the exception of the oxides of Co, Cr, Fe, Mn, Mo, Ni, V, W where an on-site Coulomb repulsive interaction U [180] with a value of 3.32, 3.7, 5.3, 3.9, 4.38, 6.2, 3.25, and 6.2 eV, respectively, was added to correct the *d*-states. Note that spin-polarized calculations are essential for this class of materials. We are of course aware that the PBE (+ U) functional is not always able to determine the correct electronic and spin ground state. Nevertheless, the optimized crystal structure is very often qualitatively and quantitatively good within PBE, even in many cases in which the electronic states are not correctly described. As an example, we can use the well studied case of Cu-O binaries [181]. Calculations using PBE give crystal structures in excellent agreement with experiments for Cu_4O_3 and Cu_2O , and a reasonable crystal structure for CuO , even if the error on the lattice constants and angles is larger than usual. On the other hand, electronic states are poorly described in PBE: Cu_4O_3 and CuO are metals, and the band gap of Cu_2O is strongly underestimated. Hybrid functionals can improve on both electronic and structural properties. However, this improvement comes at the price of a much higher computational cost, which makes them unsuitable for high-throughput calculations.

PAW setups were taken from the version 5.2 of VASP. At this stage the energy cutoff was set to 520 eV (irrespective of the elements considered) and k-point grids were automatically chosen to ensure convergence to better than 2 meV per atom. For all low-lying minima we studied the thermodynamic phase equilibria of the ternary system, considering the energy balance with respect to all possible decompositions in ternary, binary and elementary compounds that respect the overall stoichiometry: i.e, we measured the thermodynamic stability by calculating the energy distance from the convex hull of stability, which is the set of lines that connects the lowest energy ordered phases. This step was performed using PYMATGEN [182] and considering all ternary, binary and elementary phases included in the Materials Project database. According to this definition, a compound is stable if its total energy distance to the convex hull is zero. Finally, the crystallographic analysis of the structures was performed using FINDSYM [183].

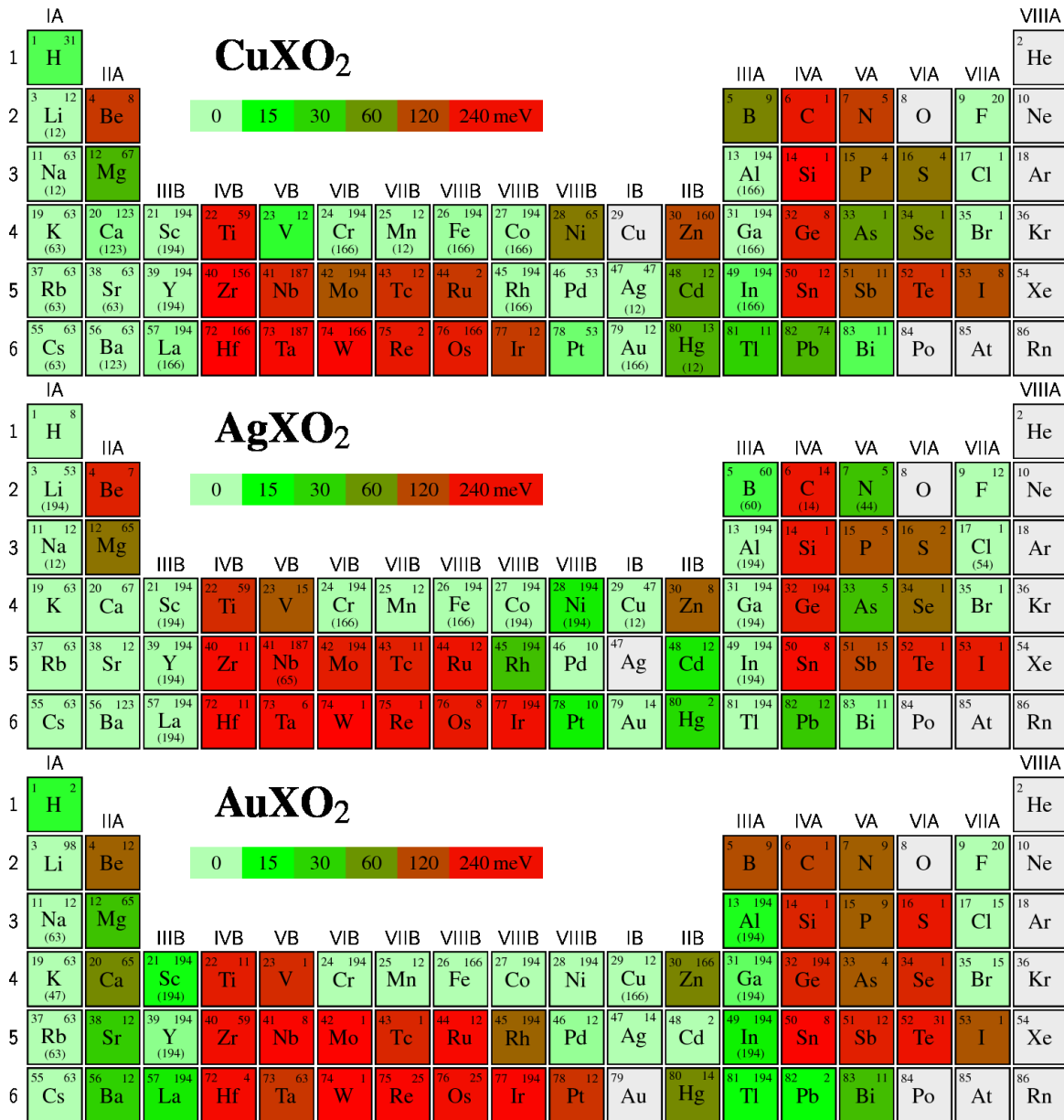


Figure 5.1 Distance to the convex hull (in meV per atom) for CuXO_2 , AgXO_2 , and AuXO_2 . The colors indicate the distance to the convex hull of stability, light green meaning that the composition is thermodynamically stable. For each element we show the symbol (center), atomic number (top left), space group of the lowest energy structure (top right), and the space groups of the phases found in experimental databases (bottom, in parenthesis).

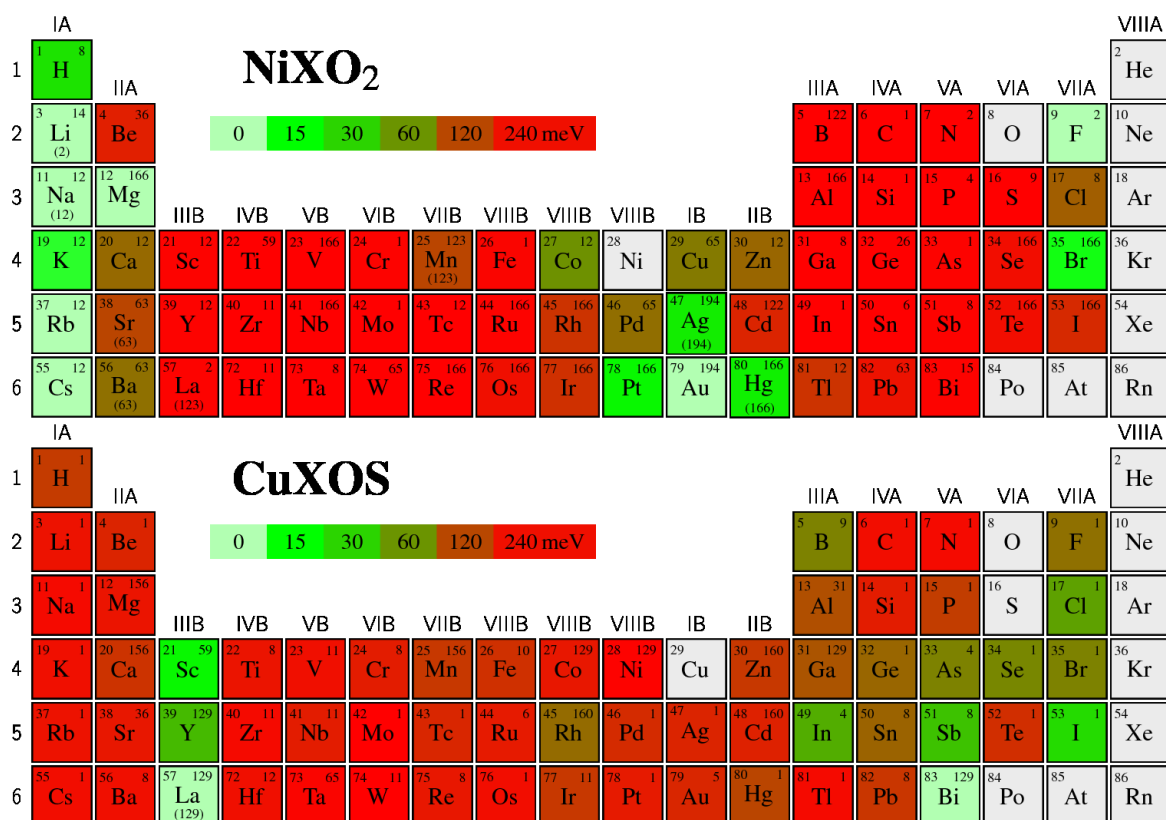


Figure 5.2 Distance to the convex hull (in meV per atom) for NiXO₂ and CuXOS. The colors indicate the distance to the convex hull of stability, light green meaning that the composition is thermodynamically stable. For each element we show the symbol (center), atomic number (top left), space group of the lowest energy structure (top right), and the space groups of the phases found in experimental databases (bottom, in parenthesis).

5.2 Results and Analysis

Our results are summarized in Fig. 5.1 and 5.2. In these periodic tables the color scale indicates the distance of the calculated energy of the ground-state structure to the convex hull of stability. Light green cases indicate stable structures (i.e., that correspond to a crystal structure on the hull). We further indicate the atomic number (upper left), the space group we predict for the lowest energy phase (upper right), and the space groups of the lowest-energy experimental structure that we found in available databases (in parenthesis below the chemical symbol). This means that all squares without a number below the chemical symbol represent crystal structures predicted theoretically.

As we can see from Figs. 5.1 and 5.2, many compositions are thermodynamically stable, and many others are quite close to the convex hull. Note that our calculations are performed at zero temperature and pressure for perfect periodic crystals. However it is well known that unstable phases can be stabilized by temperature, pressure, defects, dopants, etc. Moreover, due to the theoretical error associated to the calculation of the total energy, an inversion of the ordering of the phases very close in energy is always possible. In view of the above, we believe it is relevant to discuss all compositions that are either thermodynamically stable or quasi-stable (within 20 meV from the convex hull). This choice of 20 meV as a threshold of stability comes from the observation that well studied experimental compounds such as CuInO_2 and AgNiO_2 are above the hull by 10-20 meV in our calculations performed for perfect stoichiometric bulk crystals. The set of structures that we select within this threshold contains therefore phases that have a large chance of being synthesized experimentally. We find that this stability condition is fulfilled by 93 compositions (30 containing Cu, 29 containing Ag, 25 containing Au, 11 containing Ni and 3 containing CuXOS), of which only 41 (19 containing Cu, 11 containing Ag, 8 containing Au, 4 containing Ni and 1 CuXOS) are present in experimental databases.

We are now in the position to compare our predictions with the previous theoretical work of Ref. 166 and few theoretical structures contained in the Materials Project database. There are four phases (AgCoO_2 , AgLaO_2 , AgCsO_2 and NiPtO_2) that were previously predicted in Ref. 166, while theoretical crystal structures for CuBaO_2 , CuAuO_2 , CuHgO_2 , AgLiO_2 , AgNaO_2 , NiHgO_2 and NiLiO_2 can be found in the Materials Project database. Three cases do occur. We find the same structure for AgLaO_2 , AgNaO_2 , AgCsO_2 , NiPtO_2 , and $(\text{Cu,Ni})\text{HgO}_2$, a slightly distorted structure for CuAuO_2 and NiLiO_2 , and very different structures for CuBaO_2 and AgLiO_2 . In the last two cases, our structures are lower in energy by 73 meV/atom and 167 meV/atom, respectively. We should also observe that there might exist even lower energy structures that were not detected in the MHM runs (because their unit cell contains more than 8 atoms, for example). However, the compounds we predict

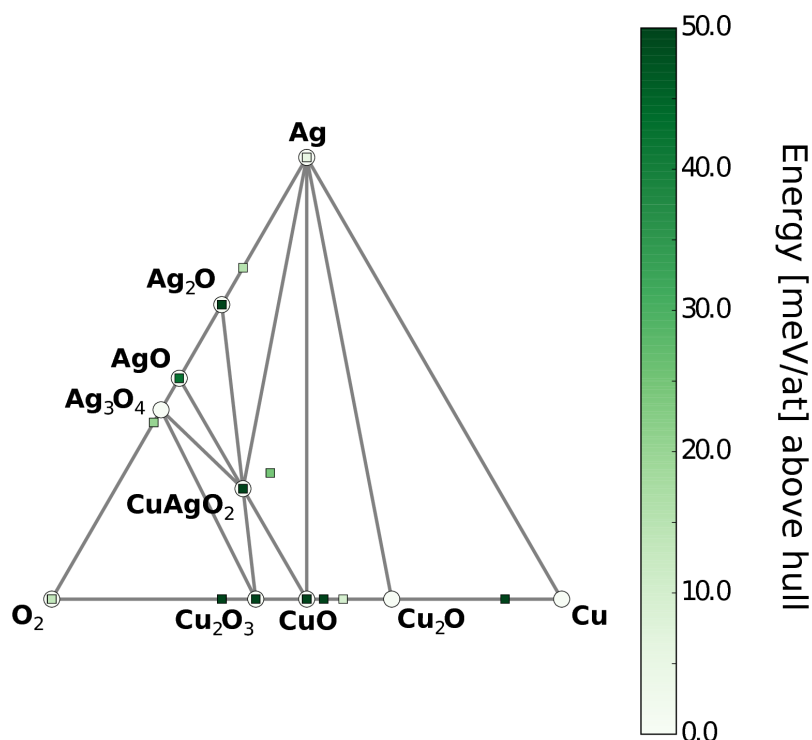


Figure 5.3 Ternary phase diagram of CuAgO_2 generated using PYPATGEN [182]. White circles: stable structures, squares: unstable structures. The color of the squares indicates the distance to the convex hull according to the color legend shown on the right of the diagram.

to be thermodynamically stable have a high chance of being experimentally synthesizable, even if the actual atomic arrangement may eventually differ from the one that we have determined. In this sense, the periodic tables shown in Fig. 5.1 and 5.2 offer a simple guide to experimentalists by indicating which compositions are expected to be easy and which are expected to be hard to synthesize, based on thermodynamic considerations.

As an example we discuss here the ternary phase diagram of CuAgO_2 . We considered only ordered crystalline phases. In Fig. 5.3 we indicate stable structures with white circles, while squares correspond to unstable compositions. A square inside a circle indicates two structures close in energy. The color of the squares (changing gradually from white to dark green) represent the distance to the convex hull in the range from 0 (white) to 50 meV (dark green). On the sides of the triangle we find the possible binary phases. Our lowest energy phase of CuAgO_2 is indicated by the circle inside the triangle. It is a layered orthorhombic structure (space group 47). Another low-energy structure of CuAgO_2 is indicated by a light green square (20 meV per atom above the hull). This is the experimental monoclinic phase with space group 12, which can be seen as a distorted delafossite structure.

Before entering in a detailed discussion on the electronic properties of the new stable phases found in our simulations, a few general remarks are in order. (i) There are some basic atomic arrangements that are energetically favorable (with some exceptions) for many compounds of this family. The most common ones are the delafossite structure of, e.g., CuFeO_2 (space groups 166 and 194) and the tetragonal structure of CuCaO_2 (space group 123), together with some slightly distorted, and therefore less symmetric, variants. We stress, however, that some recurrent crystal structures that we identified do not have any representative compound in databases. (ii) A majority of the structures are layered, but there is a substantial variety in the geometry of the layers. We could not find a strong correlation between layered structures and size mismatch of the two cations, at variance with the study on the smaller family of LiMO_2 ($M = \text{Sc-Cu}$) ternaries in Ref. [184] (iii) We observe a mixture of semiconducting and metallic structures, and for some compositions we can even find semiconducting and metallic phases separated by only a few meV/atom. It is important to observe that our calculations of total energies have an accuracy of few meV/atom, therefore we cannot discriminate between metastable crystal structures that are very close in energy, and for which different energetic ordering can be obtained using different exchange-correlation functionals. This is in particular true for compounds containing transition metal oxides, where magnetic ordering may be misrepresented.

Having the crystal structures of new stable and metastable compounds opens the way for a series of further theoretical studies. In fact, we can now calculate a wealth of physical properties using the numerous methods and codes available for theoretical spectroscopy. Our main motivation for the choice of this class of systems is the p -type conductivity measured in Cu delafossites. Therefore, we obtained the average hole effective mass and the electronic band-gap for the ground-state of all the stoichiometries studied. All calculations were performed with using PYMATGEN [182] and BOLTZTRAP [185] software packages. Following the same approach as Ref. 14 we calculated the averaged hole effective mass tensor for a carrier concentration of 10^{18} cm^{-3} and a temperature of 300 K. We then used the higher limit estimation for m_h^* (see Supporting Information of Ref. 14). The results are summarized in Fig. 5.4. In the figure, the color of the points indicates thermodynamical stability, respecting the same color scale as in Fig. 5.1. We observe that the numbers we indicate for the energy gap should be taken with care as they are Kohn-Sham gaps obtained with the PBE(+U) exchange-correlation functional, and are systematically underestimated [186, 187]. The true gaps are substantially larger (usually at least twice as large) than the ones we indicate. Moreover, systems that are metallic within PBE(+U) can sometimes be semiconducting in experiment, however the inverse never happens. Note that band dispersions, and therefore

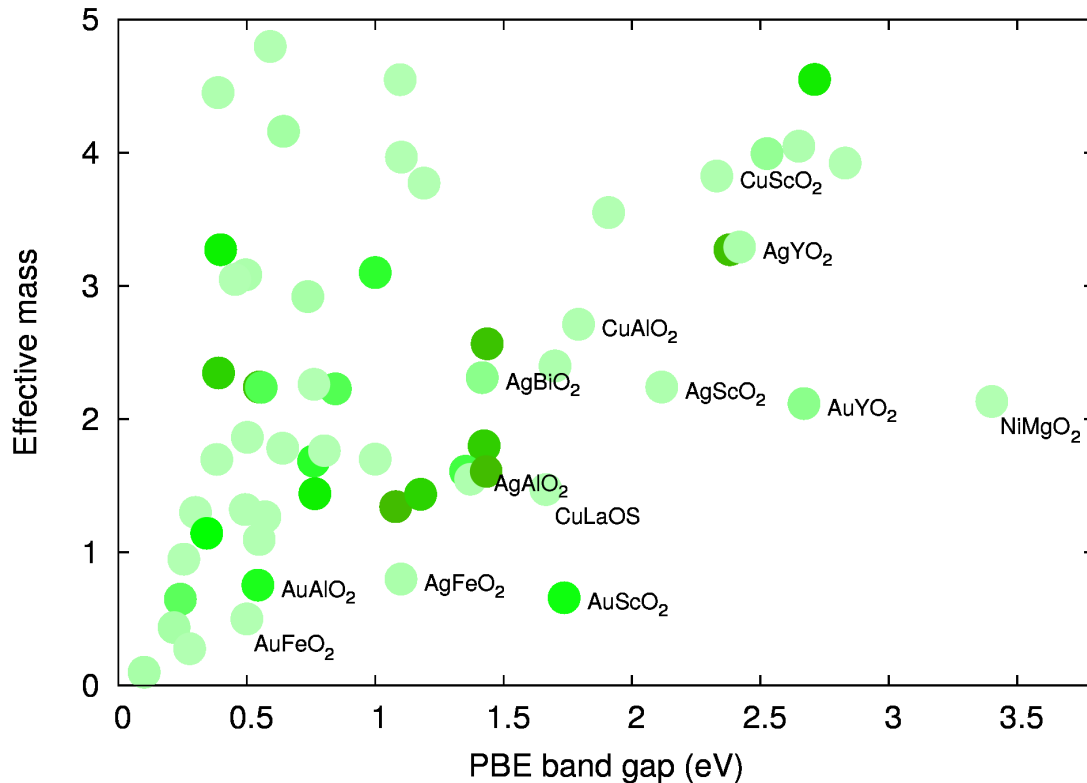


Figure 5.4 Effective hole masses as a function of the PBE(+U) band gap for all compounds that are within 50 meV/atom from the convex hull. The color of the dots gives the distance to the hull and follows the same scale as in Fig. 5.1.

effective masses, are generally less sensitive to the choice of the approximation used for the calculation of band structures.

For *p*-type transparent conductive materials we desire low-hole effective masses (to improve conductivity), and high energy gaps (to ensure transparency). Approximately in the center of Fig. 5.4 we find CuAlO₂, the compound where *p*-type electrical conductivity in transparent thin-films was discovered for the first time [167]. Its gap is sufficiently large (note that the PBE gap of 1.8 eV is substantially lower than the experimental gap of around 3.5 eV; see, e.g., Refs.186, 187 and references therein), but the hole effective mass is relatively high. Indeed, the *p*-type conductivity in CuAlO₂ is still too low for technological applications. From Fig. 5.4 we can see that several materials have the potential to outperform CuAlO₂, such as AgScO₂, AuScO₂, AuYO₂, AgAlO₂, AgBiO₂, NiMgO₂, etc. Due to the presence of (expensive) noble metals (Ag and Au), it is unlikely that most of these materials can directly find large scale applications in technology, nevertheless an experimental study of conductivity in new interesting phases could give valuable ideas on if (and eventually how) hole mobilities can be increased beyond present limits. NiMgO₂ on the other hand does not

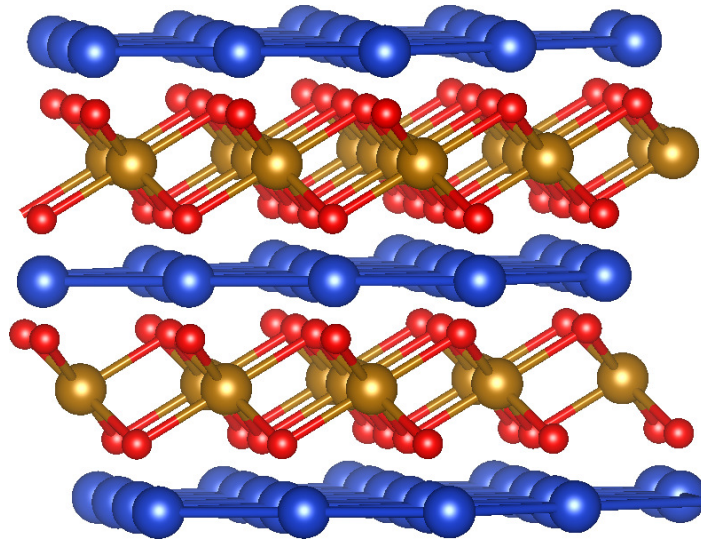


Figure 5.5 The delafossite structure (space group 166).

have expensive elements, it has a large gap, but its conductivity may still be not high enough. In Tables 5.1 and 5.2 we summarize the information concerning the energy distances from the convex hull, the band gaps and the hole effective masses. We also include in Appendix A a table with Bader charges, oxidation states, and coordination numbers for all structures within 50 meV to the convex hull of stability.

These results call for more detailed experimental studies of this restricted set of compounds, that should be accompanied by more accurate calculations of the electronic band gaps (i.e. using GW approaches beyond standard density functional theory [186, 187]) and of possible defects/impurities for p -type dopability. From a purely theoretical point of view, the results of Fig. 5.4 demonstrate that, with our approach, we are now able to go all the way from a simple stoichiometry to the estimate of relevant material properties for a vast class of materials.

We will now analyze more in detail the structural and electronic properties of the different subclasses of compounds that we identified. We will extend this discussion to phases that are closer than 50 meV to the convex hull.

5.2.1 Delafossites

The trigonal (space group 166) or hexagonal (space group 194) delafossite structures (depending on the stacking sequence) are the crystal structure assumed by all stable compounds $(\text{Cu,Ag,Au})\text{XO}_2$ with X belonging to group IIIA (Al, Ga, In), IIIB (Sc, Y, La), or $\text{X}=\text{Cr, Fe, Co, Ni, and Rh}$. Also NiBrO_2 , NiPtO_2 , AgTiO_2 and AuTiO_2 (but not CuTiO_2) present a low-energy delafossite structure. This phase is characterized by XO_2 planes separated by flat

Table 5.1 Space groups (Spg), distance to the convex hull (E_{hull}), gaps (Gap) and average hole effective mass (m_h^*) for semiconducting structures of the form $CuXO_2$ and $AgXO_2$ lying below 50 meV/atom from the convex hull.

Structure	E_{hull}	Spg	Gap	m_h^*	Structure	E_{hull}	Spg	Gap	m_h^*
CuHO ₂	8	31	0.5	2.23	AgHO ₂	0	8	0.0	–
CuLiO ₂	0	2	0.5	17.9	AgLiO ₂	0	53	0.5	1.85
CuFO ₂	0	4	0.8	11.8	AgBO ₂	33	9	1.4	1.61
CuNaO ₂	0	63	0.4	3.04	AgNO ₂	37	5	1.4	2.57
CuMgO ₂	43	67	0.0	–	AgFO ₂	0	4	0.6	7.61
CuAlO ₂	0	166	1.8	2.66	AgNaO ₂	0	12	0.6	4.79
CuClO ₂	0	1	0.8	48.9	AgAlO ₂	0	166	1.4	1.49
CuKO ₂	0	63	0.8	13.7	AgClO ₂	0	1	0.6	2902
CuCaO ₂	3	123	0.0	–	AgKO ₂	0	63	0.9	5.80
CuScO ₂	0	194	2.4	4.50	AgCaO ₂	0	12	0.0	–
CuVO ₂	11	12	1.0	3.42	AgScO ₂	0	194	2.1	2.58
CuCrO ₂	0	166	1.6	5.52	AgCrO ₂	0	166	1.7	2.48
CuMnO ₂	0	12	0.1	0.06	AgMnO ₂	0	12	0.4	1.33
CuFeO ₂	1	166	0.9	2.02	AgFeO ₂	0	166	1.1	0.90
CuCoO ₂	0	166	1.1	5.63	AgCoO ₂	0	194	1.2	3.68
CuGaO ₂	0	166	0.8	2.23	AgNiO ₂	20	166	0.0	–
CuBrO ₂	0	1	0.9	9.67	AgGaO ₂	0	166	0.6	1.09
CuRbO ₂	0	63	0.8	8.98	AgAsO ₂	38	5	2.4	3.25
CuSrO ₂	0	63	0.0	–	AgBrO ₂	0	1	0.7	450
CuYO ₂	0	194	2.6	4.01	AgRbO ₂	0	63	1.0	8.80
CuRhO ₂	0	166	0.7	2.75	AgSrO ₂	0	12	0.6	1.27
CuPdO ₂	0	53	0.0	–	AgYO ₂	0	194	2.4	3.82
CuAgO ₂	0	47	0.0	–	AgRhO ₂	38	166	0.5	2.14
CuInO ₂	7	166	0.3	0.57	AgPdO ₂	0	10	0.1	0.03
CuCsO ₂	0	63	0.9	5.24	AgCdO ₂	23	12	0.0	–
CuBaO ₂	0	63	0.0	–	AgInO ₂	0	166	0.2	0.43
CuLaO ₂	2	166	2.7	4.03	AgCsO ₂	0	63	1.1	4.54
CuYbO ₂	0	123	0.0	–	AgBaO ₂	0	123	0.0	–
CuPtO ₂	6	53	0.0	–	AgLaO ₂	0	194	2.8	3.85
CuAuO ₂	0	12	0.0	–	AgPtO ₂	19	10	0.3	3.30
CuHgO ₂	43	12	0.0	–	AgAuO ₂	0	14	0.6	1.80
CuTlO ₂	31	11	0.4	2.36	AgHgO ₂	27	2	0.0	–
CuPbO ₂	43	74	0.0	–	AgTlO ₂	0	166	0.0	–
CuBiO ₂	8	11	1.0	2.29	AgPbO ₂	34	12	0.3	0.03
					AgBiO ₂	3	11	1.4	2.38

Table 5.2 Space groups (Spg), distance to the convex hull (E_{hull}), gaps (Gap) and average hole effective mass (m_h^*) for semiconducting structures of the form $AuXO_2$, $NiXO_2$ and $CuXOS$ lying below 50 meV/atom from the convex hull.

Structure	E_{hull}	Spg	Gap	m_h^*
AuHO ₂	12	2	0.7	1.68
AuLiO ₂	0	53	1.1	3.78
AuFO ₂	0	4	1.1	3.97
AuNaO ₂	0	12	1.1	7.72
AuMgO ₂	37	65	0.0	–
AuAlO ₂	12	166	0.6	0.71
AuClO ₂	0	15	0.3	0.96
AuKO ₂	0	63	1.4	9.20
AuScO ₂	14	166	1.8	0.63
AuCrO ₂	0	166	1.2	1.65
AuMnO ₂	0	12	0.0	–
AuFeO ₂	0	166	0.6	0.59
AuCoO ₂	0	194	0.5	1.03
AuNiO ₂	0	194	0.0	–
AuGaO ₂	6	166	0.0	–
AuBrO ₂	0	15	0.0	–
AuRbO ₂	0	63	1.4	8.45
AuSrO ₂	33	12	1.3	1.80
AuYO ₂	3	194	2.7	2.49
AuPdO ₂	2	12	0.0	–
AuCdO ₂	0	2	0.9	1.76
AuInO ₂	18	166	0.0	–
AuCsO ₂	0	63	1.5	6.59
AuBaO ₂	31	12	1.2	1.44
AuLaO ₂	21	194	2.7	4.45
AuTlO ₂	13	166	0.0	–
AuPbO ₂	15	2	0.4	1.14
AuBiO ₂	40	11	1.3	1.54

Structure	E_{hull}	Spg	Gap	m_h^*
NiHO ₂	24	8	0.03	0.02
NiLiO ₂	0	14	0.4	1.70
NiFO ₂	0	2	0.0	–
NiNaO ₂	0	12	0.4	4.45
NiMgO ₂	0	166	3.4	2.13
NiKO ₂	11	12	1.0	9.42
NiBrO ₂	14	166	0.0	–
NiRbO ₂	0	12	1.9	7.08
NiCsO ₂	0	12	1.9	3.55
NiPtO ₂	17	166	0.0	–
NiHgO ₂	20	166	0.8	1.44

Structure	E_{hull}	Spg	Gap	m_h^*
CuScOS	18	59	1.4	10.4
CuYOS	40	129	1.4	1.61
CuInOS	46	4	0.0	–
CuSbOS	37	8	0.8	5.58
CuIOS	27	1	0.0	–
CuLaOS	0	129	1.7	1.47
CuBiOS	0	129	0.5	1.32

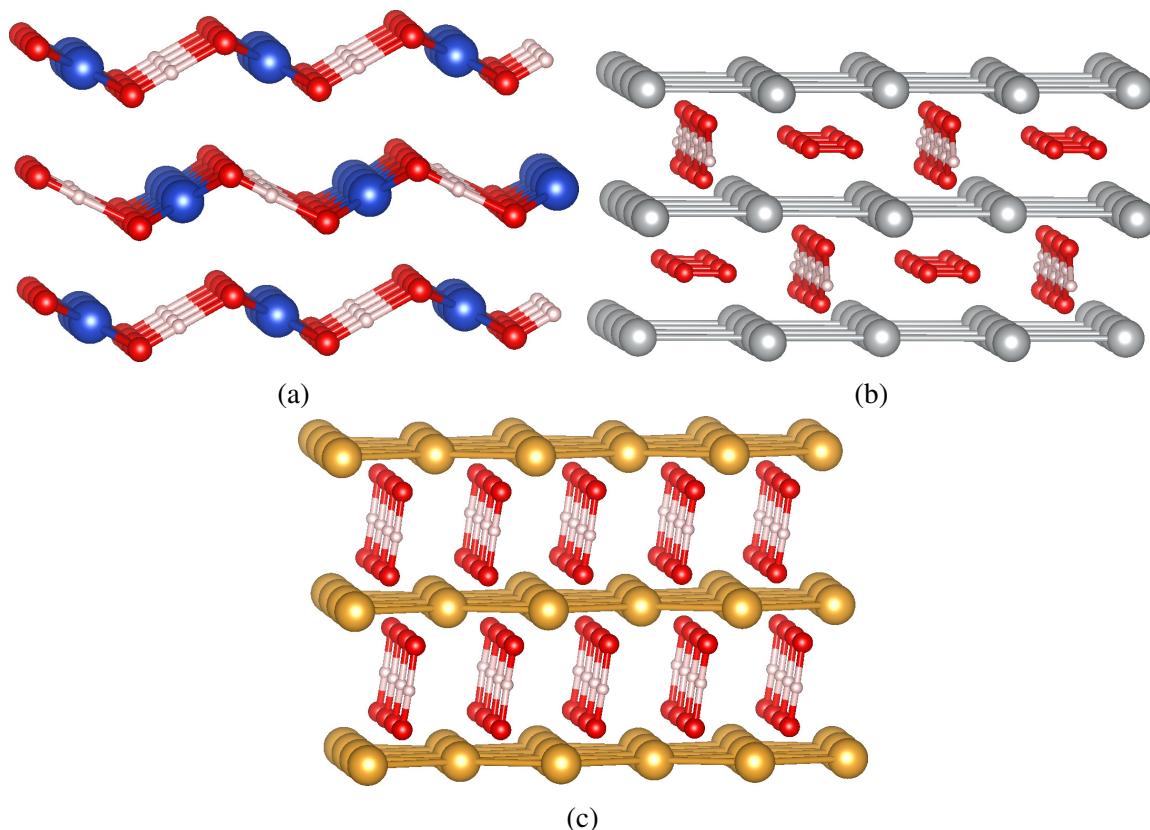


Figure 5.6 The structures of (a) CuHO_2 (space group 31), (b) AgHO_2 (space group 8), and (c) AuHO_2 (space group 2).

hexagonal (Cu,Ag,Au) planes. The energy differences between the trigonal and hexagonal phases is always very small (of the order of few meV/atom), sometimes smaller than the precision in our calculations. Thermodynamically stable delafossite structures not present in databases are AgTiO_2 , AuCrO_2 , AuFeO_2 , AuCoO_2 , AuNiO_2 , AuTiO_2 , AuLaO_2 and NiMgO_2 .

5.2.2 Group IA

Hydrogen We found a series of distinct structures for (Cu,Ag,Au,Ni) HO_2 (see Fig. 5.6). The Cu compound crystallizes in a layered structure (space group 31) composed of zigzag layers of CuHO_2 . It is just above the convex hull at 8 meV/atom, and is an indirect-gap semiconductor with a PBE gap of 0.5 eV. The Ag compound shows flat layers of Ag (in a square lattice) separated by zigzag lines of OH and O_2 dimers. This is a monoclinic (space group 8), metallic, thermodynamically stable phase. AuHO_2 is a low-symmetry structure (space group 2), composed by flat Au layers separated by aligned HO_2 units. It

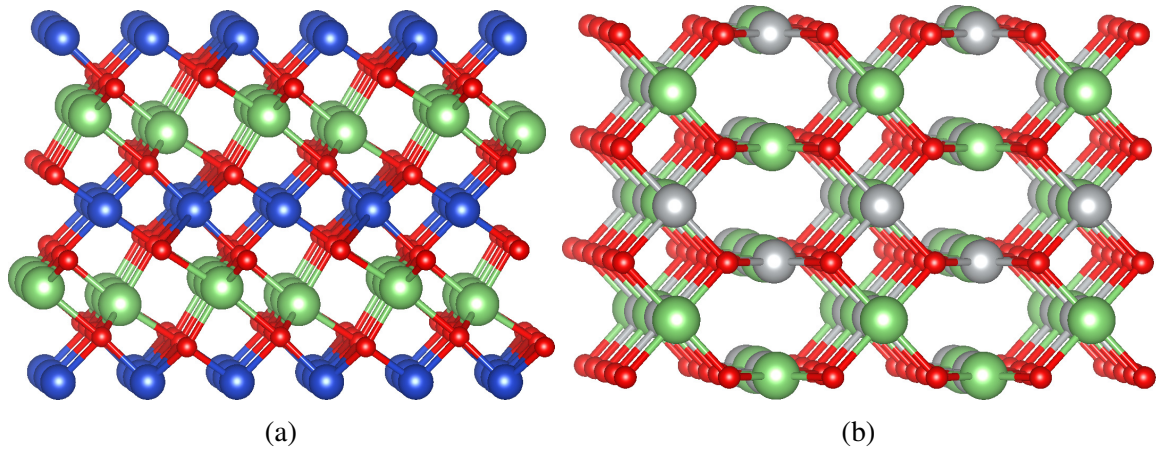


Figure 5.7 The structures of (a) CuLiO_2 (space group 2) and (b) $(\text{Ag,Au})\text{LiO}_2$ (space group 53).

is 11 meV/atom above the convex hull and it is an indirect gap semiconductor with a PBE gap of 0.7 eV. Finally, NiHO_2 is metastable at 24 meV/atom, with a monoclinic phase (space group 8) that resembles AuNiO_2 .

Lithium The structures of $(\text{Cu,Ag,Au})\text{LiO}_2$ are composed of lines of alternating (Cu,Ag,Au) and Li bonded by O in a three-dimensional arrangement (see Fig. 5.7). The Ag and Au compounds crystallize in an orthorhombic structure (space group 53). A distortion of this structure leads to the monoclinic phase (space group 12) found in the databases for CuLiO_2 , and a large distortion of this structure reduces the symmetry to the space group 2 that we find as the ground-state of CuLiO_2 . All compounds are indirect band-gap semiconductors, with PBE gaps of 0.5 eV (Cu), 0.5 eV (Ag), and 1.1 eV (Au). For NiLiO_2 we found a thermodynamically stable structure (space group 14), 13 meV/atom lower than the lowest structure found in the databases. It is formed by hexagonal layers of Lithium, intercalated by units of NiO_2 , similar to the structure of CuTiO_2 (Fig. 5.13).

Sodium The compounds containing Na result in two structures very close in energy and competing for the ground-state: the orthorhombic structure (see Fig. 5.8a) that is the structure of the ternary oxides containing K, Rb, and Cs, and the monoclinic phase that is a slightly distorted version of the structure of $(\text{Ag, Au})\text{LiO}_2$. For CuNaO_2 we find that the former is the ground state (a mere 7 meV per atom below the monoclinic structure present in databases), while for Ag and Au the latter is more stable. These compounds are all indirect-gap semiconductors with PBE gaps of 0.4 eV (Cu), 0.6 eV (Ag), and 1.1 eV (Au).

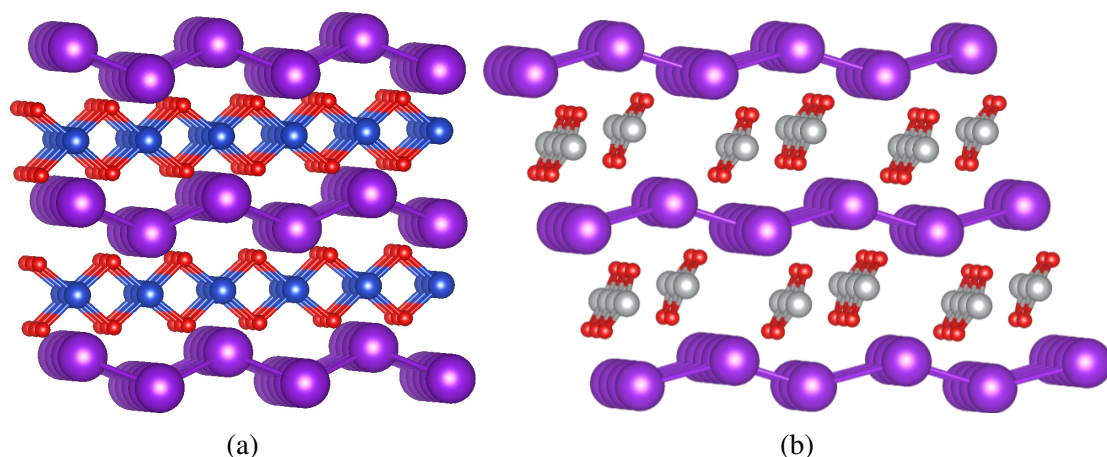


Figure 5.8 The structure of (a) $(\text{Cu,Ag,Au})(\text{K,Rb,Cs})\text{O}_2$ (space group 63) and (b) NiKO_2 (space group 12).

Potassium, Rubidium, Cesium The compounds of the form $(\text{Cu,Ag,Au})(\text{K,Rb,Cs})\text{O}_2$ crystallize in an orthorhombic structure (space group 63), characterized by corrugated square planes of (K,Rb,Cs) intercalated with flat stripes of CuO_2 where each Cu atom shares four O atoms with two neighboring Cu (see Fig. 5.8a). All these materials are semiconducting with an indirect PBE gap between 0.8 and 1.5 eV that increases with the size of the atoms from Cu to Au and from K to Cs. Note that this is also the lowest energy structure we found for CuNaO_2 . $\text{Ni}(\text{K,Rb,Cs})\text{O}_2$ crystallizes in a monoclinic structure (space group 12), although with different arrangements: Rb and Cs compounds have a structure that looks like a distortion of Fig. 5.8a. NiKO_2 is 11 meV/atom above the convex hull and also has a structure similar to the other (Rb,Cs) compounds, but in this case the NiO chains have a different orientation (Fig. 5.8b). These are all semiconducting, with electronic gaps of, respectively, 1.0 eV, 1.9 eV and 1.9 eV.

5.2.3 Group IIA

Magnesium The element Mg is contained in two ternary oxides with Cu (43 meV/atom from the convex hull) and with Au (36 meV/atom). They are both orthorhombic, but quite dissimilar: the structure CuMgO_2 (space group 67) is a distorted variation of the tetragonal unit-cell (space group 123, see Fig. 5.10) of, e.g., CuCaO_2 . AuMgO_2 is more complicated: its crystal structure (space group 65) is similar to the one of $(\text{Ag,Au})\text{LiO}_2$ (see right panel of Fig. 5.7). Both structures are metallic.

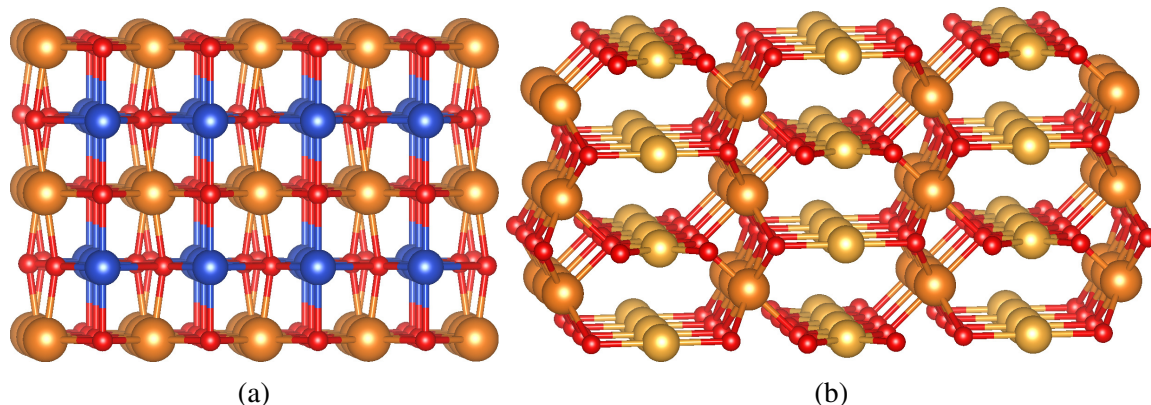


Figure 5.9 The structures of (a) CuMgO_2 (space group 67) and (b) AuMgO_2 (space group 65)

Calcium, Strontium, Barium Most of the $(\text{Cu,Ag,Au})(\text{Ca,Sr,Ba})\text{O}_2$ ternaries crystallize in a tetragonal lattice with space group 123 (CuCaO_2 , AgBaO_2) or in a distorted version with a monoclinic space group 12 (AgCaO_2 , AgSrO_2 , AuSrO_2 , AuBaO_2). These two lattices are represented in the top panels of Fig. 5.10. On the other hand, CuSrO_2 and CuBaO_2 have an orthorhombic structure (space group 63) that resembles to some extent the one of AuMgO_2 . Most of these materials are metallic, with the exception of the ones that crystallize in the monoclinic phase: AgSrO_2 has a PBE gap of 0.6 eV, AuSrO_2 of 1.4 eV and AuBaO_2 of 1.2 eV. AgCaO_2 has zero PBE gap, but the small density of states at the Fermi surface and the results for the other compounds suggest that this may just be due to the well known gap underestimation of the PBE, and that a quasiparticle gap may open up when more sophisticated methods are used. Concerning the thermodynamical stability of these compounds, CuCaO_2 is at 3 meV/atom above the hull, while AuSrO_2 is at 33 meV and AuBaO_2 at 31 meV.

5.2.4 Transition metals

Vanadium The monoclinic structure (space group 12) of CuVO_2 is very similar to the one of AgPbO_2 (see Fig. 5.14). This compound has a gap of 1.0 eV and is 11 meV/atom above the convex hull.

Manganese The oxide phases containing Mn (space group 12) can be seen as distorted delafossites, where the O atoms are slightly displaced from their symmetry positions (CuMnO_2 , AuMnO_2), or with a different stacking (AgMnO_2). The Au compound is metallic whereas the Ag and Cu have a PBE gap of 0.4 and 0.1 eV.

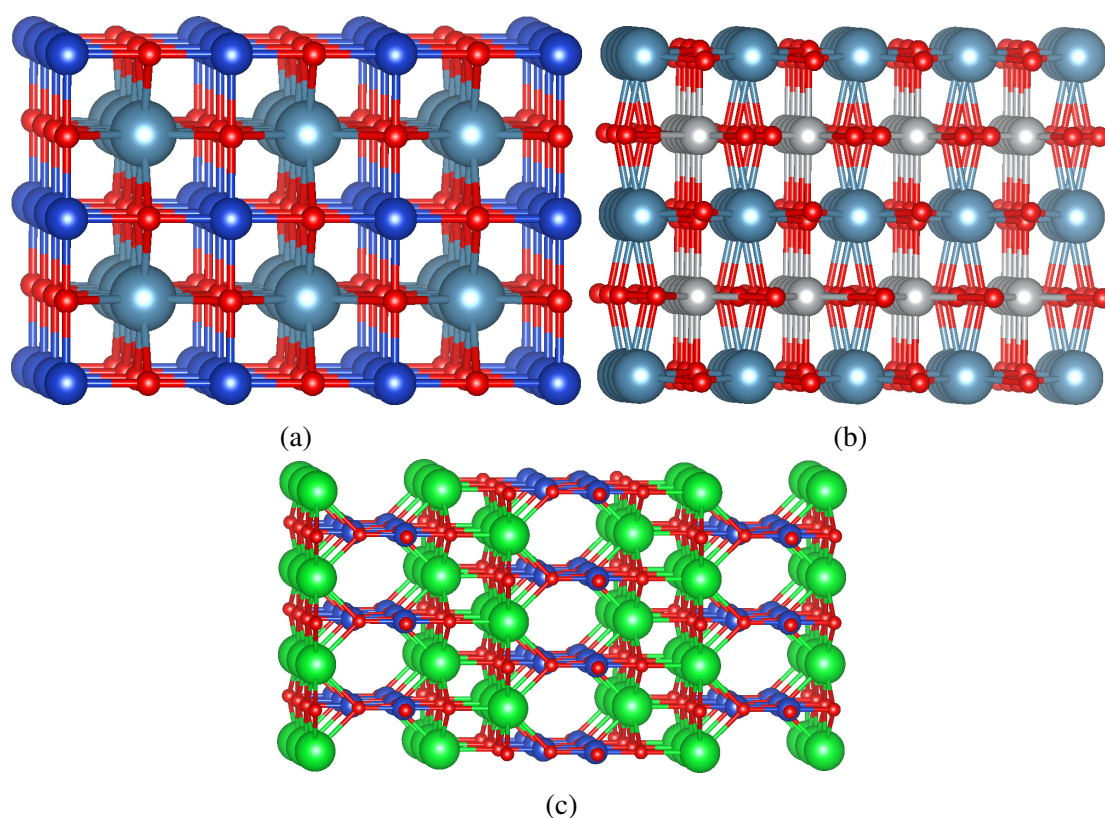


Figure 5.10 The structures of (a) CuCaO_2 (space group 123), (b) AgCaO_2 (space group 12), and (c) CuSrO_2 (space group 63).

Palladium, Platinum The two Cu compounds with Pd and Pt crystallize in the orthorhombic structure of $(\text{Ag,Au})\text{LiO}_2$ (see right panel of Fig. 5.7). While the Pd compound is thermodynamically stable, CuPtO_2 is 6 meV/atom above the convex hull. Both are metallic. On the other hand, the two Ag phases have a monoclinic structure (space group 10) similar to AuPbO_2 (see Fig. 5.14), but where the Ag planes are not distorted (increasing the symmetry of the system). AgPdO_2 is stable with a small PBE gap of 0.1 eV. AgPtO_2 has an indirect gap of 0.3 eV, lying 19 meV above the hull. Finally, AuPdO_2 it is a metallic distorted delafossite structure (space group 12) similar to the one of $(\text{Cu,Ag,Au})\text{BiO}_2$ (see Fig. 5.15a).

Copper, Silver, Gold CuAgO_2 has a orthorhombic lattice characterized by square flat layers of Ag intercalated with ribbons of CuO_2 . The main difference to the structure of CuPbO_2 (see Fig. 5.14) is that the four O atoms are shared in this case with two Cu neighbors and not with four. On the other hand, CuAuO_2 crystallizes in a monoclinic structure (space group 12) very similar to the Au delafossite structure, with Au hexagonal flat planes separated by CuO_2 layers, but where the O atoms are slightly displaced thereby reducing the symmetry

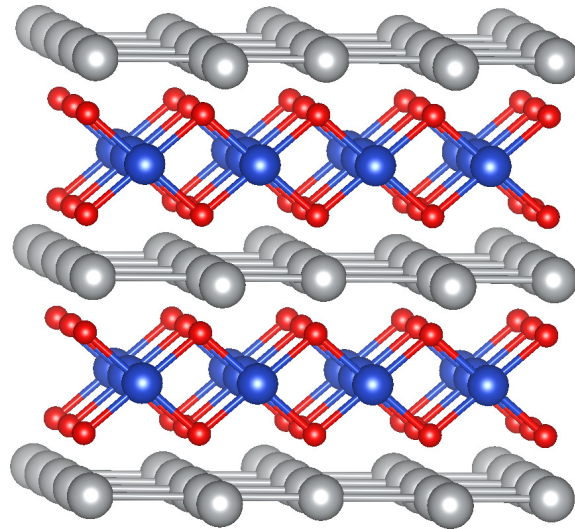


Figure 5.11 Structure of CuAgO_2 (space group 47).

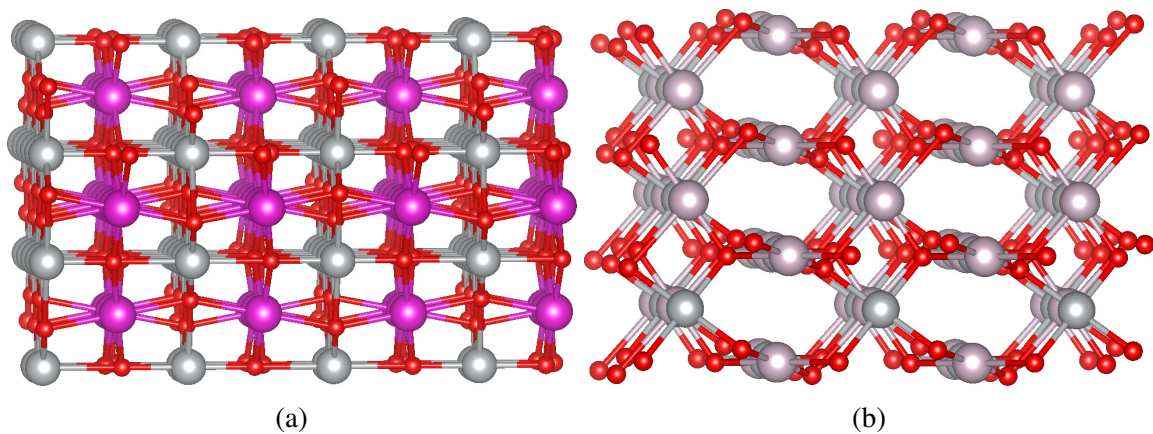


Figure 5.12 Structure of (a) AgCdO_2 (space group 12) and (b) AgHgO_2 (space group 2).

from trigonal to monoclinic. This is, in fact, the structure that can be found in the databases for CuAgO_2 . Finally, AgAuO_2 can again be seen as a distorted Au delafossite, leading to a monoclinic phase with space group 14. While CuAgO_2 and CuAuO_2 are metallic, AgAuO_2 is an indirect gap semiconductor with a PBE gap of 0.6 eV.

Cadmium, Mercury CuHgO_2 has the same monoclinic structure as CuAuO_2 , and so it can be seen as a deformed Hg delafossite. It is a metal and it lies 43 meV/atom above the convex hull of thermodynamic stability. On the other hand, AgCdO_2 crystallizes in a deformed version (see Fig. 5.12) of the tetragonal structure of, e.g., CuCaO_2 (see Fig. 5.10). This is a metal, 23 meV/atom above the hull. The next compound, AgHgO_2 has as ground state a low symmetry structure (space group 2, see right panel of Fig. 5.12) that can be seen as a

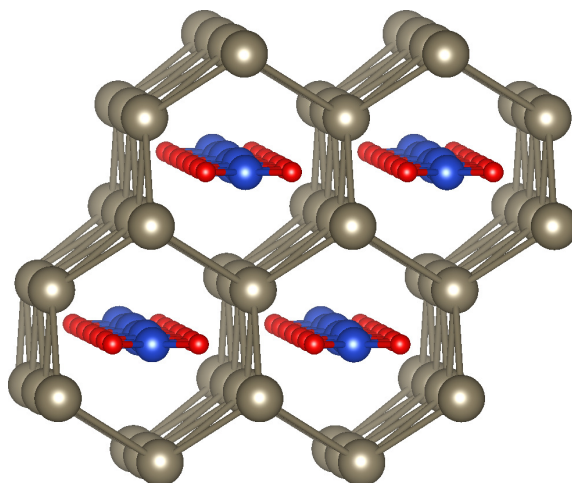


Figure 5.13 The structure of CuTiO_2 (space group 11).

small distortion of the orthorhombic phase of $(\text{Ag,Au})\text{LiO}_2$ (see right panel of 5.7). This is a metal, 27 meV above the hull. Finally, AuCdO_2 has a similar crystal structure as AgHgO_2 , also with space group 2, but with the metal atoms forming lines of Au and of Cd (i.e., they are not alternating). This is a quasi-direct gap semiconductor with a PBE gap of 0.9 eV.

Thallium The ground-state of CuTlO_2 , in contrast to the Ag and Au compounds that crystallize in the delafossite structure, is a monoclinic lattice (space group 11), characterized by hexagonal channels made of Tl filled with flat stripes of CuO_2 . This phase is an indirect band-gap semiconductor with a PBE gap of 0.4 eV. A (metallic) delafossite structure is also present as a meta-stable phase, around 14 meV/atom higher than the ground-state.

Lead $(\text{Cu,Ag,Au})\text{PbO}_2$ oxides are characterized by Pb planes separated by $(\text{Cu,Ag,Au})\text{O}_2$ layers (see Fig. 5.14). For CuPbO_2 , Pb forms a square lattice while each Cu shares four O atoms with four Cu neighbors, while for the Ag compound, Pb forms a hexagonal lattice with isolated AgO_2 units in between. Finally, the AuPbO_2 structure is somewhat intermediate between the Cu and Ag compounds: the Pb layers form a distorted hexagonal lattice and each Au has two O atoms and shares an extra two. The Cu phase (space group 74) is metallic and 43 meV above the convex hull, the Ag compound (space group 12) is a 0.3 eV semiconductor and 32 meV above the hull, and finally Au forms a semiconducting phase (space group 2) with an indirect PBE gap of 0.4 eV and it is 15 meV above the convex hull.

Bismuth The ternary oxides with Bi are indirect-gap semiconducting phases with PBE gaps of 1.0 eV (Cu), 1.4 eV (Ag), and 1.3 eV (Au). Their monoclinic space group 11 corresponds to an atomic arrangement that can be seen as a distorted delafossite, with a dimerization of

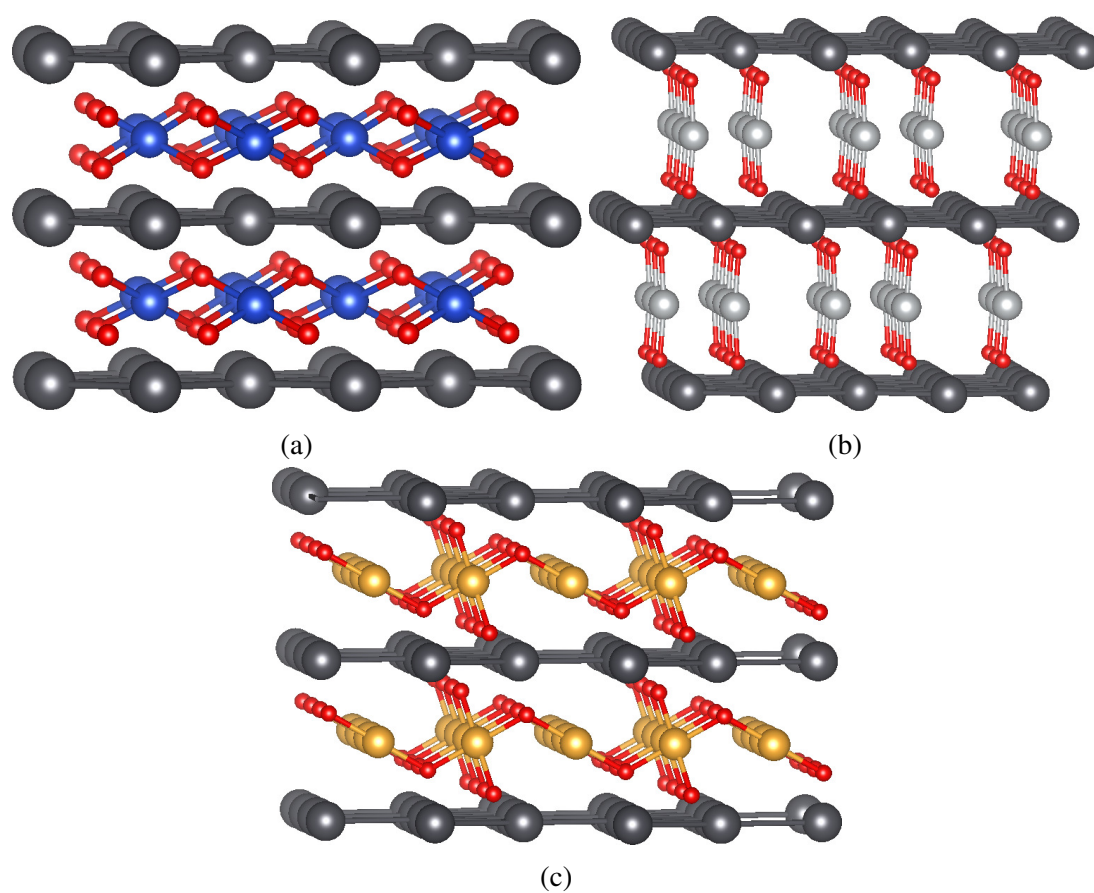


Figure 5.14 Structures of (a) CuPbO_2 (space group 74), (b) AgPbO_2 (space group 12), and (c) AuPbO_2 (space group 2).

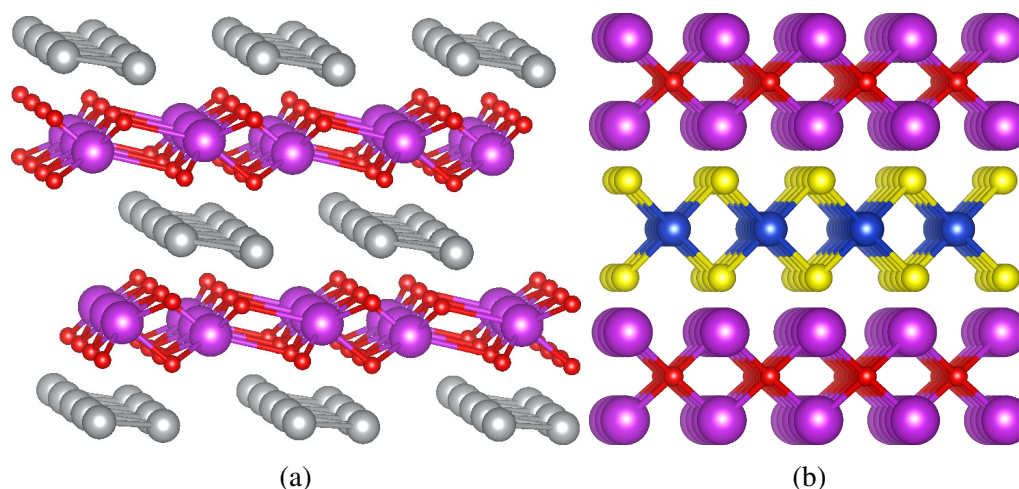


Figure 5.15 Distorted delafossite structure of $(\text{Cu,Ag,Au})\text{BiO}_2$ (compare with Fig. 5.5) (a) and tetragonal structure of CuBiOS (space group 129).

the chains of Ag and BiO_2 (see Fig. 5.15a). The delafossite structure remains, however, a meta-stable phase of this composition, around 40 meV/atom higher than the ground-state. Although not strictly stable thermodynamically, these structures are remarkably close to the convex hull at 8 meV/atom (Cu), 3 meV/atom (Ag), and 40 meV/atom (Au). Finally, for CuBiOS we found a thermodynamically stable tetragonal structure with space group 129 (see Fig. 5.15b).

Scandium CuScOS crystallizes in metastable orthorhombic structure (space group 59, see Fig. 5.16a), 18 meV/atom above the convex hull. It has a PBE gap of 1.4 eV.

Yttrium For CuYOS we found a tetragonal structure (space group 129), similar to the one of CuBiOS (Fig. 5.15b). It is semiconducting, with a PBE gap of 0.5 eV and it lays 40 meV/atom above the convex hull of stability.

5.2.5 Halogens

Fluorine $(\text{Cu,Ag,Au})\text{FO}_2$ compounds crystallize in a monoclinic lattice (space group 4) characterized by $(\text{Cu,Ag,Au})\text{FO}_2$ layers (see Fig. 5.16b). These are all semiconducting structures, with PBE electronic gaps of 0.8 eV (CuFO_2), 0.6 eV (AgFO_2), and 1.1 eV (AuFO_2). For NiFO_2 we found a stable, low symmetry structure (space group 2). It is characterized by planar units of (Ni,K,O) intercalated by lines of oxygen molecules (see Fig. 5.16c).

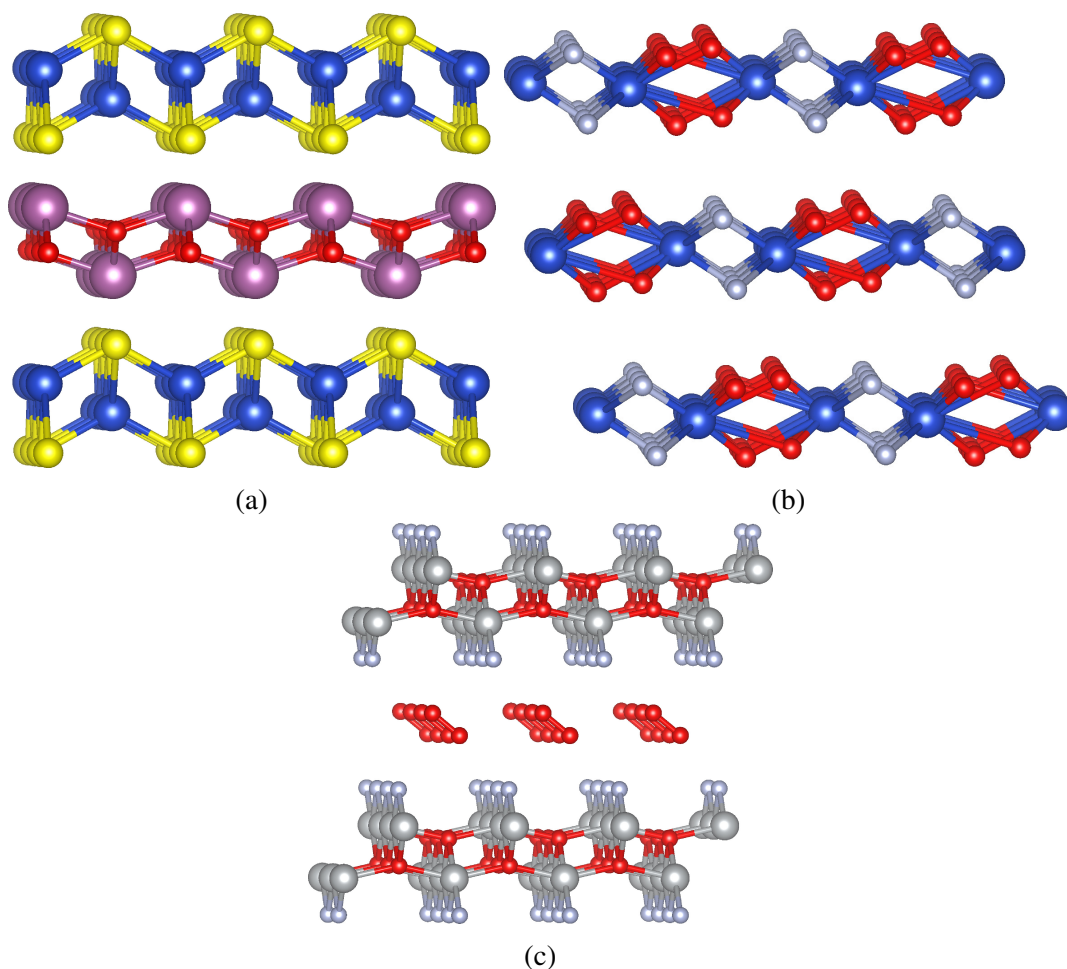


Figure 5.16 The structure of (a) CuScOS (space group 59), (b) (Cu,Ag,Au)FO₂ (space group 4) and (c) NiFO₂ (space group 2).

Chlorine, Bromine Cu(Cl,Br)O₂ compounds crystallize in a low symmetry triclinic (space group 1) lattice (see panel c of Fig. 5.17). This has some similarities to the monoclinic structure of (Cu,Ag,Au)FO₂ (see Fig. 5.16b), in the sense that they share the same CuO₂ subunits. However, in the latter structure each Cu shares four F with four neighboring Cu atoms, while in the former each Cu only shares two (Cl,Br) with two other Cu. These are thermodynamically stable structures, that are indirect gap semiconductors with PBE gap of 0.8 (CuClO₂) and 0.9 (CuBrO₂).

Ag(Cl,Br)O₂ structures are fundamentally different from all other we found in our study. It is composed of flat hexagonal layers of Ag(Cl,Br), separated by a layer of O₂ molecules (see panel a of Fig. 5.17), forming a low-symmetry triclinic lattice (space group 1). These turn out to be semiconductors with PBE gaps of 0.6 eV (AgClO₂) and 0.7 eV (AgBrO₂).

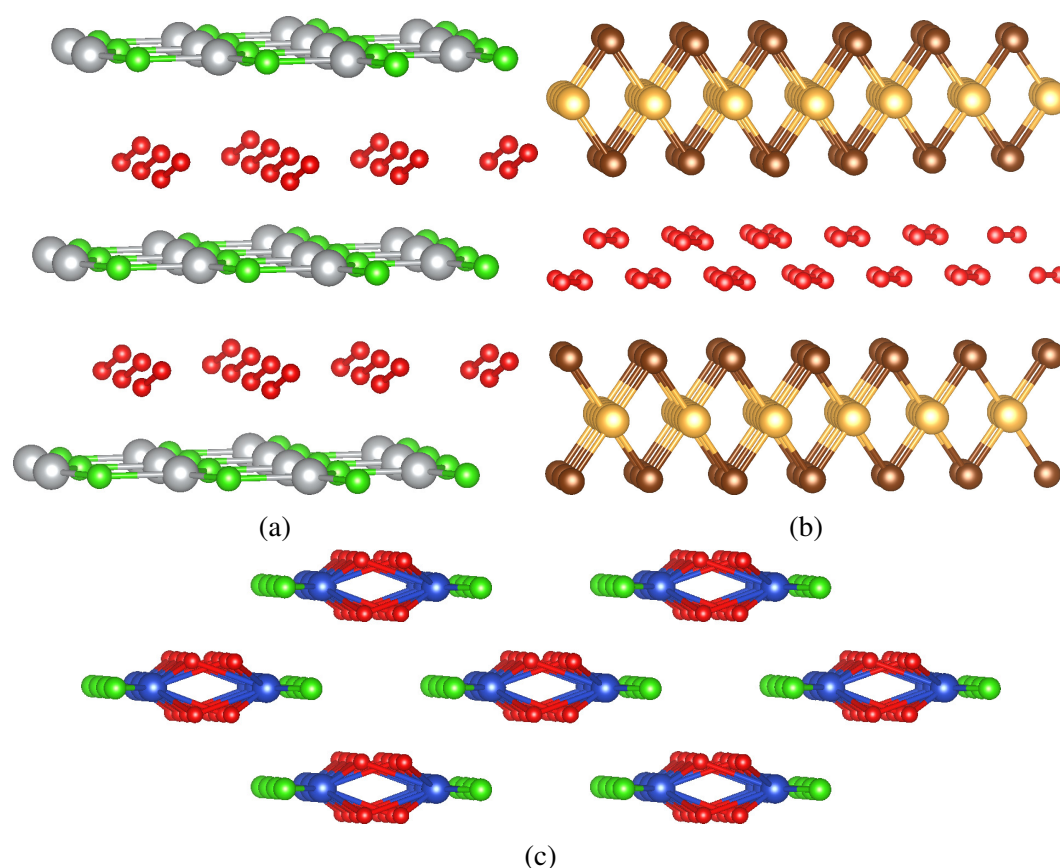


Figure 5.17 The structure of (a) $\text{Ag}(\text{Cl},\text{Br})\text{O}_2$ (space group 1), (b) $\text{Au}(\text{Cl},\text{Br})\text{O}_2$ (space group 15), and (c) $\text{Cu}(\text{Cl},\text{Br})\text{O}_2$ (space group 1).

$\text{Au}(\text{Cl},\text{Br})\text{O}_2$ compounds crystallize in a lattice that is composed of $\text{Au}(\text{Cl},\text{Br})$ layers intercalated with O_2 molecules (see panel b of Fig. 5.17). However, in this case the $\text{Au}(\text{Cl},\text{Br})$ are not flat, but form zigzag stripes with each Au bonded to two (Cl,Br) and vice-versa, leading to a monoclinic lattice (space group 15). AuClO_2 is a semiconductor with an indirect gap of 0.3 eV, while AuBrO_2 turns out to be a metal with the PBE.

Iodine CuIOS crystallizes in a metallic low symmetry structure (space group 1). It is formed by (Cu,S,O) units intercalated by SO_2 molecules (Fig. 5.18a).

5.2.6 Others

Boron AgBO_2 has a monoclinic structure (space group 9) composed by slightly buckled Ag layers, separated by BO_2 chains, where each B is connected to three O, two of which are shared with two adjacent B atoms (see Fig. 5.18b). Note that this is the same structure we

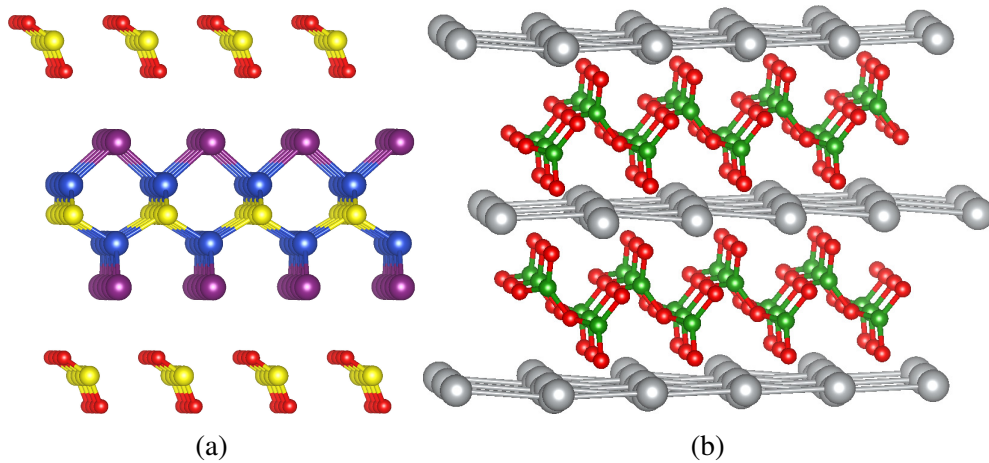


Figure 5.18 The structure of (a) CuIOS (space group 1) and (b) AgBO₂ (space group 9).

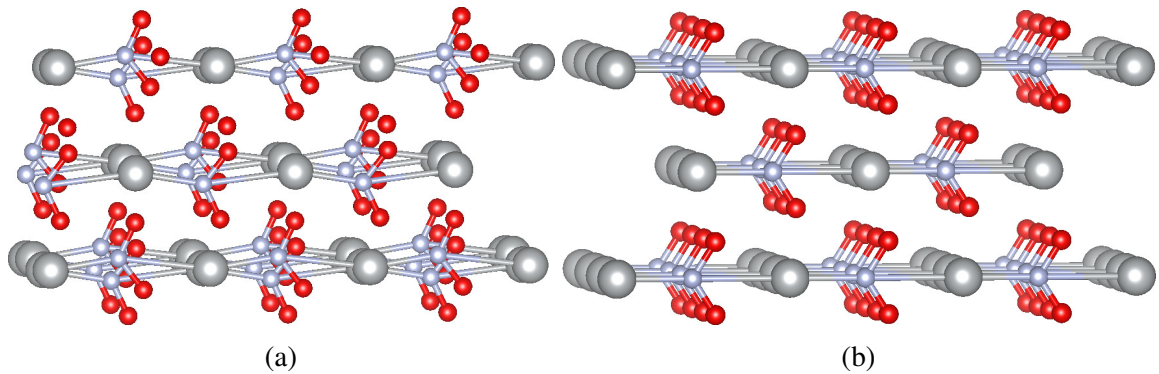


Figure 5.19 Two phases of AgNO₂, (a) the ground-state monoclinic (space group 5) and an orthorhombic (space group 44) structures.

had previously found for CuBO₂ [48]. AgBO₂ is 33 meV/atom above the hull, and it is a semiconductor with a PBE quasi-direct gap of 1.4 eV.

Nitrogen The lowest energy phase of AgNO₂ that we found is a monoclinic structure (space group 5), lying 37 meV/atom above the hull. It is composed of lines of alternating Ag and NO₂. This is a deformation of the orthorhombic structure (space group 44, see Fig. 5.19) that can be found in the databases, and that we found to be 5 meV/atom above the ground state. Both structures are indirect gap semiconductors, with PBE gaps of 1.4 eV (monoclinic) and 1.8 eV (orthorhombic).

Arsenic Also for AgAsO₂ we found a monoclinic structure (space group 5, see Fig. 5.20), composed of corrugated planes of AgAsO₂. This phase is 38 meV/atom above the hull, with a PBE indirect gap of 2.4 eV.

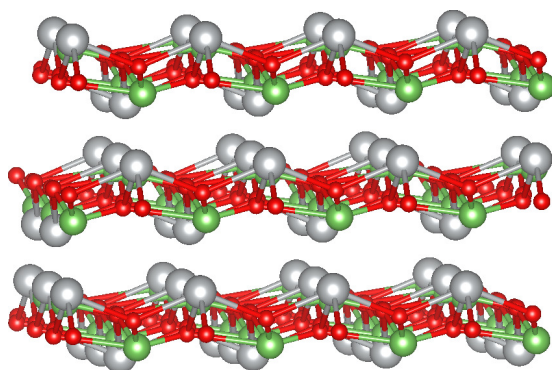


Figure 5.20 The structure of AgAsO_2 (space group 5).

Antimony CuSbOS crystallizes in a monoclinic structure (space group 8) and lays 37 meV/atom above the convex hull of stability, with a gap of 0.8 eV.

Indium For CuInOS we found a low symmetry monoclinic structure (space group 4), metallic, and 46 meV/atom above the convex hull. It resembles a distorted structure of CuBiOS and CuYOS (Fig.5.15b).

5.3 Summary and Conclusions

In this Chapter we summarized the results of structural prediction runs for 304 oxide phases of the families $(\text{Cu,Ag,Au,Ni})\text{XO}_2$ and CuXOS . From our runs we predict that there are 93 thermodynamically stable or quasi-stable (within 20 meV) compositions, out of which only 41 are included in available databases. These numbers should be compared to the 3 systems that were found in a previous study using high-throughput techniques combined with machine learning. Nevertheless, we believe that structural prediction should not be seen as a competitor of more traditional high-throughput techniques. In fact, both methods complement each other, and both should be used in synergy to speed up the experimental process of materials discovery. We tried to do the first steps in this direction, by combining structural prediction and a search based on prototype structures.

The subset of oxides that we explored include delafossite CuAlO_2 , the first delafossite *p*-type transparent conductive oxide. By calculating the band gaps and hole effective masses of the new stable compounds that we identified, we could reveal some potential candidates to outperform CuAlO_2 as *p*-type transparent conductor. These few compounds deserve in our mind further consideration, both from an experimental point of view (e.g., synthesis, structural and electronic characterization) and a theoretical point of view (e.g., study of dopability, more accurate band structure and transport calculations).

This section proves that, even if structural prediction is complex and numerically expensive, we can use modern supercomputers to investigate the stability a large number of chemical compositions. However, we still made an assumption on the stoichiometries chosen – in this case (Cu,Ag,Au)XO₂ and CuXOS. In other words, we are inputting a chemical composition and we are getting its ground state structure in return. Having the crystal structure, we can then calculate a variety of properties to assess its applicability for a target problem. In the next section we will give a step further: we will present a method where we will input a target property (properties) and get in return a material optimized for this specific purpose.

Chapter 6

Materials Design and Inverse Problem

One of the most exciting developments in condensed matter over the past years is, without doubt, materials design [7, 34, 188, 189]. This new discipline aims at solving the so-called inverse problem: given a certain desired property (or properties), discover (design) the material that possesses this property under a given set of constraints. These constraints can be related to the mechanical or chemical stability of the compounds, their price, their availability, etc. Several groups are actively working on this topic, with many projects related to energy materials including lithium batteries [7], photovoltaics [190, 191], etc.

Typically, these methods rely on the databases of *ab initio* results described before. These, can be simply filtered to yield the best material according to some objective function [14, 35] or used as a training set for some machine learning algorithm that will extrapolate the information to obtain new crystal structures with improved properties [33, 192].

Even if this framework is extremely powerful and has led to a number of significant discoveries, in our opinion it suffers from few drawbacks. First of all, it requires an enormous amount of experimental input, and in fact more than 50,000 complex synthesis and X-ray diffraction experiments had to be realized in order to obtain the current databases. Although 50,000 may seem a large number, it is certainly a very small fraction of all possible (thermodynamically) stable compounds. Of course each new experimental entry that is added to the database encompasses substantial costs in personnel, equipment and consumables. Second, any prediction based on this set will be biased by the subset of systems studied experimentally. If the solution for a given materials design problem lies in a region that has been unpopular among chemists and crystallographers, it is very unlikely that it will ever be found by any algorithm. Third, experimentally we know mostly stable stoichiometries. This means that large regions of (the unstable) phase space are completely unrepresented in the databases, which makes bridging these regions during an optimization procedure extremely difficult.

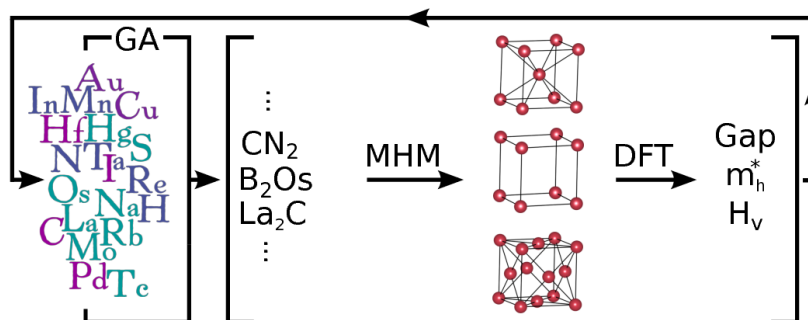


Figure 6.1 Schematic view of the on-the-fly materials design algorithm proposed.

There are other approaches to the design of new materials that do not require databases. For example, the concept of energy gradients in chemical compound space [193–198] (the so-called alchemical derivatives), transforming discrete optimization into a continuum one, has been proposed as a way to optimize molecular properties. Evolutionary approaches have also been used, although always with rather severe constraints. For example, Refs. 190 and 191 optimized optical absorption by changing the ratio and the order of Si and Ge monolayers, while in Ref. 199 the ground-state for $\text{Au}_{1-x}\text{Pd}_x$ (with variable x) alloys was found but for a fixed Bravais lattice. On the other hand, variable composition genetic algorithms were proposed to study binary phase diagrams, with application, e.g., to the Mn–B system [200].

Finally, the dream of any theoretician is to be able to provide predictions with as little experimental information as possible (ideally none). In the following we will show that this is possible, and that one can nowadays perform the inverse problem in an efficient way without resorting to databases or to any experimental input besides the periodic table of the elements and the laws of quantum mechanics.

6.1 Details of Calculations

Our approach is composed of three parts, as schematized in Fig. 6.1. In the first, we use a multi-objective genetic algorithm (GA) to vary the composition of the unit cell in order to maximize a set of properties. Then, for each individual (i.e., for each composition that stemmed from the GA) we did structural prediction to obtain its ground-state crystal structure. Finally, the property (or properties) that we want to optimize are calculated for the ground-state and possibly for the lowest-lying meta-stable structures. These are finally fed back into the GA in order to determine the better-fit parents that will generate the offspring for the following generation.

In the structure prediction step we used the minima hopping method described in Section 2.4.5 and already used in the previous Chapter. Forces and energies were obtained within density functional theory. For a given stoichiometry, the initial geometries were obtained randomly, ensuring only that the minimal distance between the atoms was at least equal to the sum of the covalent radii. At the end of the simulation, all structures higher than 200 meV per atom from the ground-state were disregarded. The remaining were reoptimized, and their properties were calculated as explained below. Details on the DFT runs are described below (Section 6.1.2).

6.1.1 Genetic algorithms

The genetic algorithm used here is slightly different from the one described in Section 2.4.3. In the latter, the GA is used to obtain the ground state crystal structure directly. Therefore, the gene is the crystal structure itself. Here, we use the genetic algorithm to, based on the best candidates, select the compositions to use in the minima hopping runs. To perform the multi-objective optimization we used the non-dominated sorting genetic algorithm–II [201]. The gene describing each individual is given by a sequence of 6 integer numbers, each one indicating a different chemical element. In order to accommodate unit cells with less than 6 atoms we introduced an empty “atom” (symbol “X”, atomic number 0). The ordering of the sequences was taken into account, such that, e.g., ABC is equivalent to BCA. The mating operator simply mixes the chemical composition of both parents, while mutations transmute randomly one element in the gene. The mutation rate was set to 10%. As an example, Fig. 6.2 shows a possible representation of the gene, the crossover and the mutation operators. In our current implementation we did not make use of a Lamarckian-type evolution as described in Ref. 199. However, we expect that such ideas could be applied to obtain a speed up of the convergence of our method.

6.1.2 Ab initio calculations

We used density functional theory as implemented in the code VASP [39, 40]. We used again the PAW datasets of version 5.2 (for compatibility with materials project [4] and OQMD [5]). We used a cutoff of 520 eV and we selected our k -point grids to ensure an accuracy of 0.002 eV/atom in the total energy. All forces were converged to better than 0.005 eV/Å. To approximate the exchange-correlation functional of DFT we used the Perdew-Burke-Ernzerhof [141] generalized gradient approximation (PBE).

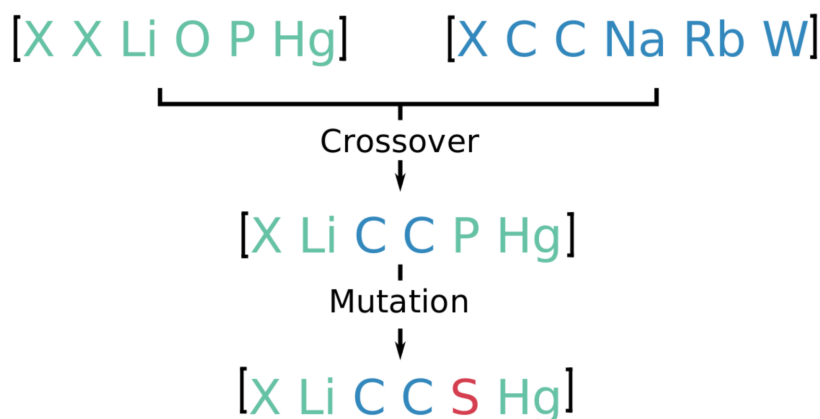


Figure 6.2 Genetic algorithm

6.1.3 Hardness evaluations

We used the model by Zhang *et al* [202] that allows for a universal calculation of the Vickers hardness for the predicted structures. This model extends the work of Šimůnek and J. Vackář [203, 204], and improves the earlier hardness models [205] based on bond strength by applying the Laplacian matrix [206] to account for the highly anisotropic and molecular systems. In order to benchmark this model, we calculated the hardness for all materials contained in the open quantum materials database [5] (around 300,000 entries). It turns out that laminar systems are correctly described as having low hardness, but the model still fails for some molecular crystals that are incorrectly assigned large values for the hardness. This is however, not a large problem, as these false positives can be easily identified by visual inspection and quickly discarded.

6.1.4 Calculation of the gaps and hole effective masses

Gaps and hole effective masses (m_h^*) were calculated using the PYMATGEN [182] and BOLTZ-TRAP [185] software packages, applying the recipe already used in the previous Chapter. We then used the higher limit estimation of m_h^* as the input value for the GA. We note that only one structure for composition was used to evaluate m_h^* , which was not always the ground-state structure. Rather, we chose the structure with largest (PBE) gap within 50 meV to the GS. Additionally, for the most promising candidates, we also calculated the gaps using the Heid-Scuseria-Ernzerhof hybrid functional (HSE06) [207]. We note that this latter functional is a screened hybrid that gives very good values for the electronic gap of small and medium gap semiconductors. In particular, the HSE06 estimate is much better than the PBE one, that has the tendency to underestimate substantially the electronic gaps.

6.2 Results and Analysis

As a first showcase demonstration of our method, we decided to search for superhard materials. The hardness is a technologically important property that has been the subject of numerous studies over the past decades. We performed two independent GA runs with 15 generations each. We used a population of 100 individuals, with a maximum of six atoms in the unit cell. We allowed all elements up to bismuth, but excluding the rare gases (which do not form hard compounds) and the lanthanides. We note that these choices were arbitrary, and ultimately decided by efficiency reasons. The initial generation was chosen such that each individual contained four *random* atoms in the unit cell. We made sure that each element appeared a minimum number of times in the initial generation (see bottom line of Fig. 6.4). Finally, the mating operations mixed the elements of both parents, while the mutations operated the alchemical transmutation of the elements. In total the structural prediction visited 121,000 minima for 1,500 compositions, of which 33,000 unique structures were further analyzed. All calculations were performed in around 1 million computer hours, a number relatively modest in comparison to the supercomputing resources currently available.

The evolution of the hardness during our GA simulations is shown in Fig. 6.3 for our two independent runs. The lines are a guide to the eye and represent the maximum (top line), average (middle line), and minimum (bottom line) hardness in a given generation. Some of the most relevant compounds that appeared during the evolution are also indicated in the figure. The average hardness increases almost monotonically, as the GA narrows the search space. Moreover, diamond (labeled “C” in the plot”) appears already in the 9th generation in run I, and in the 5th generation in run II. This is somewhat surprising as, up to that point, only a few hundred materials had been tested, which should be compared to the size of the search space that contains more than *61 million* possible compositions. We finally note that the path from the random initial materials to diamond goes through very unstable structures, obviously not present in any experimental database. This is certainly a key for the efficiency of the method.

To understand how the method works we plot, in Fig. 6.4, an histogram measuring the frequency with which each element appears in a given generation. For the initial generation (the bottom line) there is an essentially uniform distribution (the zeros correspond to the elements explicitly excluded). This simply reflects our random choice of compositions for the starting generation. However, rather quickly several elements are excluded from our population, while others increase substantially their frequency. Among these latter there are H, B, C, N, Si, P, etc., elements known to yield hard materials due to their short covalent bonds [208–211], and several transition metals like Ru, Rh, Os, Ir, etc. that form hard nitrides, borides, carbides, etc. [212, 213] In a way, the GA rediscovering, in a fully automatic and *ab*

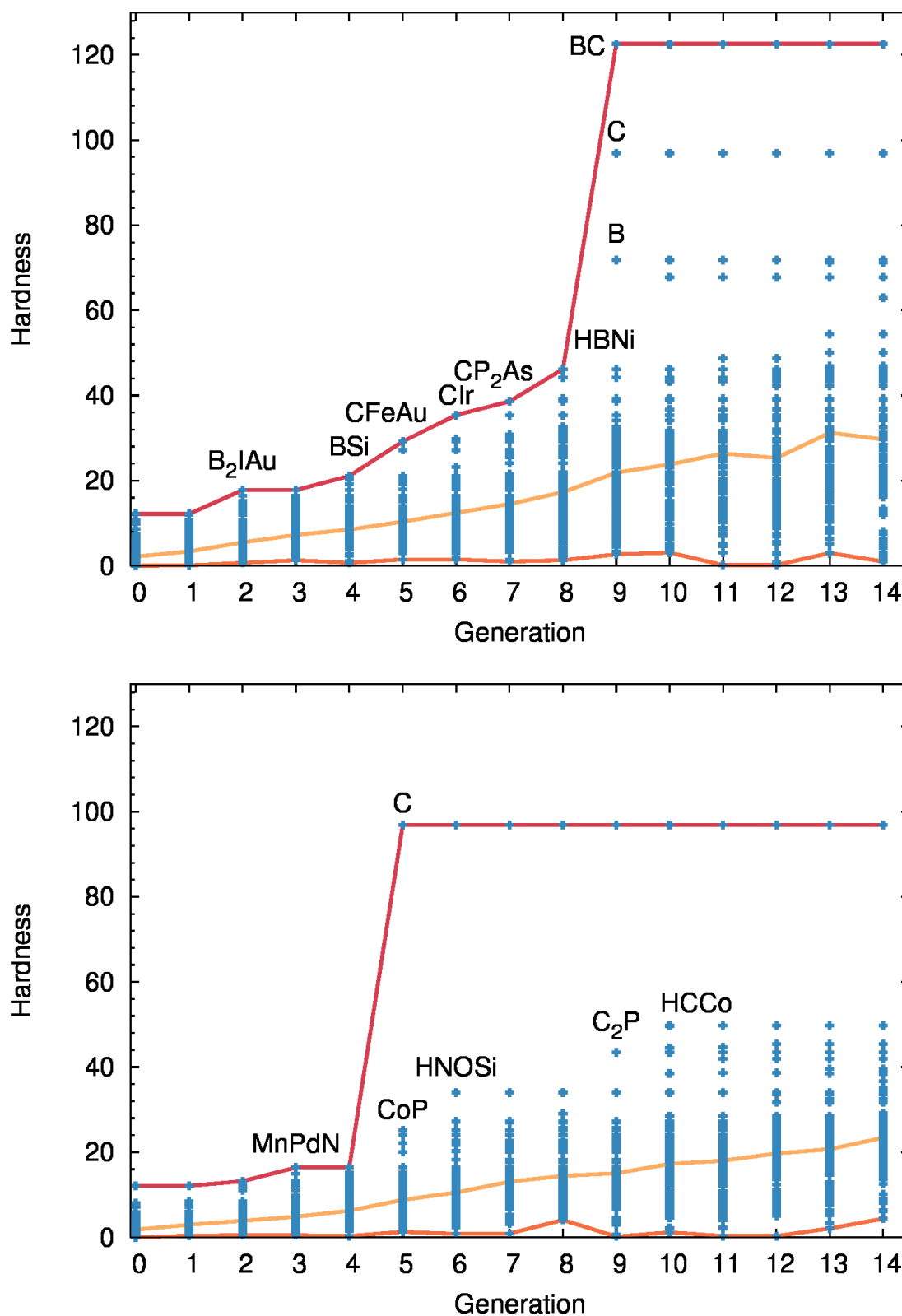


Figure 6.3 Evolution of the maximum (red line), minimum (orange line), and average (yellow line) hardness as a function of the generation for the two GA runs described in the text. Each point corresponds to the maximum hardness of a specific composition. Some relevant compounds are also indicated.

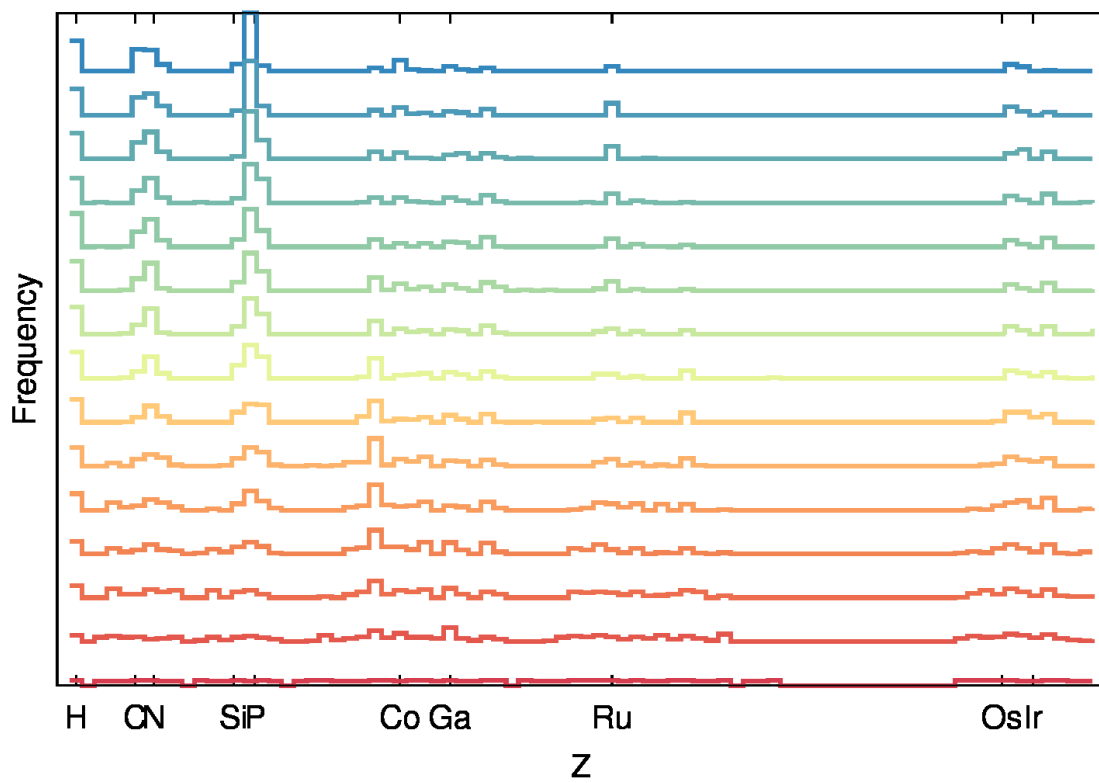


Figure 6.4 Frequency of the elements present in each generation of the hardness for the two GA runs described in the text. The bottom (red) line corresponds to generation 0, and the top (blue) line to generation 14.

initio way, some of the basic intuition concerning hardness that physicists and metallurgists developed over the centuries.

Let us now take a better look at the superhard materials (with hardness greater than 40 GPa) that came out from our simulations. They are summarized in Table 6.1. For the sake of comparison, we also include the distance to the convex hull of thermodynamic stability, the spacegroup of the structure in question, the bulk and shear moduli.¹

Without great surprises, the hardest materials on this list are composed of B, C, and N. The only structure harder than diamond is a metastable low symmetry structure of BC. In second place comes diamond, that also exhibits the highest bulk and shear moduli of all materials we looked at. For curiosity, we also found a carbon allotrope with a hardness higher than diamond, but too high in energy to enter our list. Then comes CN₂ followed by a meta-stable allotrope of boron (that has a larger hardness than any other known boron structure present in the open quantum materials database [5]) and by several boron carbides. All these materials are characterized by short and strong covalent bonds. Further down on the list we can also find a few transition metal nitrides (MnN, OsN), and several materials containing hydrogen.

We also obtained a few false positives, such as HCCo, H₃NO, or C₂P, as can be seen by their low bulk and shear moduli. This is due to the current limitations of the model used to estimate the hardness, but these cases are usually simple to spot and to filter out. For example, H₃NO turns out to be a molecular crystal that the model failed to recognize as such. We should also note that most of the materials present in the table are not thermodynamically stable, as can be seen by the finite value of E_{hull} , i.e., they can a priori decompose to other compounds or to more stable phases of the same compound. However, superhard materials are usually quite compact, and therefore are normally stabilized by pressure. It is therefore not unthinkable that some of these phases can be produced by a high pressure synthesis procedure, analogously to diamond (the second entry of the list).

As a more complicated test we decided to look at transparent conductors. These materials were already the subject of the previous Chapter, where details on their properties and literature can be found. Just a recall to put the problem in perspective here: the two key properties we are interested in are the electronic band gap, that has to be sufficiently large to ensure transparency, and the hole effective mass, that needs to be small to allow for mobile carriers. Such requirements can therefore be easily accommodated in our framework using a multi-objective optimization algorithm.

We performed 20 generations with a setup similar to the hardness runs. In total we investigated 1,100 compositions, leading to 72,000 minima, of which 19,000 were further

¹bulk and shear moduli were calculated by R. Sarmiento-Pérez [22]

Table 6.1 Superhard materials found during our GA simulations. We show the space group of the structure (spg), the distance to the convex hull of stability (E_{hull} in meV), the Vickers' hardness (in GPa), and the bulk and shear moduli (in GPa).

system	spg	E_{hull}	hardness	bulk	shear
BC	5	413	123	304	270
C	227	136	97	444	526
CN ₂	119	722	91	423	300
B	166	177	72	215	202
BC ₃	25	308	71	359	321
BC ₂	1	612	68	261	141
B ₃ C ₂	1	452	63	162	82
C ₂ Si	166	497	54	268	273
HFe	216	164	52	226	95
HB	12	660	50	205	183
NMn	216	0	50	283	26
HCCo	8	625	50	92	23
HNi ₂	123	40	49	220	85
HC ₂	2	457	47	275	184
HBNi	1	401	46	123	12
H ₃ NO	8	314	45	38	10
HNi	44	14	45	191	23
CFe	216	479	44	260	55
C ₂ P	8	554	44	90	96
B ₂ C	8	383	43	208	62
B ₂ C ₃ Si	1	345	42	204	162
NOs	119	410	42	300	86

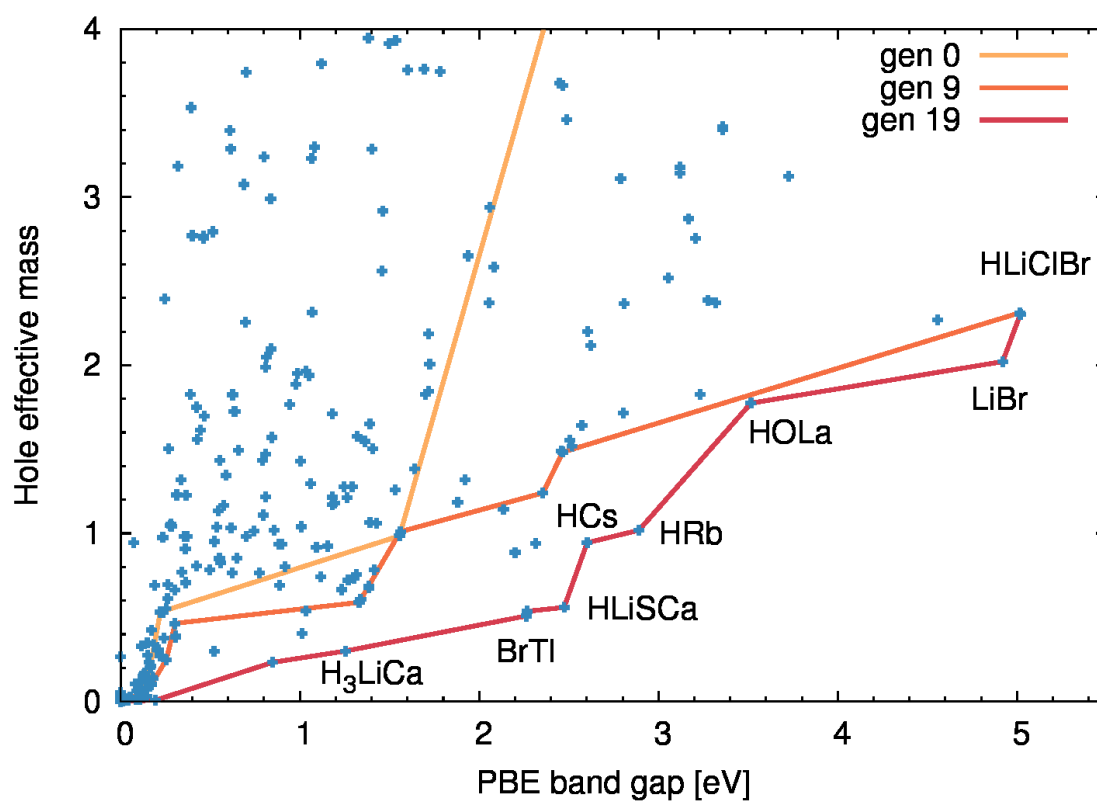


Figure 6.5 Average hole effective mass versus electronic band gap for all structures found in our run. The lines indicate the Pareto front for generations 0 (magenta), 9 (dark blue) and 19 (light blue).

analyzed. Our results are summarized in Fig. 6.5 where we plot the average hole effective mass (in units of the electron mass) versus the electronic band gap (in eV). Note that this latter quantity was calculated using standard DFT, so its value is consistently underestimated. Again, our GA method works perfectly. The Pareto front, i.e., the line connecting the structures with best gap for each effective mass (or vice-versa), is improved gradually from generation to generation. Several materials appear with large gaps and small hole effective masses that are good candidates for transparent conduction. Table 6.2 summarizes all structures with gap larger than 1.0 eV and average hole effective mass smaller than 1.5 electron masses. We list the crystallographic space group, the distance to the convex hull of thermodynamic stability (E_{hull}), the distance of the calculated structure to the lower energy structure found (Δ_{GS}), the electronic gap calculated with the PBE and the HSE06 functionals, and the average hole effective mass.

The evolution of the composition as a function of the generation, for the simultaneous optimization of the band gap and the hole effective mass, can be found in Fig. 6.6. In this case, the interpretation of the plot is more complicated than for the optimization of the hardness, as most of the successful structures are combinations of metallic elements with non-metallic elements, and therefore it is less likely that an element disappears from the population during the evolution process.

It is again interesting to understand how the GA worked. Taking random compositions, the probability of finding semiconducting systems is fairly low. For example, our 0th generation contained only 13 semiconductors out of 100 individuals. The first step in the optimization is therefore to find semiconductors. This can be achieved, e.g., by making molecular crystals formed mainly by non-metals or by combining metallic and non-metallic elements in the same structure. As the first possibility will yield very low effective masses, the final generation contains almost exclusively compounds of the latter kind. This again shows how the GA algorithms can rediscover basic chemical rules without any human intervention.

6.3 Summary and Conclusions

In conclusion, we propose a new method to design on-the-fly new materials with tailored properties. Our first test, maximizing the hardness or at the same time maximizing the electronic gap and the hole effective mass were extremely successful, with several interesting, unknown materials stemming from the simulations. This shows that our method is not only perfectly feasible, but also efficient with current computer resources. Of course any other property that can be calculated in a computer can be optimized, including the band gap, the

Table 6.2 Best transparent conductive materials found during our simulations. We show the distance to the convex hull of stability (E_{hull} in meV), the distance to the GS structure found (Δ_{GS} in meV), the space group, the gap in the PBE and the HSE06 approximations (in eV), and the average hole effective mass (m_h^* in electron masses). These latter two were calculated with the Perdew-Burke-Ernzerhof approximation [141] to the exchange-correlation potential.

system	spg	E_{hull}	Δ_{GS}	gap (PBE)	gap (HSE06)	m_h^*
PZnGeSeCs	1	57	11	1.06	1.41	1.29
ClKBrCdIn	8	79	38	1.25	1.69	1.28
HSSbTe	1	63	20	1.18	1.80	1.21
HSeCdTl	160	89	17	1.03	1.80	0.54
HSSb	8	173	22	1.01	1.80	1.04
HCaZnSb	8	0	1	1.01	1.91	0.41
HPCdTe	1	143	49	1.09	2.01	0.92
HSNbTe	1	0	0	1.27	2.03	0.72
OPTeTl	1	197	10	1.26	2.06	1.21
BeSZnTe	160	151	0	1.23	2.16	0.67
CaSeCdTe	156	124	3	1.41	2.24	0.78
SCa2Te	166	50	0	1.38	2.37	0.69
FSiCaSeTeTl	1	225	48	1.15	2.37	0.92
BePSCs	1	272	0	1.41	2.41	1.50
SCaZn	156	496	1	1.30	2.45	0.73
H2SbCs	1	42	0	1.56	2.46	0.98
HLiBrSbTe	8	119	6	1.53	2.46	1.26
OP	8	284	0	1.33	2.50	0.59
LiFCaSeTe	1	233	10	1.32	2.54	1.58
H2STe	1	194	4	1.00	2.64	1.43
HSeCdAu	1	154	2	1.29	2.67	1.28
H2CaSbCs	8	134	0	1.92	2.71	1.32
HSRh	1	148	0	1.36	2.79	1.55
CPTeCs	8	573	12	1.64	2.89	1.38
OZnGeSe	8	169	42	1.39	2.89	1.07
H2NAu	1	233	0	1.12	2.97	0.74
MgTe	216	1	1	2.31	3.13	0.94
HLiCaTe	6	103	34	2.14	3.18	1.14
HRbTe	1	0	0	2.36	3.23	1.24
HSZnAu	1	163	0	1.88	3.27	1.19
HTeCs	8	0	0	2.46	3.33	1.49
HFCaTe	1	133	0	2.51	3.48	1.55
BrTl	6	1	29	2.26	3.71	0.51
H3LiCa	221	28	0	1.25	3.95	0.30
HLiSCa	38	84	0	2.20	4.23	0.89
HCs	4	0	32	2.60	4.26	0.94
HRb	225	0	0	2.89	4.74	1.02

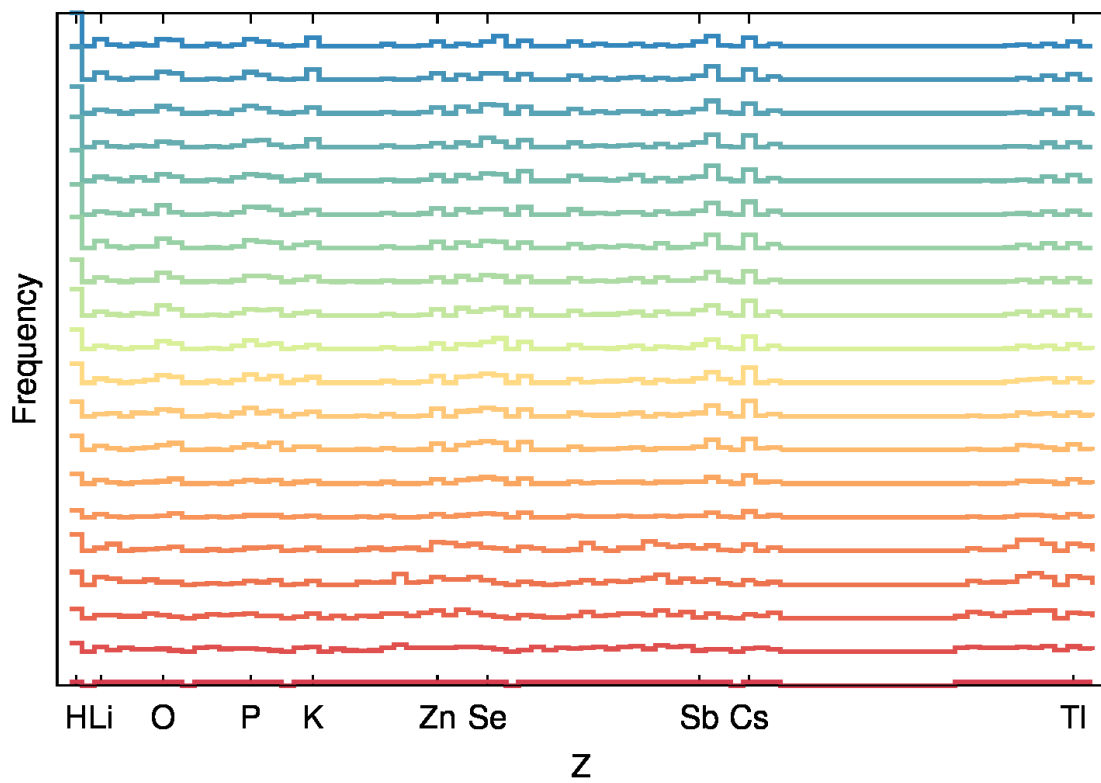


Figure 6.6 Frequency of the elements present in each generation of the gap/hole effective mass GA runs. The bottom line corresponds to generation 0, and the top line to generation 19.

Seebeck coefficient, the superconducting transition temperature, or even the price of the constituents.

Chapter 7

Summary and Conclusions

In this thesis, we used a combination of high-throughput and *ab initio* global structure prediction methods to study a wide range of different systems. In the following, a summary of the most notable results is presented.

Radial collapse of Carbon Nanotubes We studied the collapse of carbon nanotubes (CNTs), in a bundle and individualized in water, using the density functional tight-binding method. For bundles, We showed that several discrepancies found in the literature can be explained by the different number of carbon nanotubes in the unit cell and by the theoretical framework employed. Moreover, we obtained collapse pressures compatible with the ones in experimental works. For individualized CNTs, we observed different behaviours, depending on the water filling ratios: low filling ratios tend to destabilize slightly the CNTs, leading to modifications on the CNT cross section at pressures lower than for empty tubes. For higher concentrations of water, we see a consistent increase in the collapse pressure with the increased filling ratio, in accordance with experimental data, even if the calculated collapse pressures do not match perfectly experimental data. Finally, we observe that unusual states of water can be found in the collapsing / collapsed nanotubes. These can range from nanotube-like to 2D sheet-like planes of water, depending on the diameter of the CNT and on the pressure.

Type-I Silicon Clathrates Using high-throughput computational techniques we investigated the stability of type-I Si clathrates. We found several potentially stable new clathrate phases, and we reproduced the vast majority of experimental results. Based on these predictions, a new Be-doped clathrate, namely $\text{Ba}_8\text{Be}_{3.7}\text{Si}_{42.3}$, was successfully synthesized. This clathrate phase would probably be missed experimentally since it can not be expected based on the simple Zintl-Klemm-rule. Likewise, as we are not bounded by the price, availability,

toxicity, etc, of the elements, we were able to predict unusual doping combinations that are traditionally hard to access in the laboratory.

New p-type transparent conducting oxides by global structure prediction Combining structural prediction and a search based on prototype structures, we studied 304 oxide phases of the families $(\text{Cu,Ag,Au,Ni})\text{XO}_2$ and CuXOS . We found 93 thermodynamically stable or quasi-stable (within 20 meV) compositions, out of which only 40 are included in available databases. By calculating the band gaps and hole effective masses of the new stable compounds that we identified, we could reveal some potential candidates to outperform CuAlO_2 as p -type transparent conductor. These few compounds deserve further consideration, both from an experimental and a theoretical point of view.

Materials Design and Inverse Problem We proposed a new method to design new materials with tailored properties on-the-fly, based on a combination of genetic algorithms and global crystal structure prediction methods. To demonstrate the feasibility of our method, starting from a random starting point, we tried to i) maximize the hardness and ii) maximize at the same time the electronic gap and the hole effective mass. Both cases were extremely successful, with several interesting, unknown materials stemming from the simulations.

Putting everything in perspective, at the time this thesis was written, we used global crystal structure prediction methods for more than 6000 different compounds, which (including metastable structures) sums up to more than 50,000 crystal structures. From these, more than 400 are thermodynamically stable structures ($E_{hull} = 0$), not yet present in any database. This was done in three years, using around 10 million computer hours. An important part of the work done covers also the development of the software to automatize several steps of the workflow. Without this, setting up and running these complex calculations in the also complex supercomputer's environments would not be feasible. Even if 10 million hours seems a large number, it is perfectly compatible with today's computer resources. We think this shows how powerful and efficient our approach is, and how relevant this work is for the materials science community.

Finally, we would like to stress that any pragmatic search for technologically relevant materials should also take into consideration the large databases of materials already existing. Conversely, the novel crystal structures encountered by our global prediction methods can also be incorporated into these databases. We believe that the results presented in this thesis are, above all, a proof of the incredible advances of *ab initio* calculations in the past decades, and a prelude to what this field has to offer in the next ones.

Bibliography

- [1] Bergerhoff, G.; Brown, I. Inorganic Crystal Structure Database. In *Crystallographic Databases*; Allen, F., Ed.; International Union of Crystallography: Chester, 1987.
- [2] Berman, H. M.; Westbrook, J.; Feng, Z.; Gilliland, G.; Bhat, T.; Weissig, H.; Shindyalov, I. N.; Bourne, P. E. The protein data bank. *Nucleic Acids Res.* **2000**, *28*, 235–242.
- [3] Gražulis, S.; Daškevič, A.; Merkys, A.; Chateigner, D.; Lutterotti, L.; Quirós, M.; Serebryanaya, N. R.; Moeck, P.; Downs, R. T.; Le Bail, A. Crystallography Open Database (COD): an open-access collection of crystal structures and platform for world-wide collaboration. *Nucleic Acids Res.* **2012**, *40*, 420–427.
- [4] Jain, A.; Ong, S. P.; Hautier, G.; Chen, W.; Richards, W. D.; Dacek, S.; Cholia, S.; Gunter, D.; Skinner, D.; Ceder, G. Commentary: The Materials Project: A materials genome approach to accelerating materials innovation. *APL Mater.* **2013**, *1*, 011002.
- [5] Saal, J.; Kirklin, S.; Aykol, M.; Meredig, B.; Wolverton, C. Materials Design and Discovery with High-Throughput Density Functional Theory: The Open Quantum Materials Database (OQMD). *JOM* **2013**, *65*, 1501–1509.
- [6] Curtarolo, S.; Setyawan, W.; Wang, S.; Xue, J.; Yang, K.; Taylor, R. H.; Nelson, L. J.; Hart, G. L.; Sanvito, S.; Buongiorno-Nardelli, M.; Mingo, N.; Levy, O. AFLOWLIB.ORG: A distributed materials properties repository from high-throughput ab initio calculations. *Comp. Mater. Sci.* **2012**, *58*, 227 – 235.
- [7] Ceder, G. Opportunities and challenges for first-principles materials design and applications to Li battery materials. *MRS Bull.* **2010**, *35*, 693–701.
- [8] Chen, H.; Hautier, G.; Jain, A.; Moore, C.; Kang, B.; Doe, R.; Wu, L.; Zhu, Y.; Tang, Y.; Ceder, G. Carbonophosphates: A New Family of Cathode Materials for Li-Ion Batteries Identified Computationally. *Chem. Mater.* **2012**, *24*, 2009–2016.
- [9] Wang, S.; Wang, Z.; Setyawan, W.; Mingo, N.; Curtarolo, S. Assessing the Thermoelectric Properties of Sintered Compounds via High-Throughput Ab-Initio Calculations. *Phys. Rev. X* **2011**, *1*, 021012.
- [10] Opahle, I.; Parma, A.; McEniry, E. J.; Drautz, R.; Madsen, G. K. H. High-throughput study of the structural stability and thermoelectric properties of transition metal silicides. *New J. Phys.* **2013**, *15*, 105010.

- [11] Carrete, J.; Mingo, N.; Wang, S.; Curtarolo, S. Nanograined Half-Heusler Semiconductors as Advanced Thermoelectrics: An Ab Initio High-Throughput Statistical Study. *Adv. Funct. Mater.* **2014**, 7427–7432.
- [12] Yu, L.; Zunger, A. Identification of Potential Photovoltaic Absorbers Based on First-Principles Spectroscopic Screening of Materials. *Phys. Rev. Lett.* **2012**, 108, 068701.
- [13] Yu, L.; Kokenyesi, R. S.; Keszler, D. A.; Zunger, A. Inverse Design of High Absorption Thin-Film Photovoltaic Materials. *Adv. Energy Mater.* **2013**, 3, 43–48.
- [14] Hautier, G.; Miglio, A.; Ceder, G.; Rignanese, G.-M.; Gonze, X. Identification and design principles of low hole effective mass p-type transparent conducting oxides. *Nat. Commun.* **2013**, 4.
- [15] Hautier, G.; Miglio, A.; Waroquiers, D.; Rignanese, G.-M.; Gonze, X. How does chemistry influence electron effective mass in oxides? A high-throughput computational analysis. *Chem. Mater.* **2014**, 26, 5447–5458.
- [16] Goedecker, S. Minima hopping: An efficient search method for the global minimum of the potential energy surface of complex molecular systems. *J. Chem. Phys.* **2004**, 120, 9911–9917.
- [17] Amsler, M.; Goedecker, S. Crystal structure prediction using the minima hopping method. *J. Chem. Phys.* **2010**, 133, 224104.
- [18] Fiolhais, C.; Nogueira, F.; Marques, M. *A Primer in density functional theory*; Springer: Berlin, 2003.
- [19] Parr, R. G.; Weitao, Y. *Density-Functional Theory of Atoms and Molecules*; Oxford University Press, USA, 1994.
- [20] Cerqueira, T. F. T.; Botti, S.; San-Miguel, A.; Marques, M. A. Density-functional tight-binding study of the collapse of carbon nanotubes under hydrostatic pressure. *Carbon* **2014**, 69, 355–360.
- [21] Cerqueira, T. F. T.; Lin, S.; Amsler, M.; Goedecker, S.; Botti, S.; Marques, M. A. Identification of novel Cu, Ag, and Au ternary oxides from global structural prediction. *Chem. Mater.* **2015**, 27, 4562–4573.
- [22] Cerqueira, T. F. T.; Sarmiento-Pérez, R.; Amsler, M.; Nogueira, F.; Botti, S.; Marques, M. A. Materials design on-the-fly. *J. Chem. Theory Comput.* **2015**, 11, 3955–3960.
- [23] Bowler, D.; Miyazaki, T. Calculations for millions of atoms with density functional theory: linear scaling shows its potential. *J. Phys.: Condens. Matter* **2010**, 22, 074207.
- [24] Born, M.; Oppenheimer, R. Zur quantentheorie der molekeln. *Ann. Phys.* **1927**, 389, 457–484.
- [25] Thomas, L. H. The calculation of atomic fields. *Math. Proc. Cambridge.* **1927**, 23, 542–548.

- [26] Fermi, E. Un metodo statistico per la determinazione di alcune prioriet  dell'atome. *Rend. Accad. Naz. Lincei* **1927**, *6*, 32.
- [27] Hohenberg, P.; Kohn, W. Inhomogeneous electron gas. *Phys. Rev.* **1964**, *136*, B864.
- [28] Kohn, W.; Sham, L. J. Self-consistent equations including exchange and correlation effects. *Phys. Rev.* **1965**, *140*, A1133.
- [29] Porezag, D.; Frauenheim, T.; K hler, T.; Seifert, G.; Kaschner, R. Construction of tight-binding-like potentials on the basis of density-functional theory: Application to carbon. *Phys. Rev. B* **1995**, *51*, 12947.
- [30] Seifert, G.; Porezag, D.; Frauenheim, T. Calculations of molecules, clusters, and solids with a simplified LCAO-DFT-LDA scheme. *Int. J. Quantum Chem.* **1996**, *58*, 185–192.
- [31] Elstner, M.; Porezag, D.; Jungnickel, G.; Elsner, J.; Haugk, M.; Frauenheim, T.; Suhai, S.; Seifert, G. Self-consistent-charge density-functional tight-binding method for simulations of complex materials properties. *Phys. Rev. B* **1998**, *58*, 7260.
- [32] Koskinen, P.; M kinen, V. Density-functional tight-binding for beginners. *Comp. Mater. Sci.* **2009**, *47*, 237–253.
- [33] Fujimura, K.; Seko, A.; Koyama, Y.; Kuwabara, A.; Kishida, I.; Shitara, K.; Fisher, C. A.; Moriwake, H.; Tanaka, I. Accelerated Materials Design of Lithium Superionic Conductors Based on First-Principles Calculations and Machine Learning Algorithms. *Adv. Energy Mater.* **2013**, *3*, 980–985.
- [34] Curtarolo, S.; Hart, G. L. W.; Nardelli, M. B.; Mingo, N.; Sanvito, S.; Levy, O. The high-throughput highway to computational materials design. *Nat. Mater.* **2013**, *12*, 191–201.
- [35] Carrete, J.; Li, W.; Mingo, N.; Wang, S.; Curtarolo, S. Finding Unprecedentedly Low-Thermal-Conductivity Half-Heusler Semiconductors via High-Throughput Materials Modeling. *Phys. Rev. X* **2014**, *4*, 011019.
- [36] Oganov, A. R., Ed. *Modern Methods of Crystal Structure Prediction*; Wiley-VCH: Berlin, 2010.
- [37] Woodley, S. M.; Catlow, R. Crystal structure prediction from first principles. *Nat. Mater.* **2008**, *7*, 937–946.
- [38] Zurek, E.; Grochala, W. Predicting crystal structures and properties of matter under extreme conditions via quantum mechanics: the pressure is on. *Phys. Chem. Chem. Phys.* **2015**, *17*, 2917–2934.
- [39] Kresse, G.; Furthm ller, J. Efficiency of ab-initio total energy calculations for metals and semiconductors using a plane-wave basis set. *Comput. Mater. Sci.* **1996**, *6*, 15 – 50.
- [40] Kresse, G.; Furthm ller, J. Efficient iterative schemes for *ab initio* total-energy calculations using a plane-wave basis set. *Phys. Rev. B* **1996**, *54*, 11169–11186.

- [41] Kirkpatrick, S.; Gelatt, C. D.; Vecchi, M. P. Optimization by simulated annealing. *Science* **1983**, *220*, 671–680.
- [42] Hartke, B. Application of evolutionary algorithms to global cluster geometry optimization. In *Applications of Evolutionary Computation in Chemistry*; Springer, 2004; pp 33–53.
- [43] Wang, Y.; Lv, J.; Zhu, L.; Ma, Y. Crystal structure prediction via particle-swarm optimization. *Phys. Rev. B* **2010**, *82*, 094116.
- [44] Roy, S.; Goedecker, S.; Hellmann, V. Bell-Evans-Polanyi principle for molecular dynamics trajectories and its implications for global optimization. *Phys. Rev. E* **2008**, *77*, 056707.
- [45] Amsler, M.; Flores-Livas, J. A.; Lehtovaara, L.; Balima, F.; Ghasemi, S. A.; Machon, D.; Pailhès, S.; Willand, A.; Caliste, D.; Botti, S.; San Miguel, A.; Goedecker, S.; Marques, M. A. L. Crystal Structure of Cold Compressed Graphite. *Phys. Rev. Lett.* **2012**, *108*, 065501.
- [46] Huan, T. D.; Amsler, M.; Marques, M. A. L.; Botti, S.; Willand, A.; Goedecker, S. Low-Energy Polymeric Phases of Alanates. *Phys. Rev. Lett.* **2013**, *110*, 135502.
- [47] Amsler, M.; Botti, S.; Marques, M. A. L.; Goedecker, S. Conducting Boron Sheets Formed by the Reconstruction of the α -Boron (111) Surface. *Phys. Rev. Lett.* **2013**, *111*, 136101.
- [48] Cerqueira, T. F. T.; Sarmiento-Pérez, R.; Trani, F.; Amsler, M.; Goedecker, S.; Marques, M.; Botti, S. The crystal structure of p-type transparent conductive oxide CuBO_2 . *MRS Commun.* **2013**, *3*, 157–160.
- [49] Flores-Livas, J. A.; Amsler, M.; Lenosky, T. J.; Lehtovaara, L.; Botti, S.; Marques, M. A. L.; Goedecker, S. High-Pressure Structures of Disilane and Their Superconducting Properties. *Phys. Rev. Lett.* **2012**, *108*, 117004.
- [50] Sarmiento-Pérez, R.; Cerqueira, T. F. T.; Valencia-Jaime, I.; Amsler, M.; Goedecker, S.; Botti, S.; Marques, M. A. L.; Romero, A. H. Sodium–gold binaries: novel structures for ionic compounds from an ab initio structural search. *New J. Phys.* **2013**, *15*, 115007.
- [51] Sarmiento-Pérez, R.; Cerqueira, T. F. T.; Valencia-Jaime, I.; Amsler, M.; Goedecker, S.; Romero, A. H.; Botti, S.; Marques, M. A. Novel phases of lithium–aluminum binaries from first-principles structural search. *J. Chem. Phys.* **2015**, *142*, 024710.
- [52] Valencia-Jaime, I.; Sarmiento-Pérez, R.; Botti, S.; Marques, M. A.; Amsler, M.; Goedecker, S.; Romero, A. H. Novel crystal structures for lithium–silicon alloy predicted by minima hopping method. *J. Alloy. Compd.* **2016**, *655*, 147–154.
- [53] Iijima, S. Helical microtubules of graphitic carbon. *Nature* **1991**, *354*, 56–58.
- [54] Chopra, N. G.; Benedict, L. X.; Crespi, V. H.; Cohen, M. L.; Louie, S. G.; Zettl, A. Fully collapsed carbon nanotubes. *Nature* **1995**, *377*, 135–138.

- [55] Motta, M.; Moisala, A.; Kinloch, I. A.; Windle, A. H. High Performance Fibres from "Dog Bone" Carbon Nanotubes. *Adv. Mater.* **2007**, *19*, 3721–3726.
- [56] Chen, D.; Sasaki, T.; Tang, J.; Qin, L.-C. Effects of deformation on the electronic structure of a single-walled carbon nanotube bundle. *Phys. Rev. B* **2008**, *77*, 125412.
- [57] Nishidate, K.; Hasegawa, M. Universal band gap modulation by radial deformation in semiconductor single-walled carbon nanotubes. *Phys. Rev. B* **2008**, *78*, 195403.
- [58] Nishidate, K.; Hasegawa, M. Deformation and transfer doping of a single-walled carbon nanotube adsorbed on metallic substrates. *Phys. Rev. B* **2010**, *81*, 125414.
- [59] Elliott, J. A.; Sandler, J. K. W.; Windle, A. H.; Young, R. J.; Shaffer, M. S. P. Collapse of Single-Wall Carbon Nanotubes is Diameter Dependent. *Phys. Rev. Lett.* **2004**, *92*, 095501.
- [60] Pugno, N. M.; Elliott, J. A. Buckling of peapods, fullerenes and nanotubes. *Phys. E* **2012**, *44*, 944–948.
- [61] Gadagkar, V.; Maiti, P. K.; Lansac, Y.; Jagota, A.; Sood, A. K. Collapse of double-walled carbon nanotube bundles under hydrostatic pressure. *Phys. Rev. B* **2006**, *73*, 085402.
- [62] Yang, X.; Wu, G.; Dong, J. Structural transformations of double-walled carbon nanotube bundle under hydrostatic pressure. *Appl. Phys. Lett.* **2006**, *89*, 113101.
- [63] Sun, D. Y.; Shu, D. J.; Ji, M.; Liu, F.; Wang, M.; Gong, X. G. Pressure-induced hard-to-soft transition of a single carbon nanotube. *Phys. Rev. B* **2004**, *70*, 165417.
- [64] Capaz, R. B.; Spataru, C. D.; Tangney, P.; Cohen, M. L.; Louie, S. G. Hydrostatic pressure effects on the structural and electronic properties of carbon nanotubes. *Phys. Status Solidi B* **2004**, *241*, 3085–3085.
- [65] Merlen, A.; Toulemonde, P.; Bendiab, N.; Aouizerat, A.; Sauvajol, J. L.; Montagnac, G.; Cardon, H.; Petit, P.; San Miguel, A. Raman spectroscopy of open-ended Single Wall Carbon Nanotubes under pressure: effect of the pressure transmitting medium. *Phys. Status Solidi B* **2006**, *243*, 690–699.
- [66] Torres-Dias, A. C.; Cambré, S.; Wenseleers, W.; Machon, D.; San-Miguel, A. Chirality-dependent mechanical response of empty and water-filled single-wall carbon nanotubes at high pressure. *Carbon* **2015**, *95*, 442–451.
- [67] Caillier, C.; Machon, D.; San-Miguel, A.; Arenal, R.; Montagnac, G.; Cardon, H.; Kalbac, M.; Zukalova, M.; Kavan, L. Probing high-pressure properties of single-wall carbon nanotubes through fullerene encapsulation. *Phys. Rev. B* **2008**, *77*, 125418.
- [68] Anis, B.; Börrnert, F.; Rummeli, M.; Kuntscher, C. High-Pressure Optical Microspectroscopy Study on Single-Walled Carbon Nanotubes Encapsulating C₆₀. *J. Phys. Chem. C* **2013**, *117*, 21995–22001.

- [69] Aguiar, A.; Barros, E.; Capaz, R.; Souza Filho, A.; Freire, P.; Filho, J. M.; Machon, D.; Caillier, C.; Kim, Y.; Muramatsu, H. Pressure-induced collapse in double-walled carbon nanotubes: chemical and mechanical screening effects. *J. Phys. Chem. C* **2011**, *115*, 5378–5384.
- [70] Shanavas, K. V.; Sharma, S. M. Molecular dynamics simulations of phase transitions in argon-filled single-walled carbon nanotube bundles under high pressure. *Phys. Rev. B* **2009**, *79*, 155425.
- [71] Ling, C.-C.; Xue, Q.-Z.; Chu, L.-Y.; Jing, N.-N.; Zhou, X.-Y. Radial collapse of carbon nanotubes without and with Stone-Wales defects under hydrostatic pressure. *RSC Adv.* **2012**, *2*, 12182–12189.
- [72] Venkateswaran, U. D.; Rao, A. M.; Richter, E.; Menon, M.; Rinzler, A.; Smalley, R. E.; Eklund, P. C. Probing the single-wall carbon nanotube bundle: Raman scattering under high pressure. *Phys. Rev. B* **1999**, *59*, 10928–10934.
- [73] Peters, M. J.; McNeil, L. E.; Lu, J. P.; Kahn, D. Structural phase transition in carbon nanotube bundles under pressure. *Phys. Rev. B* **2000**, *61*, 5939–5944.
- [74] Yao, M.; Wang, Z.; Liu, B.; Zou, Y.; Yu, S.; Lin, W.; Hou, Y.; Pan, S.; Jin, M.; Zou, B.; Cui, T.; Zou, G.; Sundqvist, B. Raman signature to identify the structural transition of single-wall carbon nanotubes under high pressure. *Phys. Rev. B* **2008**, *78*, 205411.
- [75] Sood, A. K.; Teredesai, P. V.; Muthu, D. V. S.; Sen, R.; Govindaraj, A.; Rao, C. N. R. Pressure Behaviour of Single Wall Carbon Nanotube Bundles and Fullerenes: A Raman Study. *Phys. Status Solidi B* **1999**, *215*, 393–401.
- [76] Sandler, J.; Shaffer, M. S. P.; Windle, A. H.; Halsall, M. P.; Montes-Morán, M. A.; Cooper, C. A.; Young, R. J. Variations in the Raman peak shift as a function of hydrostatic pressure for various carbon nanostructures: A simple geometric effect. *Phys. Rev. B* **2003**, *67*, 035417.
- [77] Merlen, A.; Bendiab, N.; Toulemonde, P.; Aouizerat, A.; San Miguel, A.; Sauvajol, J. L.; Montagnac, G.; Cardon, H.; Petit, P. Resonant Raman spectroscopy of single-wall carbon nanotubes under pressure. *Phys. Rev. B* **2005**, *72*, 035409.
- [78] Ghandour, A. J.; Dunstan, D. J.; Sapelkin, A.; Proctor, J. E.; Halsall, M. P. High-pressure Raman response of single-walled carbon nanotubes: Effect of the excitation laser energy. *Phys. Rev. B* **2008**, *78*, 125420.
- [79] Ghandour, A. J.; Dunstan, D. J.; Sapelkin, A. G-mode behaviour of closed ended single wall carbon nanotubes under pressure. *Phys. Status Solidi B* **2009**, *246*, 491–495.
- [80] Kawasaki, S.; Matsuoka, Y.; Yokomae, T.; Nojima, Y.; Okino, F.; Touhara, H.; Kataura, H. Effect of a liquid pressure-transmitting medium on the high pressure behavior of open- and closed-end single-walled carbon nanotubes and of C₆₀-peapods. *Phys. Status Solidi B* **2004**, *241*, 3512–3516.
- [81] Proctor, J. E.; Halsall, M. P.; Ghandour, A.; Dunstan, D. J. Raman spectroscopy of single-walled carbon nanotubes at high pressure: Effect of interactions between the nanotubes and pressure transmitting media. *Phys. Status Solidi B* **2007**, *244*, 147–150.

- [82] Gao, K.; Dai, R.; Zhao, Z.; Zhang, Z.; Ding, Z. Effects of pressure transmitting media on Raman features of single-walled carbon nanotubes. *Solid State Commun.* **2008**, *147*, 65 – 68.
- [83] Rols, S.; Goncharenko, I. N.; Almairac, R.; Sauvajol, J. L.; Mirebeau, I. Polygonization of single-wall carbon nanotube bundles under high pressure. *Phys. Rev. B* **2001**, *64*, 153401.
- [84] Sharma, S. M.; Karmakar, S.; Sikka, S. K.; Teredesai, P. V.; Sood, A. K.; Govindaraj, A.; Rao, C. N. R. Pressure-induced phase transformation and structural resilience of single-wall carbon nanotube bundles. *Phys. Rev. B* **2001**, *63*, 205417.
- [85] Anis, B.; Haubner, K.; Börrnert, F.; Dunsch, L.; Rummeli, M. H.; Kuntscher, C. A. Stabilization of carbon nanotubes by filling with inner tubes: An optical spectroscopy study on double-walled carbon nanotubes under hydrostatic pressure. *Phys. Rev. B* **2012**, *86*, 155454.
- [86] Zhang, X. H.; Liu, Z. F.; Gong, X. G. Comment on “Collapse of Single-Wall Carbon Nanotubes is Diameter Dependent”. *Phys. Rev. Lett.* **2004**, *93*, 149601.
- [87] Yang, X.; Wu, G.; Zhou, J.; Dong, J. Single-walled carbon nanotube bundle under hydrostatic pressure studied by first-principles calculations. *Phys. Rev. B* **2006**, *73*, 235403.
- [88] Elliott, J. A.; Sandler, J. K. W.; Windle, A. H.; Young, R. J.; Shaffer, M. S. P. Elliott *et al.* Reply. *Phys. Rev. Lett.* **2004**, *93*, 149602.
- [89] Saxena, S.; Tyson, T. A. Interacting Quasi-Two-Dimensional Sheets of Interlinked Carbon Nanotubes: A High-Pressure Phase of Carbon. *ACS Nano* **2010**, *4*, 3515–3521.
- [90] Yang, W.; Wang, R.; Song, X.; Wang, B.; Yan, H. Pressure-induced Raman-active radial breathing mode transition in single-wall carbon nanotubes. *Phys. Rev. B* **2007**, *75*, 045425.
- [91] Imtani, A. N.; Jindal, V. Structure of armchair single-wall carbon nanotubes under hydrostatic pressure. *Phys. Rev. B* **2007**, *76*, 195447.
- [92] Tangney, P.; Capaz, R. B.; Spataru, C. D.; Cohen, M. L.; Louie, S. G. Structural transformations of carbon nanotubes under hydrostatic pressure. *Nano Lett.* **2005**, *5*, 2268–2273.
- [93] Sluiter, M. H.; Kawazoe, Y. Phase diagram of single-wall carbon nanotube crystals under hydrostatic pressure. *Phys. Rev. B* **2004**, *69*, 224111.
- [94] Liu, J.; Zheng, Q.-S.; Wang, L.-F.; Jiang, Q. Mechanical properties of single-walled carbon nanotube bundles as bulk materials. *J. Mech. Phys. Solids* **2005**, *53*, 123–142.
- [95] Yang, W.; Wang, R.-Z.; Wang, Y.-F.; Song, X.-M.; Wang, B.; Yan, H. Anomalous pressure behavior of tangential modes in single-wall carbon nanotubes. *Phys. Rev. B* **2007**, *76*, 033402.

- [96] Zheng, G.; Irle, S.; Morokuma, K. Performance of the DFTB method in comparison to DFT and semiempirical methods for geometries and energies of C₂₀-C₆₀ fullerene isomers. *Chem. Phys. Lett.* **2005**, *412*, 210 – 216.
- [97] Malola, S.; Häkkinen, H.; Koskinen, P. Raman spectra of single-walled carbon nanotubes with vacancies. *Phys. Rev. B* **2008**, *77*, 155412.
- [98] Botti, S.; Amsler, M.; Flores-Livas, J. A.; Ceria, P.; Goedecker, S.; Marques, M. A. L. Carbon structures and defect planes in diamond at high pressure. *Phys. Rev. B* **2013**, *88*, 014102.
- [99] Aradi, B.; Hourahine, B.; Frauenheim, T. DFTB+, a Sparse Matrix-Based Implementation of the DFTB Method. *J. Phys. Chem. A* **2007**, *111*, 5678–5684.
- [100] Frenzel, J.; Oliveira, A. F.; Jardillier, N.; Heine, T.; Seifert, G. Semi-relativistic, self-consistent charge Slater-Koster tables for density-functional based tight-binding (DFTB) for materials science simulations. 2004–2009.
- [101] ShklyaeV, O. E.; Mockensturm, E.; Crespi, V. H. Modeling Electrostatically Induced Collapse Transitions in Carbon Nanotubes. *Phys. Rev. Lett.* **2011**, *106*, 155501.
- [102] Thess, A.; Lee, R.; Nikolaev, P.; Dai, H.; Petit, P.; Robert, J.; Xu, C.; Lee, Y. H.; Kim, S. G.; Rinzler, A. G.; Colbert, D. T.; Scuseria, G. E.; Tománek, D.; Fischer, J. E.; Smalley, R. E. Crystalline Ropes of Metallic Carbon Nanotubes. *Science* **1996**, *273*, 483–487.
- [103] Lu, S.; Yao, M.; Li, Q.; Lv, H.; Liu, D.; Liu, B.; Liu, R.; Jiang, L.; Yao, Z.; Liu, Z.; Zou, B.; Cui, T.; Liu, B. Exploring the possible interlinked structures in single-wall carbon nanotubes under pressure by Raman spectroscopy. *J. Raman Spectrosc.* **2013**, *44*, 176–182.
- [104] Cheng, H.; Pez, G. P.; Cooper, A. C. Spontaneous Cross Linking of Small-Diameter Single-Walled Carbon Nanotubes. *Nano Lett.* **2003**, *3*, 585–587.
- [105] Reich, S.; Thomsen, C.; Ordejón, P. Elastic properties and pressure-induced phase transitions of single-walled carbon nanotubes. *Phys. Status Solidi B* **2003**, *235*, 354–359.
- [106] López, M. J.; Rubio, A.; Alonso, J. A.; Qin, L.-C.; Iijima, S. Novel Polygonized Single-Wall Carbon Nanotube Bundles. *Phys. Rev. Lett.* **2001**, *86*, 3056–3059.
- [107] Zang, J.; Treibergs, A.; Han, Y.; Liu, F. Geometric Constant Defining Shape Transitions of Carbon Nanotubes under Pressure. *Phys. Rev. Lett.* **2004**, *92*, 105501.
- [108] Zhong, X. H.; Wang, R.; Liu, L. B.; Kang, M.; Wen, Y. Y.; Hou, F.; Feng, J. M.; Li, Y. L. Structures and characterizations of bundles of collapsed double-walled carbon nanotubes. *Nanotechnology* **2012**, *23*, 505712.
- [109] Lebedkin, S.; Arnold, K.; Kiowski, O.; Hennrich, F.; Kappes, M. M. Raman study of individually dispersed single-walled carbon nanotubes under pressure. *Phys. Rev. B* **2006**, *73*, 094109.

- [110] Paineau, E.; Albouy, P.-A.; Rouzière, S.; Orecchini, A.; Rols, S.; Launois, P. X-ray scattering determination of the structure of water during carbon nanotube filling. *Nano Lett.* **2013**, *13*, 1751–1756.
- [111] Kalra, A.; Garde, S.; Hummer, G. Osmotic water transport through carbon nanotube membranes. *Proc. Natl. Acad. Sci.* **2003**, *100*, 10175–10180.
- [112] Zangi, R.; Mark, A. E. Monolayer ice. *Phys. Rev. Lett.* **2003**, *91*, 025502.
- [113] Maniwa, Y.; Kataura, H.; Abe, M.; Udaka, A.; Suzuki, S.; Achiba, Y.; Kira, H.; Matsuda, K.; Kadowaki, H.; Okabe, Y. Ordered water inside carbon nanotubes: formation of pentagonal to octagonal ice-nanotubes. *Chem. Phys. Lett.* **2005**, *401*, 534–538.
- [114] Takaiwa, D.; Hatano, I.; Koga, K.; Tanaka, H. Phase diagram of water in carbon nanotubes. *Proc. Natl. Acad. Sci.* **2008**, *105*, 39–43.
- [115] Giovambattista, N.; Rossky, P. J.; Debenedetti, P. G. Phase transitions induced by nanoconfinement in liquid water. *Phys. Rev. Lett.* **2009**, *102*, 050603.
- [116] Han, S.; Choi, M.; Kumar, P.; Stanley, H. E. Phase transitions in confined water nanofilms. *Nat. Phys.* **2010**, *6*, 685–689.
- [117] Bai, J.; Zeng, X. C. Polymorphism and polyamorphism in bilayer water confined to slit nanopore under high pressure. *Proc. Natl. Acad. Sci.* **2012**, *109*, 21240–21245.
- [118] Nair, R.; Wu, H.; Jayaram, P.; Grigorieva, I.; Geim, A. Unimpeded permeation of water through helium-leak-tight graphene-based membranes. *Science* **2012**, *335*, 442–444.
- [119] Algara-Siller, G.; Lehtinen, O.; Wang, F.; Nair, R.; Kaiser, U.; Wu, H.; Geim, A.; Grigorieva, I. Square ice in graphene nanocapillaries. *Nature* **2015**, *519*, 443–445.
- [120] O’Keeffe, M.; Adams, G. B.; Sankey, O. F. Duals of Frank-Kasper structures as C, Si and Ge clathrates: Energetics and structure. *Philos. Mag. Lett.* **1998**, *1*, 21–28.
- [121] Kuo, K. H. From Frank-Kasper phases to the icosahedral quasicrystal. *J. Phys. Colloques* **1986**, *47*, 425–436.
- [122] Cros, C.; Pouchard, M.; Hagenmuller, P. *C. R. Acad. Sci. Paris* **1965**, *260*, 4764.
- [123] Kasper, J. S.; Hagenmuller, P.; Pouchard, M.; Cros, C. Clathrate Structure of Silicon $\text{Na}_8\text{Si}_{46}$ and $\text{Na}_x\text{Si}_{136}$ ($x < 11$). *Science* **1965**, *150*, 1713–1714.
- [124] Nolas, G. S. *The Physics and Chemistry of Inorganic Clathrates*; Springer, 2014; Vol. 199.
- [125] Fässler, T. F., Ed. Quantitative Advances in the Zintl-Klemm Formalism. In *Zintl phases*; Struct. Bond.; Springer Berlin Heidelberg, 2011; Vol. 139; pp 1–55.
- [126] Schafer, H. On the Problem of Polar Intermetallic Compounds: the Stimulation of E. Zintl’s Work for the Modern Chemistry of Intermetallics. *Annu. Rev. Mater. Res.* **1985**, *15*, 1–41.

- [127] Shevelkov, A. V.; Kovnir, K. Zintl Clathrates. In *Zintl Phases*; Fässler, T. F., Ed.; Struct. Bond.; Springer Berlin Heidelberg, 2011; Vol. 139; pp 97–142.
- [128] Karttunen, A. J.; Fässler, T. F.; Linnolahti, M.; Pakkanen, T. A. Structural Principles of Semiconducting Group 14 Clathrate Frameworks. *Inorg. Chem.* **2011**, *50*, 1733–1742.
- [129] Toberer, E. S.; May, A. F.; Snyder, G. J. Zintl Chemistry for Designing High Efficiency Thermoelectric Materials. *Chem. Mater.* **2009**, *22*, 624–634.
- [130] Yamanaka, S. Silicon clathrates and carbon analogs: high pressure synthesis, structure, and superconductivity. *Dalton Trans.* **2010**, *39*, 1901–1915.
- [131] Shi, X.; Yang, J.; Bai, S.; Yang, J.; Wang, H.; Chi, M.; Salvador, J. R.; Zhang, W.; Chen, L.; Wong-Ng, W. On the Design of High-Efficiency Thermoelectric Clathrates through a Systematic Cross-Substitution of Framework Elements. *Adv. Funct. Mater.* **2010**, *20*, 755–763.
- [132] Pailhès, S.; Euchner, H.; Giordano, V. M.; Debord, R.; Assy, A.; Gomès, S.; Bosak, A.; Machon, D.; Paschen, S.; de Boissieu, M. Localization of Propagative Phonons in a Perfectly Crystalline Solid. *Phys. Rev. Lett.* **2014**, *113*, 025506.
- [133] Euchner, H.; Pailhès, S.; Nguyen, L. T. K.; Assmus, W.; Ritter, F.; Haghighirad, A.; Grin, Y.; Paschen, S.; de Boissieu, M. Phononic filter effect of rattling phonons in the thermoelectric clathrate $\text{Ba}_8\text{Ge}_{40+x}\text{Ni}_{6-x}$. *Phys. Rev. B* **2012**, *86*, 224303.
- [134] Tadano, T.; Gohda, Y.; Tsuneyuki, S. Impact of Rattlers on Thermal Conductivity of a Thermoelectric Clathrate: A First-Principles Study. *Phys. Rev. Lett.* **2015**, *114*, 095501.
- [135] Takabatake, T.; Suekuni, K. Phonon-glass electron-crystal thermoelectric clathrates: Experiments and theory. *Rev. Mod. Phys.* **2014**, *86*, 669–716.
- [136] Mogens Christensen, S. J.; Iversen, B. B. Thermoelectric clathrates of type I. *Dalton Trans.* **2010**, *39*, 978–992.
- [137] Slack, G. *CRC Handbook of Thermoelectrics*; CRC Press, 1995; Vol. 407.
- [138] Kovnir, K. A.; Shevelkov, A. V. Semiconducting clathrates: synthesis, structure and properties. *Russ. Chem. Rev.* **2004**, *73*, 923.
- [139] Prokofiev, A.; Sidorenko, A.; Hradil, K.; Ikeda, M.; Svagera, R.; Waas, M.; Winkler, H.; Neumaier, K.; Paschen, S. Thermopower enhancement by encapsulating cerium in clathrate cages. *Nat. Mater.* **2013**, *12*, 1096–1101.
- [140] Paschen, S.; Ikeda, M.; Stefanoski, S.; Nolas, G. S. Structural and Physical Properties of Rare-Earth Clathrates. In *The Physics and Chemistry of Inorganic Clathrates*; Springer, 2014; pp 249–276.
- [141] Perdew, J. P.; Burke, K.; Ernzerhof, M. Generalized Gradient Approximation Made Simple. *Phys. Rev. Lett.* **1996**, *77*, 3865–3868.

- [142] Reny, E.; Gravereau, P.; Cros, C.; Pouchard, M. Structural characterisations of the NaSi_{136} and $\text{Na}_8\text{Si}_{46}$ silicon clathrates using the Rietveld method. *J. Mater. Chem.* **1998**, *8*, 2839–2844.
- [143] Ramachandran, G. K.; McMillan, P. F.; Dong, J.; Sankey, O. F. $\text{K}_{7.62(1)}\text{Si}_{46}$ and $\text{Rb}_{6.15(2)}\text{Si}_{46}$: Two Structure I Clathrates with Fully Occupied Framework Sites. *J. Solid State Chem.* **2000**, *154*, 626 – 634.
- [144] Wosylus, A.; Veremchuk, I.; Schnelle, W.; Baitinger, M.; Schwarz, U.; Grin, Y. $\text{Cs}_{8-x}\text{Si}_{46}$: A Type-I Clathrate with Expanded Silicon Framework. *Chem. Eur. J.* **2009**, *15*, 5901–5903.
- [145] Reny, E.; Yamanaka, S.; Cros, C.; Pouchard, M. High pressure synthesis of an iodine doped silicon clathrate compound. *Chem. Commun.* **2000**, *24*, 2505–2506.
- [146] Kirsanova, M. A.; Shevelkov, A. V. Clathrates and semiclathrates of Type-I: crystal structure and superstructures. *Z. Kristallogr. - Cryst. Mater.* **2013**, *228*, 215–227.
- [147] Dong, Y.; Chai, P.; Beekman, M.; Zeng, X.; Tritt, T. M.; Nolas, G. S. Precursor Routes to Complex Ternary Intermetallics: Single-Crystal and Microcrystalline Preparation of Clathrate.I $\text{Na}_8\text{Al}_8\text{Si}_{38}$ from $\text{NaSi} + \text{NaAlSi}$. *Inorg. Chem.* **2015**, *54*, 5316–5321.
- [148] Kraner, R.; Peters, K.; Von Schnering, H. G.; Nesper, R. Crystal structure of the clathrates $\text{K}_8\text{Ga}_8\text{Si}_{38}$ and $\text{K}_8\text{Ga}_8\text{Sn}_{38}$. *Z. Kristallogr.-New Cryst. Struct.* **1998**, *213*, 667.
- [149] Jung, W.; Lörincz, J.; Ramlau, R.; Borrmann, H.; Prots, Y.; Haarmann, F.; Schnelle, W.; Burkhardt, U.; Baitinger, M.; Grin, Y. $\text{K}_7\text{B}_7\text{Si}_{39}$ a Borosilicide with the Clathrate I Structure. *Angew. Chem.* **2007**, *46*, 6725–6728.
- [150] Baran, V.; Senyshyn, A.; Karttunen, A.; Fischer, A.; Scherer, W.; Raudaschl-Sieber, G.; Fässler, T. A Combined Metal/Halide/Metal Flux Synthetic Route towards Type-I Clathrates: Crystal Structures and Thermoelectric Properties of $\text{A}_8\text{Al}_8\text{Si}_{38}$ (A=K, Rb, and Cs). *Chem. Eur. J.* **2014**, *20*, 15077–15088.
- [151] von Schnering, H. G.; Kröner, R.; Menke, H.; Peters, K.; Nesper, R. Crystal structure of the clathrates $\text{Rb}_8\text{Ga}_8\text{Sn}_{38}$, $\text{Rb}_8\text{Ga}_8\text{Ge}_{38}$ and $\text{Rb}_8\text{Ga}_8\text{Si}_{38}$. *Z. Kristallogr.-New Cryst. Struct.* **1998**, *213*, 677.
- [152] Sui, F.; He, H.; Bobev, S.; Zhao, J.; Osterloh, F.; Kauzlarich, S. Synthesis, Structure, Thermoelectric Properties, and Band Gaps of Alkali Metal Containing Type I Clathrates: $\text{A}_8\text{Ga}_8\text{Si}_{38}$ (A = K, Rb, Cs) and $\text{K}_8\text{Al}_8\text{Si}_{38}$. *Chem. Mater.* **2015**,
- [153] Roudebush, J. H.; Tsujii, N.; Hurtando, A.; Hope, H.; Grin, Y.; M. Kauzlarich, S. Phase Range of the Type-I Clathrate $\text{Sr}_8\text{Al}_x\text{Si}_{46-x}$ and Crystal Structure of $\text{Sr}_8\text{Al}_{10}\text{Si}_{36}$. *Inorg. Chem.* **2012**, *51*, 4161–4169.
- [154] Carrillo-Cabrera, W.; Cardoso Gil, R.; Grin, Y. Crystal structure of the clathrate $\text{Sr}_8\text{Ga}_{16-x}\text{Si}_{30+x}$, $x = 2.18, 4.05$. *Z. Kristallogr. - New Cryst. Struct.* **2002**, *217*, 179–180.

- [155] Cordier, G.; Woll, P. Neue ternäre intermetallische Verbindungen mit Clathratstruktur: $\text{Ba}_8(\text{T},\text{Si})_6\text{Si}_{40}$ und $\text{Ba}_6(\text{T},\text{Ge})_6\text{Ge}_{40}$ mit $\text{T} = \text{Ni}, \text{Pd}, \text{Pt}, \text{Cu}, \text{Ag}, \text{Au}$. *J. Less-Common Met.* **1991**, *169*, 291 – 302.
- [156] Aydemir, U.; Candolfi, C.; Ormeci, A.; Borrmann, H.; Burkhardt, U.; Oztan, Y.; Oeschler, N.; Baitinger, M.; Steglich, F.; Grin, Y. Synthesis, Crystal Structure, and Physical Properties of the Type-I Clathrate $\text{Ba}_{8-\delta}\text{Ni}_{x\leq y}\text{Si}_{46-x-y}$. *Inorg. Chem.* **2012**, *51*, 4730–4741.
- [157] Anno, H.; Yamada, H.; Nakabayashi, T.; Hokazono, M.; Shirataki, R. Influence of preparation conditions on thermoelectric properties of $\text{Ba}_8\text{Ga}_{16}\text{Si}_{30}$ clathrate by combining arc melting and spark plasma sintering methods. *J. Phys.: Conf. Ser.* **2011**, *379*, 012007.
- [158] Yan, X.; Chen, M. X.; Laumann, S.; Bauer, E.; Rogl, P.; Podloucky, R.; Paschen, S. Thermoelectric properties of Ba-Cu-Si clathrates. *Phys. Rev. B* **2012**, *85*, 165127.
- [159] Zeiringer, I.; Bauer, E.; Grytsiv, A.; Rogl, P.; Effenberger, H. Phase Equilibria, Crystal Chemistry, and Physical Properties of Ag-Ba-Si Clathrates. *Jpn. J. Appl. Phys.* **2011**, *50*, 05FA01.
- [160] Anno, H.; Hokazono, M.; Shirataki, R.; Nagami, Y. Crystallographic, thermoelectric, and mechanical properties of polycrystalline Type-I $\text{Ba}_8\text{Al}_{16}\text{Si}_{30}$ -based clathrates. *J. Mater. Sci.* **2013**, *48*, 2846–2854.
- [161] Nasir, N.; Grytsiv, A.; Melnychenko-Koblyuk, N.; Rogl, P.; Bauer, E.; Lackner, R.; Royanian, E.; Giester, G.; Saccone, A. Clathrates $\text{Ba}_8\text{Zn}, \text{Cd}_x\text{Si}_{46-x}$, $x \sim 7$: synthesis, crystal structure and thermoelectric properties. *J. Phys.: Condens. Matter* **2009**, *21*, 385404.
- [162] Melnychenko-Koblyuk, N.; Grytsiv, A.; Rogl, P.; Bauer, E.; Lackner, R.; Royanian, E.; Rotter, M.; Giester, G. Structure and Physical Properties of Clathrate I Systems $\text{Ba}_8\text{Pd}_x\text{Si}_{46-x}$ and $\text{Ba}_8\text{Pt}_x\text{Si}_{46-x}$. *J. Phys. Soc. Jpn.* **2008**, *77*, 54–60.
- [163] Candolfi, C.; Aydemir, U.; Baitinger, M.; Oeschler, N.; Steglich, F.; Grin, Y. High temperature thermoelectric properties of the Type-I clathrate $\text{Ba}_8\text{Au}_x\text{Si}_{46-x}$. *J. Appl. Phys.* **2012**, *111*, 043706.
- [164] Jung, W.; Kessens, H.; Ormeci, A.; Schnelle, W.; Burkhardt, U.; Borrmann, H.; Nguyen, H. D.; Baitinger, M.; Grin, Y. Synthesis, crystal structure and physical properties of the clathrate-I phase $\text{Ba}_8\text{Rh}_x\text{Si}_{46-x-y\leq y}$. *Dalton Trans.* **2012**, *41*, 13960–13968.
- [165] Falmbigl, M.; Grytsiv, A.; Rogl, P.; Giester, G. Clathrate formation in the systems Ba–Ir–Ge and Ba–{Rh, Ir}–Si: Crystal chemistry and phase relations. *Intermetallics*. **2013**, *36*, 61–72.
- [166] Hautier, G.; Fischer, C. C.; Jain, A.; Mueller, T.; Ceder, G. Finding Nature’s Missing Ternary Oxide Compounds Using Machine Learning and Density Functional Theory. *Chem. Mater.* **2010**, *22*, 3762–3767.

- [167] Kawazoe, H.; Yasukawa, M.; Hyodo, H.; Kurita, M.; Yanagi, H.; Hosono, H. P-type electrical conduction in transparent thin films of CuAlO_2 . *Nature* **1997**, *389*, 939.
- [168] Yanagi, H.; Hase, T.; Ibuki, S.; Ueda, K.; Hosono, H. Bipolarity in electrical conduction of transparent oxide semiconductor CuInO_2 with delafossite structure. *Appl. Phys. Lett.* **2001**, *78*, 1583–1585.
- [169] Yanagi, H.; Ueda, K.; Ohta, H.; Orita, M.; Hirano, M.; Hosono, H. Fabrication of all oxide transparent p-n homojunction using bipolar CuInO_2 semiconducting oxide with delafossite structure. *Solid State Comm.* **2002**, *121*, 15–17.
- [170] Ueda, K.; Hase, T.; Yanagi, H.; Kawazoe, H.; Hosono, H.; Ohta, H.; Orita, M.; Hirano, M. Epitaxial growth of transparent p-type conducting CuGaO_2 thin films on sapphire (001) substrates by pulsed laser deposition. *J. Appl. Phys.* **2001**, *89*, 1790–1793.
- [171] Ueda, K.; Inoue, S.; Hirose, S.; Kawazoe, H.; Hosono, H. Transparent p-type semiconductor: LaCuOS layered oxysulfide. *Appl. Phys. Lett.* **2000**, *77*, 2701–2703.
- [172] Yanagi, H.; Inoue, S.; Ueda, K.; Kawazoe, H.; Hosono, H.; Hamada, N. Electronic structure and optoelectronic properties of transparent p-type conducting CuAlO_2 . *J. Appl. Phys.* **2000**, *88*, 4159–4163.
- [173] Scanlon, D. O.; Watson, G. W. $(\text{Cu}_2\text{S}_2)(\text{Sr}_3\text{Sc}_2\text{O}_5)$ - A Layered, Direct Band Gap, p-Type Transparent Conducting Oxychalcogenide: A Theoretical Analysis. *Chem. Mater.* **2009**, *21*, 5435–5442.
- [174] Scanlon, D. O.; Buckeridge, J.; Catlow, C. R. A.; Watson, G. W. Understanding doping anomalies in degenerate p-type semiconductor LaCuOSe . *J. Mater. Chem. C* **2014**, *2*, 3429–3438.
- [175] Nagarajan, R.; Duan, N.; Jayaraj, M.; Li, J.; Vanaja, K.; Yokochi, A.; Draeseke, A.; Tate, J.; Sleight, A. p-Type conductivity in the delafossite structure. *Int. J. Inorg. Mater.* **2001**, *3*, 265 – 270.
- [176] Sheng, S.; Fang, G.; Li, C.; Xu, S.; Zhao, X. p-type transparent conducting oxides. *Phys. Status Solidi A* **2006**, *203*, 1891–1900.
- [177] Nagarajan, R.; Draeseke, A. D.; Sleight, A. W.; Tate, J. p-type conductivity in $\text{CuCr}_{1-x}\text{Mg}_x\text{O}_2$ films and powders. *J. Appl. Phys.* **2001**, *89*, 8022–8025.
- [178] Kudo, A.; Yanagi, H.; Hosono, H.; Kawazoe, H. SrCu_2O_2 : A p-type conductive oxide with wide band gap. *Appl. Phys. Lett.* **1998**, *73*, 220–222.
- [179] Blöchl, P. Projector augmented-wave method. *Phys. Rev. B* **1994**, *50*, 17953.
- [180] Anisimov, V. I.; Zaanen, J.; Andersen, O. *Phys. Rev. B* **1991**, *44*, 943.
- [181] Heinemann, M.; Eifert, B.; Heiliger, C. Band structure and phase stability of the copper oxides Cu_2O , CuO , and Cu_4O_3 . *Phys. Rev. B* **2013**, *87*, 115111.

- [182] Ong, S. P.; Richards, W. D.; Jain, A.; Hautier, G.; Kocher, M.; Cholia, S.; Gunter, D.; Chevrier, V. L.; Persson, K. A.; Ceder, G. Python Materials Genomics (pymatgen): A robust, open-source python library for materials analysis. *Comp. Mater. Sci.* **2013**, *68*, 314 – 319.
- [183] Stokes, H. T.; Hatch, D. M. *FINDSYM*: program for identifying the space-group symmetry of a crystal. *J. Appl. Crystallogr.* **2005**, *38*, 237–238.
- [184] Hewston, T. A.; Chamberland, B. A survey of first-row ternary oxides LiMO_2 (M= Sc-Cu). *J. Phys. Chem. Solids.* **1987**, *48*, 97–108.
- [185] Madsen, G. K.; Singh, D. J. BoltzTraP. A code for calculating band-structure dependent quantities. *Comput. Phys. Commun.* **2006**, *175*, 67 – 71.
- [186] Vidal, J.; Trani, F.; Bruneval, F.; Marques, M. A. L.; Botti, S. Effects of Electronic and Lattice Polarization on the Band Structure of Delafossite Transparent Conductive Oxides. *Phys. Rev. Lett.* **2010**, *104*, 136401.
- [187] Trani, F.; Vidal, J.; Botti, S.; Marques, M. A. L. Band structures of delafossite transparent conductive oxides from a self-consistent *GW* approach. *Phys. Rev. B* **2010**, *82*, 085115.
- [188] Anatole von Lilienfeld, O. Towards the Computational Design of Compounds from First Principles. In *Many-Electron Approaches in Physics, Chemistry and Mathematics: A Multidisciplinary View*; Delle Site, L., Bach, V., Eds.; Lect. Notes. Phys.; Springer Verlag, 2014.
- [189] Franceschetti, A.; Zunger, A. The inverse band-structure problem of finding an atomic configuration with given electronic properties. *Nature* **1999**, *402*, 60–63.
- [190] Zhang, L.; d’Avezac, M.; Luo, J.-W.; Zunger, A. Genomic design of strong direct-gap optical transition in Si/Ge core/multishell nanowires. *Nano Lett.* **2012**, *12*, 984–991.
- [191] d’Avezac, M.; Luo, J.-W.; Chanier, T.; Zunger, A. Genetic-Algorithm Discovery of a Direct-Gap and Optically Allowed Superstructure from Indirect-Gap Si and Ge Semiconductors. *Phys. Rev. Lett.* **2012**, *108*, 027401.
- [192] Pilania, G.; Wang, C.; Jiang, X.; Rajasekaran, S.; Ramprasad, R. Accelerating materials property predictions using machine learning. *Sci. Rep.* **2013**, *3*.
- [193] von Lilienfeld, O. A.; Lins, R. D.; Rothlisberger, U. Variational Particle Number Approach for Rational Compound Design. *Phys. Rev. Lett.* **2005**, *95*, 153002.
- [194] Wang, M.; Hu, X.; Beratan, D. N.; Yang, W. Designing Molecules by Optimizing Potentials. *J. Am. Chem. Soc.* **2006**, *128*, 3228–3232.
- [195] Keinan, S.; Hu, X.; Beratan, D. N.; Yang, W. Designing Molecules with Optimal Properties Using the Linear Combination of Atomic Potentials Approach in an AM1 Semiempirical Framework. *J. Phys. Chem. A* **2007**, *111*, 176–181.
- [196] Anatole von Lilienfeld, O. Accurate ab initio energy gradients in chemical compound space. *J. Chem. Phys.* **2009**, *131*, 164102.

- [197] Balawender, R.; Welearegay, M. A.; Lesiuk, M.; De Proft, F.; Geerlings, P. Exploring Chemical Space with the Alchemical Derivatives. *J. Chem. Theory Comput.* **2013**, *9*, 5327–5340.
- [198] Lesiuk, M.; Balawender, R.; Zachara, J. Higher order alchemical derivatives from coupled perturbed self-consistent field theory. *J. Chem. Phys.* **2012**, *136*, 034104.
- [199] d’Avezac, M.; Zunger, A. Identifying the minimum-energy atomic configuration on a lattice: Lamarckian twist on Darwinian evolution. *Phys. Rev. B* **2008**, *78*, 064102.
- [200] Niu, H.; Chen, X.-Q.; Ren, W.; Zhu, Q.; Oganov, A. R.; Li, D.; Li, Y. Variable-composition structural optimization and experimental verification of MnB₃ and MnB₄. *Phys. Chem. Chem. Phys.* **2014**, *16*, 15866–15873.
- [201] Deb, K.; Pratap, A.; Agarwal, S.; Meyarivan, T. A Fast Elitist Multi-objective Genetic Algorithm: NSGA-II. *IEEE Trans. Evol. Comput.* **2002**, *6*, 182.
- [202] Zhang, X.; Wang, Y.; Lv, J.; Zhu, C.; Li, Q.; Zhang, M.; Li, Q.; Ma, Y. First-principles structural design of superhard materials. *J. Chem. Phys.* **2013**, *138*, 114101.
- [203] Šimůnek, A.; Vacká, J. Hardness of Covalent and Ionic Crystals: First-Principle Calculations. *Phys. Rev. Lett.* **2006**, *96*, 085501.
- [204] Šimůnek, A. How to estimate hardness of crystals on a pocket calculator. *Phys. Rev. B* **2007**, *75*, 172108.
- [205] Gao, F.; Gao, L. Microscopic models of hardness. *J. Superhard Mater.* **2010**, *32*, 148–166.
- [206] Trinajstić, N.; Babić, D.; Nikolić, S.; Plavšić, D.; Amić, D.; Mihaljčić, Z. The Laplacian matrix in chemistry. *J. Chem. Inf. Comp. Sci.* **1994**, *34*, 368–376.
- [207] Heyd, J.; Scuseria, G. E.; Ernzerhof, M. Hybrid functionals based on a screened Coulomb potential. *J. Chem. Phys.* **2003**, *118*, 8207–8215.
- [208] Liu, A. Y.; Cohen, M. L. Prediction of New Low Compressibility Solids. *Science* **1989**, *245*, 841–842.
- [209] Vepřek, S. The search for novel, superhard materials. *J. Vac. Sci. Technol., A* **1999**, *17*, 2401–2420.
- [210] Solozhenko, V. L.; Andrault, D.; Fiquet, G.; Mezouar, M.; Rubie, D. C. Synthesis of superhard cubic BC₂N. *Appl. Phys. Lett.* **2001**, *78*, 1385–1387.
- [211] Solozhenko, V. L.; Gregoryanz, E. Synthesis of superhard materials. *Mater. Today* **2005**, *8*, 44 – 51.
- [212] Friedrich, A.; Winkler, B.; Juárez-Arellano, E. A.; Bayarjargal, L. Synthesis of Binary Transition Metal Nitrides, Carbides and Borides from the Elements in the Laser-Heated Diamond Anvil Cell and Their Structure-Property Relations. *Materials* **2011**, *4*, 1648–1692.

-
- [213] Levine, J. B.; Tolbert, S. H.; Kaner, R. B. Advancements in the Search for Superhard Ultra-Incompressible Metal Borides. *Adv. Funct. Mater.* **2009**, *19*, 3519–3533.
- [214] Henkelman, G.; Arnaldsson, A.; Jónsson, H. A fast and robust algorithm for Bader decomposition of charge density. *Comp. Mater. Sci.* **2006**, *36*, 354–360.
- [215] O’Keeffe, M. A proposed rigorous definition of coordination number. *Acta Crystallogr., Sect. A: Cryst. Phys., Diffr., Theor. Gen. Crystallogr.* **1979**, *35*, 772–775.
- [216] O’Keeffe, M.; Brese, N. Atom sizes and bond lengths in molecules and crystals. *J. Am. Chem. Soc.* **1991**, *113*, 3226–3229.

Appendix A

Bader charges, oxidation states, and coordination numbers (Chapter 5)

In Tables A.1 and A.2 we summarize values of Bader charges, oxidation states and coordination numbers for the crystal structures with a total energy within 50 meV from the convex hull of stability. These data were calculated using the PYMATGEN package [182]. For Bader charges PYMATGEN uses the algorithm developed by Henkelman *et al.* [214], coordination numbers are extracted from the Voronoi analysis [215], while oxidation states are obtained using a maximum a posteriori estimation method with the element-based parameters of M. O’Keefe *et al.* [216]. Oxidation states for some structures are unfortunately missing due to the lack of adequate parameters for some elements and related problems with the software.

Table A.1 Bader charges (BC), oxidation state (OS) and coordination numbers (CN) for the (Cu,Ag,Au,Ni)XO₂ structures within 50 meV from the convex hull.

Structure	A			B			O		
	BC	OS	CN	BC	OS	CN	BC	OS	CN
CuHO2	1.3	Cu2+	5.3	1.0	H+	3.1	-1.4, -0.9	O2-, O-	3.1, 3.7
CuLiO2	1.2	Cu2+	4.9, 5.2	0.9	Li+	4.9	-1.0, -1.1	O-, O2-	4.9
CuFO2	1.2	Cu3+	4.8	-0.7	F-	5.3	-0.3, -0.2	O-	3.3
CuNaO2	1.2	Cu3+	4.5	0.9	Na+	6.0	-1.0	O2-	4.5
CuMgO2	1.0	Cu2+	5.3	1.8	Mg2+	6.1	-1.3, -1.5	O2-	6.0, 5.3
CuAlO2	0.5	Cu+	4.2	3.0	Al3+	6.0	-1.8, -1.7	O2-	4.2
CuClO2	1.0	Cu3+	4.8	-0.5	Cl-	5.3	-0.2	O-	3.1
CuKO2	1.1	Cu3+	4.3	0.8	K+	6.5	-1.0	O2-	4.3
CuCaO2	1.0	Cu2+	5.2	1.5	Ca2+	9.0	-1.3	O2-	5.2
CuScO2	0.7	Cu+	3.8	2.0	Sc3+	6.0	-1.3	O2-	3.8
CuVO2	0.6	Cu+	4.0	1.9	V3+	6.0, 5.9	-1.2, -1.3	O2-	4.0
CuCrO2	0.6	Cu+	4.0	1.8	Cr3+	6.0	-1.2	O2-	4.0
CuMnO2	0.6	Cu2+	4.0	1.8	Mn2+	5.6	-1.2	O2-	4.0
CuFeO2	0.6	Cu+	4.0	1.8	Fe3+	6.0	-1.2	O2-	4.0
CuCoO2	0.5	Cu2+	4.2	1.4	Co2+	6.0	-1.0	O2-	4.2
CuGaO2	0.6	Cu+	4.1	1.9	Ga3+	6.0	-1.2	O2-	4.1
CuBrO2	0.9	Cu3+	4.6	-0.4	Br-	5.4	-0.3, -0.2	O-	3.1
CuRbO2	1.1	Cu+	4.3	0.9	Rb+	6.7	-1.0	O-	4.3
CuSrO2	1.0	Cu2+	4.7	1.5	Sr2+	5.9	-1.2, -1.4	O2-	4.9, 4.7
CuYO2	0.6	Cu+	3.6	2.2	Y3+	6.1	-1.4	O2-	3.6

Table A.1 (continued)

Structure	A			B			O		
	BC	OS	CN	BC	OS	CN	BC	OS	CN
CuRhO2	0.6	Cu+	3.9	1.3	Rh3+	6.0	-1.0	O2-	3.9
CuPdO2	1.0	Cu2+	5.0	0.9	Pd2+	5.1	-1.0	O2-	5.0
CuAgO2	1.1	Cu+	4.8	0.8	Ag+	5.4	-0.9	O-	4.8
CuInO2	0.6	Cu+	3.8	1.9	In3+	6.0	-1.2	O2-	3.8
CuCsO2	1.1	Cu+	4.3	0.9	Cs+	6.8	-1.0	O-	4.3
CuBaO2	0.9	Cu2+	4.5	1.5	Ba2+	5.9	-1.1, -1.2, -1.3	O2-	4.6, 4.5
CuLaO2	0.6	Cu+	3.5	2.1	La3+	6.3	-1.3	O2-	3.5
CuPtO2	1.0	-	5.0	0.9	-	5.1	-1.0	-	5.0
CuAuO2	1.2	-	5.1	0.6	-	4.3	-0.9	-	4.3
CuHgO2	1.0	Cu2+	4.9	0.8	Hg2+	4.5	-0.9	O2-	4.5
CuTiO2	1.1	Cu3+	4.6	0.8	Tl+	6.4	-1.0	O2-	4.6
CuPbO2	1.0, 0.9	Cu2+	4.9	1.2	Pb2+	6.7	-1.1	O2-	4.9
CuBiO2	0.5	Cu+	3.7	2.9	Bi3+	6.0	-1.8, -1.6	O2-	3.8, 3.7
AuHO2	1.2	-	5.4, 5.2	0.7	-	3.0	-1.0, -0.9	-	3.0, 3.2
AuLiO2	1.1	-	5.1	0.9	-	5.1	-1.0	-	5.1
AuFO2	1.1	-	4.8	-0.6	-	5.4	-0.3	-	3.2
AuNaO2	1.1	-	5.1	0.9	-	6.1	-1.0	-	5.1
AuMgO2	0.4, 1.1	-	4.7, 5.2	1.7	-	5.7	-1.1, -1.4	-	5.2, 4.7
AuAlO2	0.4	-	4.7	3.0	-	6.0	-1.7	-	4.7
AuClO2	0.3	-	5.2	-0.3	-	5.2	-0.0	-	3.1
AuKO2	1.1	-	4.4	0.9	-	5.9	-1.0	-	4.4

Table A.1 (continued)

Structure	A			B			O		
	BC	OS	CN	BC	OS	CN	BC	OS	CN
AuScO2	0.4	-	4.2	2.0	-	6.0	-1.2	-	4.2
AuCrO2	0.5	-	4.4	1.8	-	6.0	-1.1	-	4.4
AuMnO2	0.5	-	4.3	1.6	-	5.6	-1.1	-	4.3
AuFeO2	0.6	-	4.4	1.4	-	6.0	-1.0	-	4.4
AuCoO2	0.5	-	4.6	1.4	-	6.0	-1.0	-	4.6
AuNiO2	0.5	-	4.3	1.2	-	6.0	-0.9	-	4.3
AuGaO2	0.4	-	4.5	1.9	-	6.0	-1.2	-	4.5
AuBrO2	0.2	-	5.6	-0.2	-	5.6	-0.0	-	3.1
AuRbO2	1.1	-	4.4	0.9	-	6.1	-1.0	-	4.4
AuSrO2	0.4, 1.0	-	4.4, 5.0	1.6	-	6.5	-1.0, -1.2	-	4.4, 5.0
AuYO2	0.4	-	3.9	2.2	-	6.1	-1.3	-	3.9
AuPdO2	0.5	-	4.1	1.0, 1.4	-	5.5, 5.9	-0.9	-	4.1, 4.5
AuAgO2	1.1	-	5.0	0.6	-	5.0	-0.9	-	5.0
AuCdO2	1.1, 0.4	-	4.5, 5.0	1.2	-	5.4	-1.0	-	4.5, 5.0
AuInO2	0.4	-	4.1	1.9	-	6.0	-1.2	-	4.1
AuCsO2	1.1	-	4.3	0.9	-	6.2	-1.0	-	4.3
AuBaO2	1.0, 0.3	-	4.8, 4.1	1.6	-	6.7	-1.0, -1.2	-	4.8, 4.1
AuLaO2	0.4	-	3.7	2.1	-	6.3	-1.2	-	3.7
AuTiO2	0.5	-	3.9	1.5	-	6.0	-1.0	-	3.9
AuPbO2	0.4, 1.1	-	4.0, 5.0	1.3	-	6.1	-1.0	-	4.0, 5.1
AuBiO2	0.4	-	4.0	2.9	-	6.0	-1.8, -1.5	-	4.0, 4.1

Table A.1 (continued)

Structure	A			B			O		
	BC	OS	CN	BC	OS	CN	BC	OS	CN
AgHO2	0.8	Ag2+	5.3	1.0	H+	3.1	-1.5, -0.3, -0.2	O2-, O-	3.1, 3.0
AgLiO2	1.1	Ag+	5.2	0.9	Li+	5.2	-1.0	O-	5.2
AgBO2	0.6	Ag+	4.6	3.0	B3+	3.3	-1.6, -2.0	O2-	3.3
AgNO2	0.7	Ag+	4.8	0.5	N3+	3.2	-0.6	O2-	3.2
AgFO2	1.1	-	5.4	-0.7	-	5.8	-0.2	-	3.2
AgNaO2	1.1	Ag+	5.1	0.9	Na+	6.1	-1.0	O-	5.1
AgAlO2	0.5	Ag+	4.7	3.0	Al3+	6.0	-1.8, -1.7	O2-	4.7
AgClO2	0.6	-	4.6	-0.5	-	4.6	-0.0	-	2.8
AgKO2	1.1	Ag+	4.4	0.8	K+	6.0	-1.0	O-	4.4
AgCaO2	0.7, 0.9	Ag+	5.3, 5.0	1.5	Ca2+	6.3	-1.1, -1.3	O-, O2-	5.5, 5.0
AgScO2	0.5	Ag+	4.2	2.0	Sc3+	6.0	-1.2	O2-	4.2
AgCrO2	0.5	Ag+	4.5	1.8	Cr3+	6.0	-1.2	O2-	4.5
AgMnO2	0.5	Ag+	4.4	1.6	Mn3+	5.6	-1.1	O2-	4.4
AgFeO2	0.5	Ag+	4.4	1.9	Fe3+	6.0	-1.2	O2-	4.4
AgCoO2	0.5	Ag+	4.7	1.4	Co3+	6.0	-1.0	O2-	4.7
AgNiO2	0.6	Ag+	4.4	1.3	Ni3+	6.0	-1.0	O2-	4.4
AgGaO2	0.5	Ag+	4.5	1.9	Ga3+	6.0	-1.2	O2-	4.5
AgAsO2	0.6	Ag+	4.9	3.1	As3+	4.1	-1.7, -2.0	O2-	4.1, 4.4
AgBrO2	0.5	-	4.5	-0.4	-	4.5	-0.0	-	2.8
AgRbO2	1.1	Ag+	4.4	0.9	Rb+	6.2	-1.0	O-	4.4
AgSrO2	0.6, 1.0	Ag+	4.6, 5.1	1.6	Sr2+	6.6	-1.1, -1.2	O-, O2-	4.6, 5.2

Table A.1 (continued)

Structure	A			B			O		
	BC	OS	CN	BC	OS	CN	BC	OS	CN
AgYO2	0.5	Ag+	4.0	2.2	Y3+	6.1	-1.4	O2-	4.0
AgRhO2	0.5	Ag+	4.4	1.3	Rh3+	6.0	-0.9	O2-	4.4
AgPdO2	0.7, 0.5	Ag+	5.5, 4.7	1.5, 0.9	Pd2+	6.0, 5.2	-0.9	O-, O2-	4.7, 5.2
AgCdO2	0.7, 1.0	Ag+	5.3, 5.0	1.2	Cd2+	6.3	-1.0, -1.1	O-, O2-	5.4, 5.0
AgInO2	0.5	Ag+	4.1	1.9	In3+	6.0	-1.2	O2-	4.1
AgCsO2	1.1	Ag+	4.3	0.9	Cs+	6.3	-1.0	O-	4.3
AgBaO2	0.8	Ag2+	5.1	1.5	Ba2+	9.0	-1.2	O2-	5.1
AgLaO2	0.5	Ag+	3.8	2.1	La3+	6.2	-1.3	O2-	3.8
AgPtO2	0.6, 0.5	-	4.8, 5.5	1.6, 0.9	-	6.0, 5.2	-0.9	-	4.8, 5.2
AgHgO2	0.9	Ag+	5.1	0.9	Hg2+	4.5	-0.9	O-, O2-	4.5
AgTiO2	0.5	Ag+	4.0	1.5	Ti3+	6.0	-1.0	O2-	4.0
AgPbO2	0.5	-	3.9	1.9, 1.4	-	6.0, 5.6	-1.1	-	3.9
AgBiO2	0.5	Ag+	4.0	2.9	Bi3+	5.8	-1.8, -1.6	O2-	4.0, 4.1
NiHO2	1.4	Ni3+	5.8	0.6	H+	3.1	-1.0	O2-	3.1, 3.4
NiLiO2	1.3	Ni3+	5.7	0.9	Li+	6.1	-1.1	O2-	5.7
NiFO2	1.4	Ni4+	5.3	-0.6	F-	5.3	-0.9, -0.8, 0.1	O2-, O-	3.1, 5.9
NiNaO2	1.3	Ni3+	5.6	0.8	Na+	7.4	-1.1	O2-	5.6
NiMgO2	1.2	Ni2+	6.0	1.7	Mg2+	6.0	-1.5	O2-	6.0
NiKO2	1.3	Ni3+	5.0	0.8	K+	8.9	-1.0, -1.1	O2-	5.5, 5.0
NiBrO2	1.3	Ni3+	6.0	0.6	Br+	4.1	-1.0	O2-	4.1
NiRbO2	1.2	Ni3+	4.2	0.8	Rb+	6.8	-1.0	O2-	4.2, 4.4

Table A.1 (continued)

Structure	A		B		O	
	BC	OS	BC	OS	BC	OS
NiCsO2	1.2	Ni3+	4.2	Cs+	-1.0	O2-
NiPtO2	1.3	-	6.0	-	-0.9	-
NiHgO2	1.3	Ni2+	6.0	Hg2+	-1.0	O2-

Table A.2 Bader charges (BC), oxidation state (OS) and coordination numbers (CN) for the CuXOS structures within 50 meV from the convex hull.

Structure	Cu		B		O		S	
	BC	OS	BC	OS	BC	OS	BC	OS
CuScOS	0.4	Cu+	1.9	Sc3+	5.3	5.3	5.3	5.6
CuYOS	0.4	Cu+	2.1	Y3+	6.5	6.5	6.5	7.2
CuInOS	0.4	Cu+	1.6	In3+	5.3	5.3	5.3	5.1
CuSbOS	0.4	Cu+	1.5	Sb3+	5.4, 5.2	5.4, 5.2	5.4, 5.2	4.4, 4.5
CuIOS	0.5	-	-0.2	-	4.9, 5.0	-	3.3	-0.6, 2.3
CuLaOS	0.4	Cu+	2.0	La3+	6.6	6.6	6.6	6.8
CuBiOS	0.4	Cu+	1.6	Bi3+	6.7	6.7	6.7	7.1

Ehrenwörtliche Erklärung

Ich erkläre hiermit ehrenwörtlich, dass ich die vorliegende Arbeit selbständig, ohne unzulässige Hilfe Dritter und ohne Benutzung anderer als der angegebenen Hilfsmittel und Literatur angefertigt habe. Die aus anderen Quellen direkt oder indirekt übernommenen Daten und Konzepte sind unter Angabe der Quelle gekennzeichnet. Bei der Auswahl und Auswertung folgenden Materials haben mir die nachstehend aufgeführten Personen in der jeweils beschriebenen Weise unentgeltlich geholfen:

1. Die Verbindung $\text{Ba}_8\text{Be}_{3.7}\text{Si}_{42.3}$ in Kapitel 4 wurde durch Dr. Stéphane Pailhès, Dr. Régis Debord und Dr. Romain Viennois experimentell synthetisiert und charakterisiert.
2. Ein Teil der Minima-Hopping-Rechnungen zu den AuXO_2 -Verbindungen in Kapitel 5 wurde vom Master-Studenten Sun Lin durchgeführt.
3. Prof. Dr. Miguel A. L. Marques hat die Prototyp-Rechnungen in Kapitel 5 durchgeführt.
4. Dr. Rafael Sarmiento-Pérez hat Kompressionsmodul und Schermodul für die Verbindungen in Kapitel 6 berechnet.
5. Prof. Dr. Fernando M. S. Nogueira hat den single-objective-genetic algorithm geschrieben, der in Kapitel 6 verwendet wurde.
6. Prof. Dr. Silvana Botti und Prof. Dr. Miguel A. L. Marques waren die betreuenden Hochschullehrer dieser Arbeit.

Weitere Personen waren an der inhaltlich-materiellen Erstellung der vorliegenden Arbeit nicht beteiligt. Insbesondere habe ich hierfür nicht die entgeltliche Hilfe von Vermittlungs- bzw. Beratungsdiensten (Promotionsberater oder andere Personen) in Anspruch genommen. Niemand hat von mir unmittelbar oder mittelbar geldwerte Leistungen für Arbeiten erhalten, die im Zusammenhang mit dem Inhalt der vorgelegten Dissertation stehen. Die Arbeit wurde bisher weder im In- noch im Ausland in gleicher oder ähnlicher Form einer anderen Prüfungsbehörde vorgelegt. Die geltende Promotionsordnung der Physikalisch-Astronomischen Fakultät ist mir bekannt. Ich versichere ehrenwörtlich, dass ich nach bestem Wissen die reine Wahrheit gesagt und nichts verschwiegen habe.

Tiago F.T. Cerqueira
July 8, 2016